Cavity quantum electrodynamics with ultracold atoms and superconducting resonators

Dissertation

zur Erlangung des akademischen Grades
Doktorin der Naturwissenschaften

eingereicht an der
Fakultät für Mathematik, Informatik und Physik
der Universität Innsbruck

von

Dipl.-Phys. Kathrin Sandner

Betreuer der Dissertation: Univ.-Prof. Dr. Helmut Ritsch,
Institut für Theoretische Physik

Innsbruck, September 2012

Zusammenfassung

Die vorliegende Arbeit befasst sich mit hybriden Implementationen in der Cavity Quantenelektrodynamik (Cavity QED). Darunter versteht man Systeme, die Grundbausteine aus der Circuit Quantenelektrodynamik (Circuit QED) mit kalten Atomen oder mit Spins in Festkörpern kombinieren. Die Bausteine der Circuit QED sind kleine Inseln und Drähte aus supraleitendem Material, die sich zu Resonatoren und künstlichen Atomen zusammensetzen lassen. Ein wichtiges Ziel ist die Schaffung einer Verbindung zwischen den unterschiedlichen Implementationen in der Cavity Quantenelektrodynamik, um so deren jeweilige Stärken nutzen zu können. Systeme, die auf echten Atomen basieren haben den Vorteil, dass ein Photon über eine relativ lange Zeit in einem Atom oder einem Ensemble von Atomen gespeichert werden kann. Künstliche Quantensysteme können sich ähnlich verhalten wie echte Atome, haben aber den Vorteil, dass sie auf kleinstem Raum integriert werden können und auf viel kürzeren Zeitskalen manipulierbar sind. Um die Stärken der verschiedenen Implementationen nutzen zu können, muss eine Verbindung hergestellt werden, was durch starke Kopplung an einen gemeinsamen Resonator erreicht werden kann. Im Bereich der künstlichen Quantensysteme werden häufig supraleitende Koplanare-Wellenleiter-Resonatoren (CPW Resonatoren) eingesetzt. Ein vorrangiges Ziel dieser Arbeit ist es daher, aufzuzeigen, unter welchen Umständen starke Kopplung zwischen Ensembles von Atomen oder, alternativ, zwischen Stickstoff-Fehlstellen-Zentren in Diamant, und einem CPW Resonator erreicht werden kann. Darüber hinaus ergeben sich interessante Perspektiven, um auf dieser Basis neuartige Lasersysteme zu entwerfen und zu untersuchen.

Dieser Teil der Arbeit entstand in enger Kooperation zwischen Theorie und Experiment, was viele Ideen und Ansätze hervorgebracht hat und darüber hinaus den direkten Vergleich mancher theoretischer Ergebnisse mit den Experimenten ermöglichte. Die Experimente wurden in der Gruppe von Jörg Schmiedmayer, insbesondere von Johannes Majer und Robert Amsüss, geplant und durchgeführt.

In einem weiteren Teilprojekt, das ebenfalls im Bereich der Cavity QED angesiedelt ist, wird das Verhalten von Quanten Kaskadenlasern (QC Lasern) und deren Temperaturbeständigkeit untersucht. Während in üblichen Halbleiterlasern Photonen durch Übergänge zwischen dem Valenzband und dem Leitungsband erzeugt werden, basieren Kaskadenlaser auf Übergängen innerhalb eines Bandes. Ein Kaskadenlaser besteht aus sich wiederholenden Abfolgen von verschiedenen Halbleiterschichten, die eine Serie von Potentialtöpfen bilden. Wird eine Spannung angelegt, so passieren Elektronen die Struktur und es kommt wiederholt zur Emission von Photonen. Üblicherweise wird die Leistung eines Kaskadenlasers durch Heizeffekte begrenzt.

Zwischen den einzelnen Emissionsschritten werden Phononen erzeugt und der Laser erhitzt sich so lange, bis die Lasertätigkeit zum erliegen kommt. Ein Teil dieser Arbeit beschäftigt sich mit Möglichkeiten, diesem unerwünschten Prozess entgegenzuwirken. Darüber hinaus wird ein alternativer Pumpmechanismus untersucht, der auf einem Temperaturgradienten innerhalb der Halbleiterstruktur basiert anstatt auf dem Anlegen einer Spannung.

Abstract

This thesis is concerned with hybrid systems in cavity quantum electrodynamics (cavity QED). These are systems that combine elements from circuit quantum electrodynamics (circuit QED) with atoms or spin ensembles. A central goal of this work is to establish a link between the different implementations in cavity QED in order to pool their individual strength. Systems based on real atoms have the advantage that an excitation can be stored over a relatively long time in an atom or an ensemble of atoms. Artificial quantum systems, or circuit QED systems, can behave like real atoms, but can be densely integrated on a chip and manipulated on a shorter timescale. To combine the strength of both systems it is necessary to connect them, a task that can be fulfilled by the strong coupling to a common resonator. In circuit QED, superconducting coplanar waveguide (CPW) resonators are widely-used. Thus, an important aim of this thesis is to demonstrate under which circumstances it is possible to reach the strong coupling regime for ensembles of atoms, or nitrogen vacancy centers and CPW resonators. Moreover, interesting prospects for new laser systems in this context are investigated.

This part of the present thesis was performed in close collaboration between physicists working in experimental and theoretical cavity QED. This collaboration motivated many research objectives and allowed for the comparison of some theoretical findings with actual measurements. The experiments were realized in the group of Jörg Schmiedmayer, in particular by Johannes Majer and Robert Amsüss, at the Atomic Institute in Vienna.

In a second project, also relating to cavity QED, the behavior of quantum cascade (QC) lasers and their temperature stability are studied. While in conventional semiconductor lasers photons are created by transitions between the valence band and the conduction band, QC lasers are based on intraband transitions. A QC laser is built from repeated patterns of semiconductor materials which establish a series of potential wells. An external electric potential causes electrons to travel through the structure and leads to repetitive photon emission. The output power of a QC laser is usually limited by heating processes. Between the photon emission steps, phonons are produced and the laser gradually heats up until the lasing activity ceases. Here we study possible ways to reduce this detrimental heating processes. Moreover, an alternative mechanism for providing gain based on a sustained spatial temperature gradient instead of an external potential is investigated.

Contents

1. General Introduction and Motivation 1
- 1.1. So it has come to this: A brief history of cavity QED 1
- 1.2. Motivation and Outline 4

I. Strong coupling of spin ensembles and superconducting resonators 9

2. Introduction to cavity QED with ensembles 11
- 2.1. The Jaynes-Cummings Hamiltonian 11
- 2.2. The Tavis-Cummings Hamiltonian 14
  - 2.2.1. Dicke states 14
  - 2.2.2. Weak excitation limit 15
  - 2.2.3. Superradiance 18
- 2.3. Open quantum systems 19
  - 2.3.1. Master equations 19
  - 2.3.2. Operator expectation values 21
- 2.4. Strong coupling regime 23
- 2.5. Cavity emission spectrum 25
- 2.6. Experimental Implementations 29
  - 2.6.1. Coplanar waveguide resonators 29
  - 2.6.2. Rubidium Ensemble 30
  - 2.6.3. Nitrogen-Vacancy Centers 31

3. Publication: Cavity QED with an ultracold ensemble on a chip 37
- 3.1. Introduction 37
- 3.2. Model 39
- 3.3. Collective atom-field Hamiltonian 39
- 3.4. Master equation including decoherence and thermal noise 42
- 3.5. Signatures of strong coupling 43
- 3.6. Numerical solution for small particle number 44
- 3.7. Truncated cumulant expansion of collective observables 46
- 3.8. Cavity output spectrum at finite temperature 49

3.9. Cooling the field mode with the atomic ensemble 50
3.10. Coherently driven cavity mode 54
3.11. Spectrum of the coherently driven cavity 56
3.12. Superradiance 59
3.13. Narrowbandwidth hyperfine micromaser 61
3.14. Conclusions 63
3.15. Acknowledgment 65
3.16. Appendix A: Coupled Equations 65
3.17. Appendix B: Validity of the cumulant expansion 68

4. Publication: Cavity QED with magnetically coupled collective spin states 73

5. Publication: Strong magnetic coupling of an inhomogeneous NV ensemble to a cavity 85
5.1. Introduction 86
5.2. General system properties and experimental implementation 87
5.3. Theoretical model 88
5.4. Experimental setup and parameters 89
5.5. Cavity transmission spectra for inhomogeneous ensembles 90
5.6. Coupled collective oscillator approximation 90
5.7. Polarization decay and collective coupling at finite temperature . . . 93
5.8. Detailed modeling and reconstruction of inhomogeneous distributions 97
5.9. A transmission line micro-maser with an inhomogeneous NV ensemble 106
5.10. Conclusions 108
5.11. Acknowledgment 108

II. Quantum cascade lasers 111

6. Introduction to quantum cascade lasers 113
6.1. Devices 113
6.2. Theoretical description of a single QC laser 115
6.3. Coupled QC lasers 119
6.4. Suppression of heating and alternative pumping schemes 126

7. Preprint: Temperature gradient driven lasing and stimulated cooling 129

8. List of Publications 143

1. General Introduction and Motivation

The theory of classical *electrodynamics* describes the interaction between charged particles and the electromagnetic field. The idea that light is comprised of discrete lumps of energy brings about the *quantization* of the electromagnetic field. Finally, mirrors that form a *cavity* in which photons are repeatedly reflected single out resonant field modes. In short: Cavity QED deals with the interaction between matter and the quantized field modes in a resonator.

Starting with the first steps towards quantum electrodynamics, a short history of the field of cavity QED is given in Sec. 1.1 to point out key developments and to motivate the research activities presented in this thesis.

1.1. So it has come to this: A brief history of cavity QED

The quantization of the electromagnetic field was motivated by the difficulties discovered in the description of the nature of black-body radiation. In 1900 Max Plank rather reluctantly presented the idea that the modes of the electromagnetic field exchange energy with heated bodies only in multiples of $\hbar\omega$, thus solving the so-called "ultraviolet puzzle". This lumps of radiation with energy $\hbar\omega$ later were termed "Lichtquanten" by Albert Einstein in his work about the photoelectric effect [1.1]. The actual term "photon" was suggested by Lewis in 1926 [1.2]. It was not until the work of Schwinger, Feynman, Tomonaga and Dyson, who solved the self-energy problem in the early formulation of quantum electrodynamics in the late 1940s, that the theory became as successful as it is in describing the interaction of light and matter. However, the key aspect of this research rather laid on matter than on light. New paths were explored with the invention of new sources of light.

The field of quantum optics owes its present relevance to the invention of the laser. Early studies in quantum optics were mostly concerned with the statistical properties of laser light, thus introducing a theoretical description of the quantum states of light [1.3]. The development of tunable lasers not only allowed for precision measurements in spectroscopy, they are also an indispensable tool for the trapping and cooling of atoms, techniques that are major building blocks of quantum optics as we know it today [1.4–1.7].

A fundamental part of the theoretical description of light-matter interactions concerns the treatment of dissipation in a consistent quantum mechanical way, as a majority of the problems studied in quantum optics are open system, i.e. interacting with some sort of environment. It is again the invention of the laser that triggered the development of the description of dissipation in quantum mechanics. Since an essential part of a laser is a lossy cavity, lasers are per se open systems. Naive approaches to include damping fail when it comes to the requirement that, to be consistent with quantum mechanics, the commutation relations must be preserved. The solution lies in the close relationship between dissipation and fluctuations: The interaction with the environment results not only in damping, but also in a fluctuating force. Taking into account the fluctuating force preserves the commutation relations, which becomes apparent in the Heisenberg picture [1.8, 1.9]. The equivalent formulation in the Schrödinger picture is given by the master equation approach. It also relies on the partition of the whole dynamics into those for the small system we are interested in, those for a heat bath surrounding it, and an interaction between system and bath [1.10, 1.11]. The requirements and results brought about by the master equation approach are discussed in Sec. 2.3.

The field of cavity quantum electrodynamics was initiated by Edward Mills Purcell who noted in 1946 that the spontaneous emission rate of a spin in a magnetic resonance setup should be enhanced in a resonant structure [1.12]. The main idea was to enhance the spontaneous emission rate by coupling it to a damped oscillator (an R-L-C circuit), serving as an additional loss channel. The same argument holds for the spontaneous emission rate of an atom in a cavity. Until Purcell's note, the spontaneous emission rate of an excited atom, arising from the coupling to near-resonant field modes and the shift of atomic energy levels caused by the dissipative coupling to off-resonant field modes, had been assumed to be immutable. The role of the cavity is to support near resonant modes that have a high amplitude inside the cavity and thus to increase the interaction of the spin with near-resonant modes (i.e. the spontaneous emission rate) [1.13]. Cavity-enhanced emission has been realized experimentally in the microwave [1.14] and the optical regime [1.15]. The cavity can also be designed such that resonant field modes are suppressed, resulting in the effect of spontaneous emission inhibition [1.16]. The parameter regime in which cavity-enhanced or inhibited emission can be found is usually called *perturbative regime*. The term expresses the assumption that the coupling between the atom and the mode is weak compared to the cavity decay rate and that a perturbative treatment is possible.

The Purcell effect can also be explained by the constructive interference between the field emitted by the atom and the field reflected by a mirror. This situation is comparable with an atom interacting with an ensemble of atoms surrounding it, leading to superradiant emission [1.17]. Both subjects, superradiance theory and cavity QED in the perturbative limit have been developed around the same time.

The first experiments in the field of cavity QED were performed in the perturbative regime, altering incoherent quantum dynamics. It took quite some time to enter the so-called *strong coupling regime* where the system was expected to behave in a completely different way. The strong coupling regime is defined by the requirement that the coupling rate between the atom and the field exceeds the loss rates of both, cavity and atom. Loosely speaking, a photon will be reabsorbed by the atom before it gets the chance to be lost via a mirror. To reach this regime in an experiment, it is necessary to build cavities with a low photon loss rate and a very small mode volume, as the mode volume is inversely proportional to the cavity-atom coupling rate. The first successful experiments were performed in the collective strong coupling regime, both for microwave [1.18] and optical cavities [1.19]. The collective coupling rate of N atoms scales with $\sqrt{N}$, making it possible to observe strong coupling by increasing the number of atoms. In microwave cavity QED, experiments with better cavities followed, where a stream of excited atoms was sent through the cavity, interacting with it for the time it takes to pass through the mode volume [1.20]. Even better control over the timing and velocity was achieved in a series of experiments where Rydberg atoms were sent through the cavity [1.21–1.23]. In optical cavity QED the strong coupling regime with single atoms was first observed in 1992 [1.24].

Today, cavity QED is studied in a wide variety of contexts ranging from cavity assisted cooling of atoms [1.25, 1.26], over the signature of states of ultracold gases in cavity transmission spectra [1.27], to the storage of quantum information using the cavity as a link between several components of the system [1.28, 1.29].

A very recent direction of research is towards so-called *hybrid systems* that combine solid state devices from *circuit quantum electrodynamics* with trapped atoms or spins in a solid. The physics of circuit quantum electrodynamics shares many concepts with cavity QED, although the implementation is fundamentally different. The components of circuit QED are μm sized structures of superconducting material forming resonators or small islands (Cooper-pair boxes) and are entirely man-made. Over the recent years the development in circuit QED retraced the scientific milestones of cavity QED with cold atoms, albeit at an accelerated pace [1.30–1.32].

1.2. Motivation and Outline

The first part of the present work is motivated by the effort to identify promising building blocks for hybrid systems, in particular ensembles of ultracold atoms or spins in a solid strongly coupled to a resonator. Important questions in this context are the influence of thermal excitations, as the resonators are in the GHz regime, and the role of the frequency inhomogeneity in solid state systems. The second part of the thesis is motivated by promising developments in the field of semiconductor heterostructures, which can be etched down to form different types of microdisc cavities. Such a structure can be operated as a laser in the THz regime and has been implemented in various forms for different wavelengths [1.33–1.35]. However, the regime of operation of such devices is usually limited by intrinsic heating. It is therefore a desirable goal to reduce the intrinsic heating and thereby extending the range of operation.

The work on the strong coupling between spin ensembles and cavities is presented in Part I. The main aspects of the theoretical approach are outlined in Sec. 2. Sections 3, 4 and 5 contain publications concerned with particular implementations of cavity QED systems either planned or already realized at the Atomic Institute in Vienna. In Part II the results of another cavity QED project with focus on quantum cascade lasers (QC lasers) are presented. In Sec. 6 we give a brief introduction into this type of laser and the theoretical description. In Sec. 6.3 we study two QC lasers that are coupled via their evanescent fields. Finally, in Sec. 6.4 we motivate an alternative pumping mechanism for structures similar to those of QC lasers based on a spatial temperature gradient and investigate prospects for extending the operating regime of QC lasers by counteracting intrinsic heating. The results on the temperature gradient pumping and the prevention of heating are summarized as a preprint in Sec. 7.

References for Chapter 1

[1.1] A. Einstein. "On a heuristic viewpoint concerning the production and transformation of light." In: *Annalen der Physik* 17 (1905), pp. 132–148.

[1.2] G.N. Lewis. "The conservation of photons." In: *Nature* 118 (1926), pp. 874–875.

[1.3] R.J. Glauber. "Coherent and incoherent states of the radiation field." In: *Physical Review* 131.6 (1963), pp. 2766–2788.

[1.4] T.W. Hänsch and A.L. Schawlow. "Cooling of gases by laser radiation." In: *Optics Communications* 13.1 (1975), pp. 68–69.

[1.5] D.J. Wineland, R.E. Drullinger, and F.L. Walls. "Radiation-pressure cooling of bound resonant absorbers." In: *Physical Review Letters* 40.25 (1978), pp. 1639–1642.

[1.6] W. Neuhauser et al. "Optical-sideband cooling of visible atom cloud confined in parabolic well." In: *Physical Review Letters* 41.4 (1978), pp. 233–236.

[1.7] S. Chu, C. Cohen-Tannoudji, and W.D. Phillips. "Nobel lectures in physics 1997." In: *Rev. Mod. Phys* 70.3 (1998), pp. 685–741.

[1.8] I.R. Senitzky. "Dissipation in quantum mechanics. The harmonic oscillator." In: *Physical Review* 119.2 (1960), p. 670.

[1.9] H.J. Carmichael. *Statistical methods in quantum optics 1: Master Equations and Fokker-Planck Equations.* Springer, 1999.

[1.10] W.H. Louisell. *Quantum statistical properties of radiation.* Vol. 2. Wiley, 1973, 1973.

[1.11] H. Haken. "Handbuch der Physik." In: *Vol. XXV, 2c, Springer, Berlin* (1970).

[1.12] E.M. Purcell. "Spontaneous emission probabilities at radio frequencies." In: *Physical Review* 69 (1946), p. 681.

[1.13] H.J. Carmichael. *Statistical Methods in Quantum Optics: Non-classical fields.* Vol. 2. Springer Verlag, 2007.

[1.14] P. Goy et al. "Observation of cavity-enhanced single-atom spontaneous emission." In: *Physical review letters* 50.24 (1983), p. 1903.

[1.15] D.J. Heinzen et al. "Enhanced and inhibited visible spontaneous emission by atoms in a confocal resonator." In: *Physical review letters* 58.13 (1987), pp. 1320–1323.

[1.16] D. Kleppner. "Inhibited spontaneous emission." In: *Physical Review Letters* 47.4 (1981), pp. 233–236.

[1.17] R.H. Dicke. “Coherence in spontaneous radiation processes.” In: *Physical Review* 93.1 (1954), pp. 99–110.

[1.18] Y. Kaluzny et al. “Observation of self-induced Rabi oscillations in two-level atoms excited inside a resonant cavity: the ringing regime of superradiance.” In: *Physical review letters* 51.13 (1983), p. 1175.

[1.19] R.J. Brecha et al. “Observation of oscillatory energy exchange in a coupled-atom—cavity system.” In: *JOSA B* 12.12 (1995), pp. 2329–2339.

[1.20] D. Meschede, H. Walther, and G. Müller. “One-atom maser.” In: *Physical review letters* 54.6 (1985), pp. 551–554.

[1.21] S. Haroche, G. Grynberg, and R. Stora. “New Trends in Atomic Physics.” In: *Proceedings of the Les Houches Summer School of Theoretical Physics* (1984), p. 193.

[1.22] H. Walther. “The single atom maser and the quantum electrodynamics in a cavity.” In: *Physica Scripta* 1988.T23 (2007), p. 165.

[1.23] J.M. Raimond, M. Brune, and S. Haroche. “Manipulating quantum entanglement with atoms and photons in a cavity.” In: *Reviews of Modern Physics* 73.3 (2001), p. 565.

[1.24] R.J. Thompson, G. Rempe, and H.J. Kimble. “Observation of normal-mode splitting for an atom in an optical cavity.” In: *Physical Review Letters* 68.8 (1992), pp. 1132–1135.

[1.25] P. Domokos and H. Ritsch. “Collective cooling and self-organization of atoms in a cavity.” In: *Physical review letters* 89.25 (2002), p. 253003.

[1.26] T. Salzburger and H. Ritsch. “Atomic self-trapping induced by single-atom lasing.” In: *Physical review letters* 93.6 (2004), p. 63002.

[1.27] I.B. Mekhov, C. Maschler, and H. Ritsch. “Probing quantum phases of ultracold atoms in optical lattices by transmission spectra in cavity quantum electrodynamics.” In: *Nature physics* 3.5 (2007), pp. 319–323.

[1.28] M. Wallquist et al. “Hybrid quantum devices and quantum engineering.” In: *Physica Scripta* 2009 (2009), p. 014001.

[1.29] P. Rabl et al. “Hybrid quantum processors: molecular ensembles as quantum memory for solid state circuits.” In: *Physical review letters* 97.3 (2006), p. 33003.

[1.30] D. Vion et al. “Manipulating the quantum state of an electrical circuit.” In: *Science* 296.5569 (2002), pp. 886–889.

[1.31] F. Mallet et al. “Single-shot qubit readout in circuit quantum electrodynamics.” In: *Nature Physics* 5.11 (2009), pp. 791–795.

[1.32] A. Wallraff et al. “Strong coupling of a single photon to a superconducting qubit using circuit quantum electrodynamics.” In: *Nature* 431.7005 (2004), pp. 162–167.

[1.33] J. Faist et al. “Quantum cascade laser.” In: *Science* 264.5158 (1994), pp. 553–556.

[1.34] C. Gmachl et al. “Long-wavelength (9.5-11.5 μm) microdisk quantum-cascade lasers.” In: *Quantum Electronics, IEEE Journal of* 33.9 (1997), pp. 1567–1573.

[1.35] C. Gmachl et al. “Recent progress in quantum cascade lasers and applications.” In: *Reports on progress in physics* 64 (2001), p. 1533.

Part I.

Strong coupling of spin ensembles and superconducting resonators

2. Introduction to cavity QED with ensembles

The aim of this section is to clarify the notation and to point out the basic similarities and differences when dealing with single spins and whole ensembles of spins coupled to a cavity. Note that the term spin is used synonymously with the term two-level system or two-level atom, as well as the term light refers to radiation in the visible and in the microwave regime. We then introduce the master equation approach for open quantum systems and discuss the hallmarks of the strong coupling regime before we briefly introduce some implementations of hybrid systems.

In the forthcoming discussion we always assume single mode cavities. A cavity mode can be conveniently modelled by a one-dimensional oscillator with frequency ω_c and annihilation and creation operators a and $a^\dagger$. An atom resonantly interacting with the mode can be truncated to a two-level system with upper state $|e\rangle$ and lower state $|g\rangle$, connected by an electric (or magnetic) dipole transition at the frequency ω_a. The raising and lowering operators for the two-level system are $\sigma^+ = |e\rangle\langle g|$ and $\sigma^- = |g\rangle\langle e|$ with $[\sigma^+, \sigma^-] = \sigma^z$. Other atomic transitions are assumed to be off-resonant.

2.1. The Jaynes-Cummings Hamiltonian

A single standing-wave cavity mode interacting with a two-level system localized at an antinode of the field is described by the Jaynes-Cummings Hamiltonian

$$\begin{aligned} \mathrm{H_{JC}} &= \mathrm{H_A} + \mathrm{H_F} + \mathrm{H_I} \\ &= \frac{1}{2}\hbar\omega_a\sigma^z + \hbar\omega_c a^\dagger a + \mathrm{i}\hbar g\left(a^\dagger\sigma^- - a\sigma^+\right) \; . \end{aligned} \tag{2.1.1}$$

The dipole coupling constant $g = \sqrt{\frac{\omega_c d^2}{2\hbar\varepsilon_0 V}}$ quantifies the coupling strength per photon between the two-level system and the mode, where d denotes the dipole matrix element of the atomic transition, and V refers to the mode volume [2.1]. To begin with we introduce the eigenstates of the bare Hamiltonian $\mathrm{H_A} + \mathrm{H_F}$. Without $\mathrm{H_I}$ the states $|e, n-1\rangle$ (two-level system in its excited state, $n-1$ photons in the cavity) and $|g, n\rangle$ (two-level system in its ground state, n photons in the cavity) are degenerate. The degeneracy is lifted by the interaction, or in other words, the diagonalization of the full Hamiltonian yields new eigenstates, often called *dressed states* for each pair of excited states with n excitations ($n = 1, 2, \cdots$)

$$|+, n\rangle = \frac{1}{\sqrt{2}} \left(\mathcal{C}\,|e, n-1\rangle + \mathrm{i}\mathcal{D}\,|g, n\rangle\right) \tag{2.1.2}$$

$$|-, n\rangle = \frac{1}{\sqrt{2}} \left(\mathcal{D}\,|e, n-1\rangle - \mathrm{i}\mathcal{C}\,|g, n\rangle\right)\ , \tag{2.1.3}$$

where

$$\mathcal{C} = \left[1 + \frac{\frac{1}{2}\left(\omega_a - \omega_c\right)}{\sqrt{\frac{1}{4}\left(\omega_a - \omega_c\right)^2 + g^2 n}}\right]^{\frac{1}{2}}\ , \tag{2.1.4}$$

and

$$\mathcal{D} = \left[1 - \frac{\frac{1}{2}\left(\omega_a - \omega_c\right)}{\sqrt{\frac{1}{4}\left(\omega_a - \omega_c\right)^2 + g^2 n}}\right]^{\frac{1}{2}}\ . \tag{2.1.5}$$

The energies of each pair of states are given by

$$E_{+,n} = (n - \frac{1}{2})\hbar\omega_a + \hbar\sqrt{\frac{1}{4}\left(\omega_a - \omega_c\right)^2 + g^2 n} \tag{2.1.6}$$

$$E_{-,n} = (n - \frac{1}{2})\hbar\omega_a - \hbar\sqrt{\frac{1}{4}\left(\omega_a - \omega_c\right)^2 + g^2 n}\ . \tag{2.1.7}$$

The energy of the ground state is

$$E_G = -\frac{1}{2}\hbar\omega_a\ . \tag{2.1.8}$$

At resonance ($\omega_c = \omega_a$) we obtain simplified expressions for the eigenstates

$$|+, n\rangle = \frac{1}{\sqrt{2}} \left(|e, n-1\rangle + \mathrm{i}\,|g, n\rangle\right) \tag{2.1.9}$$

$$|-, n\rangle = \frac{1}{\sqrt{2}} \left(|e, n-1\rangle - \mathrm{i}\,|g, n\rangle\right)\ , \tag{2.1.10}$$

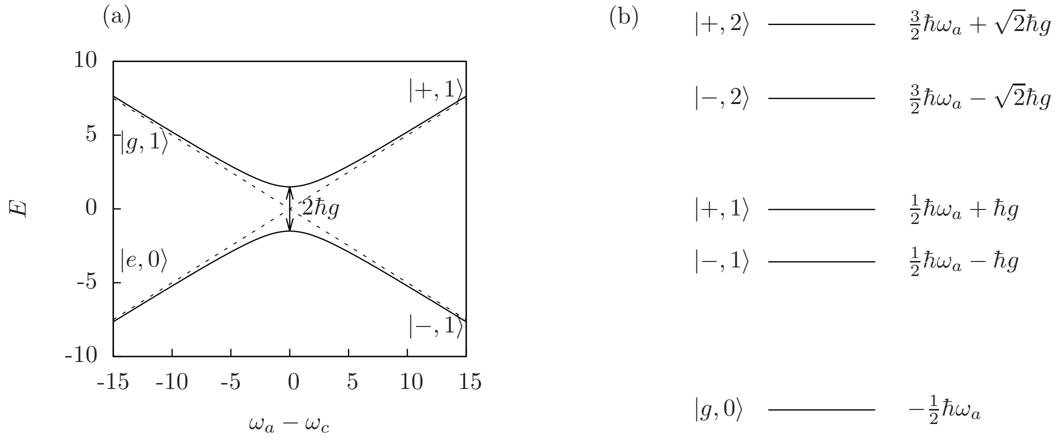

Figure 2.1.: (a) Energies of the dressed states $|+,1\rangle$ and $|-,1\rangle$ as a function of the detuning $\omega_a - \omega_c$. For large detunings the dressed states asymptotically approach the unperturbed states. At $\omega_a - \omega_c = 0$ the splitting between the states is $2\hbar g$. (b) Sketch of the Jaynes-Cummings ladder with the first and second pair of excited states. The separation between the excited-state doublets increases with $\sqrt{n}$.

and also for the eigenenergies

$$E_{+,n} = (n - \frac{1}{2})\hbar\omega_a + \sqrt{n}\hbar g \tag{2.1.11}$$

$$E_{-,n} = (n - \frac{1}{2})\hbar\omega_a - \sqrt{n}\hbar g \; . \tag{2.1.12}$$

The energies of the eigenstate pairs in the resonant case form the so-called Jaynes-Cummings ladder in which the splitting between each pair of states grows anharmonicly with $\sqrt{n}$, see Fig. 2.1. The splitting between the $|+,1\rangle$ and $|-,1\rangle$ states is given by $2\hbar g$ and is usually referred to as vacuum Rabi splitting. For an atom in the state $|e\rangle$ that enters the empty cavity, the state $|e,0\rangle$ is no longer an eigenstate but can be written as a superposition of the eigenstates $|+,1\rangle$ and $|-,1\rangle$. The spectrum of the emitted radiation therefore yields two peaks [2.1]. The excited atom will emit a photon into the cavity and reabsorb it a short time later, hence the probability to find the atom in the excited state will undergo Rabi oscillations.

The eigenenergy pairs are split by $2\hbar g\sqrt{n}$. For sufficiently large g this anharmonicity can lead to the situation where the $|-,1\rangle \rightarrow |-,2\rangle$ transition is off-resonant when the driving frequency is tuned to the $|g,0\rangle \rightarrow |-,1\rangle$ transition. The states $|g,0\rangle$ and $|-,1\rangle$ then form an effective two level system [2.2]. Another consequence of the anharmonicity is the collapse and revival of Rabi oscillations when an atom interacts with a coherent state in a cavity [2.3, 2.4].

The study of the Jaynes-Cummings Hamiltonian alone gives some insight into the dynamics of the system. The actual behavior of an atom interacting with a cavity mode will strongly depend on the quality of the mirrors, shielding the mode from its surrounding, and the spontaneous emission rate of the atom. The description of open quantum systems, motivated by this (almost always) inevitable coupling to the environment, will be discussed in Sec. 2.3.

2.2. The Tavis-Cummings Hamiltonian

We now turn to the description of an ensemble of identical two-level atoms coupled to a single cavity mode. The Hamiltonian

$$\mathrm{H_{TC}} = \hbar\omega_c a^\dagger a + \frac{\hbar\omega_a}{2}\sum_j^N \sigma_j^z + \hbar g \sum_j^N \left(\sigma_j^+ a + a^\dagger \sigma_j^-\right) \ . \tag{2.2.1}$$

thus contains a sum over all atoms (with index j) that couple to the mode. Here we assumed that all atoms have the same frequency ω_a and that they are coupled with the same strength g. The energy eigenstates of the Tavis-Cummings Hamiltonian are highly degenerate, reflecting the many possibilities to deposit an excitation in the ensemble. A simplified treatment is possible if all atoms are confined in a small volume and couple to the field with equal strength. The only state of the ensemble containing one excitation which takes part in the dynamics is then a symmetric superposition of all possible states with one excited atom. It also is the first state in a whole ladder of so-called Dicke states with growing number of excitations.

2.2.1. Dicke states

It is instructive to introduce the collective spin operators

$$\mathrm{S^z} = \frac{1}{2}\sum_j^N \sigma_j^z \quad \text{and} \quad \mathrm{S^\pm} = \sum_j^N \sigma_j^\pm \tag{2.2.2}$$

together with the total spin operator $\boldsymbol{S} = (\mathrm{S^x}, \mathrm{S^y}, \mathrm{S^z})$, where $\mathrm{S^\pm} = (\mathrm{S^x} \pm \mathrm{i}\,\mathrm{S^y})$. The eigenstates of $\boldsymbol{S}$ and $\mathrm{S^z}$ are the Dicke states $|J, M\rangle$ with $\boldsymbol{S}\,|J, M\rangle = J\,(J+1)\,|J, M\rangle$

and $\mathrm{S}^{\mathrm{z}}\left|J, M\right\rangle = M\left|J, M\right\rangle$ where $J = 0, 1, \cdots, N/2$ and $M = -J, -J+1, \cdots, J$ [2.5]. The state with all atoms in the excited state $\left|e, e, \cdots, e\right\rangle$ is identified with the state $\left|J, J\right\rangle$, while $\left|J, -J\right\rangle$ corresponds to the state $\left|g, g, \cdots, g\right\rangle$. Both states have maximum angular momentum $J = N/2$. The total number of excitations is given by $J + M$. The collective raising and lowering operators generate the intermediate states according to

$$\mathrm{S}^{\pm}\left|J, M\right\rangle = \sqrt{\left(J \pm M + 1\right)\left(J \mp M\right)}\left|J, M \pm 1\right\rangle \ . \tag{2.2.3}$$

These states are a sufficient basis in the case that the atoms are confined in a volume small compared to the wavelength of an emitted photon and equally coupled to it. This implies that a photon that is absorbed in this cloud of atoms cannot be assigned to a single atom. For example, the state $\left|J, -J+1\right\rangle$ is a symmetric superposition of all states containing one excitation, i.e

$$\frac{1}{\sqrt{N}}\left(\left|e, g, \cdots, g\right\rangle + \left|g, e, \cdots, g\right\rangle + \cdots + \left|g, g, \cdots, e\right\rangle\right) \ . \tag{2.2.4}$$

There are several important properties that emerge from this collective description: The Dicke states $\left|J, M\right\rangle$ with $J = N/2$ form a ladder of states with equidistant energies. For a single excitation, the coupling between the mode and the ensemble scales with $\sqrt{N}$, as can be seen by applying the collective raising operator in Eq. (2.2.3) to the state $\left|N/2, -N/2\right\rangle$. As long as the number of excitations is small compared to N, the ensemble behaves like a harmonic oscillator. To see this we write

$$\begin{aligned}\left|\left\langle J, M+1\left|\mathrm{S}^{+}\right|J, M\right\rangle\right|^2 &= \left(J + M + 1\right)\left(J - M\right) \\ &= \left(J + M + 1\right)\left(N - \left(J + M\right)\right) \qquad (2.2.5) \\ &\approx \left(J + M + 1\right)N \quad \text{for} \quad J + M \ll N \qquad (2.2.6)\end{aligned}$$

and compare it to $\left|\left\langle n+1\left|a^{\dagger}\right|n\right\rangle\right|^2 = (n+1)$. Both matrix elements scale linearly with the number of excitations [2.6].

2.2.2. Weak excitation limit

In the weak excitation limit the ensemble and the cavity mode can be regarded as a pair of harmonic oscillators coupled at a rate of $g\sqrt{N}$. This is sketched in Fig. 2.2(a). At the level of a single excitation the Jaynes-Cummings and the Tavis-Cummings Hamiltonian are equivalent, except that the resonant splitting between the first excited state pair is $2\hbar g\sqrt{N}$ for the many atom case. An important difference shows

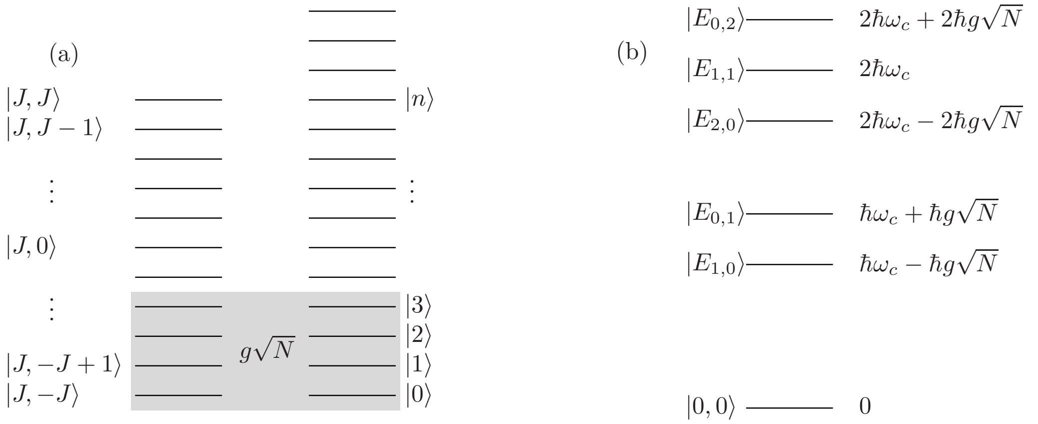

Figure 2.2.: (a) Sketch of the harmonic energy ladders of the Dicke states and the cavity mode. The gray shaded area indicates the regime in which the ensemble is well approximated by a harmonic oscillator. (b) Spectrum of the coupled harmonic oscillators.

up for more than one excitation in the system. To clarify this we consider the Hamiltonian for two coupled harmonic oscillators with creation operators $a^\dagger$ and $b^\dagger$ and with the same frequency ω_c [2.1]

$$\mathrm{H_{HO}} = \hbar\omega_c a^\dagger a + \hbar\omega_c b^\dagger b + \mathrm{i}\hbar g\sqrt{N}\left(a^\dagger b - a b^\dagger\right) \ . \tag{2.2.7}$$

The eigenstates are

$$|E_{n,m}\rangle = \frac{\left(a^\dagger - \mathrm{i}b^\dagger\right)^n \left(a^\dagger + \mathrm{i}b^\dagger\right)^m}{\sqrt{2^{n+m} n! m!}} \left|0\right\rangle_a \left|0\right\rangle_b \tag{2.2.8}$$

with eigenenergies

$$E_{n,m} = n\hbar\left(\omega_c - g\sqrt{N}\right) + m\hbar\left(\omega_c + g\sqrt{N}\right) \ . \tag{2.2.9}$$

The eigenenergies are sketched in Fig. 2.2(b) and are fundamentally different from the anharmonic spectrum of a single two-level system in a cavity shown in Fig. 2.1(b). Coherent excitation of the form $\mathrm{H_P} = \mathrm{i}\hbar\eta\left(\mathrm{e}^{-\mathrm{i}\omega t}a^\dagger - \mathrm{e}^{\mathrm{i}\omega t}a\right)$ causes resonances only at $\left(\omega_c - g\sqrt{N}\right)$ and $\left(\omega_c + g\sqrt{N}\right)$ as can be deduced from

$$\begin{aligned}
\mathrm{H_P}\left|E_{n,m}\right\rangle =& \mathrm{i}\hbar\eta\left(\mathrm{e}^{-\mathrm{i}\omega t}a^\dagger - \mathrm{e}^{\mathrm{i}\omega t}a\right)\frac{\left(a^\dagger - \mathrm{i}b^\dagger\right)^n\left(a^\dagger + \mathrm{i}b^\dagger\right)^m}{\sqrt{2^{n+m}n!m!}}\left|0\right\rangle_a\left|0\right\rangle_b \\
=& \mathrm{i}\hbar\eta\left[\mathrm{e}^{-\mathrm{i}\omega t}\frac{a^\dagger\left(a^\dagger - \mathrm{i}b^\dagger\right)^n\left(a^\dagger + \mathrm{i}b^\dagger\right)^m}{\sqrt{2^{n+m}n!m!}} - \mathrm{e}^{\mathrm{i}\omega t}\frac{a\left(a^\dagger - \mathrm{i}b^\dagger\right)^n\left(a^\dagger + \mathrm{i}b^\dagger\right)^m}{\sqrt{2^{n+m}n!m!}}\right]\left|0\right\rangle_a\left|0\right\rangle_b \\
=& \mathrm{i}\hbar\eta\left[\mathrm{e}^{-\mathrm{i}\omega t}\frac{\left(a^\dagger - \mathrm{i}b^\dagger + a^\dagger + \mathrm{i}b^\dagger\right)\left(a^\dagger - \mathrm{i}b^\dagger\right)^n\left(a^\dagger + \mathrm{i}b^\dagger\right)^m}{2\sqrt{2^{n+m}n!m!}}\right. \\
&\left. -\mathrm{e}^{\mathrm{i}\omega t}\frac{\left[\left(a^\dagger - \mathrm{i}b^\dagger\right)^n a + n\left(a^\dagger - \mathrm{i}b^\dagger\right)^{n-1}\right]\left(a^\dagger + \mathrm{i}b^\dagger\right)^m}{\sqrt{2^{n+m}n!m!}}\right]\left|0\right\rangle_a\left|0\right\rangle_b \\
=& \mathrm{i}\hbar\eta\left[\mathrm{e}^{-\mathrm{i}\omega t}\frac{\left(a^\dagger - \mathrm{i}b^\dagger\right)^{n+1}\left(a^\dagger + \mathrm{i}b^\dagger\right)^m + \left(a^\dagger - \mathrm{i}b^\dagger\right)^n\left(a^\dagger + \mathrm{i}b^\dagger\right)^{m+1}}{2\sqrt{2^{n+m}n!m!}}\right. \\
&-\mathrm{e}^{\mathrm{i}\omega t}\left(\frac{\left(a^\dagger - \mathrm{i}b^\dagger\right)^n\left[\left(a^\dagger + \mathrm{i}b^\dagger\right)^m a + m\left(a^\dagger + \mathrm{i}b^\dagger\right)^{m-1}\right]}{\sqrt{2^{n+m}n!m!}}\right. \\
&\left.\left. +\frac{n\left(a^\dagger - \mathrm{i}b^\dagger\right)^{n-1}\left(a^\dagger + \mathrm{i}b^\dagger\right)^m}{\sqrt{2^{n+m}n!m!}}\right)\right]\left|0\right\rangle_a\left|0\right\rangle_b \\
=& \mathrm{i}\hbar\eta\left[\mathrm{e}^{-\mathrm{i}\omega t}\frac{\left(a^\dagger - \mathrm{i}b^\dagger\right)^{n+1}\left(a^\dagger + \mathrm{i}b^\dagger\right)^m + \left(a^\dagger - \mathrm{i}b^\dagger\right)^n\left(a^\dagger + \mathrm{i}b^\dagger\right)^{m+1}}{2\sqrt{2^{n+m}n!m!}}\right. \\
&\left. -\mathrm{e}^{\mathrm{i}\omega t}\frac{m\left(a^\dagger - \mathrm{i}b^\dagger\right)^n\left(a^\dagger + \mathrm{i}b^\dagger\right)^{m-1} + n\left(a^\dagger - \mathrm{i}b^\dagger\right)^{n-1}\left(a^\dagger + \mathrm{i}b^\dagger\right)^m}{\sqrt{2^{n+m}n!m!}}\right]\left|0\right\rangle_a\left|0\right\rangle_b \ .
\end{aligned} \tag{2.2.10}$$

The coherent excitation couples the state $\left|E_{n,m}\right\rangle$ only to the states $\left|E_{n+1,m}\right\rangle$, $\left|E_{n,m+1}\right\rangle$, $\left|E_{n,m-1}\right\rangle$, and $\left|E_{n-1,m}\right\rangle$ for which the transition frequencies are $\left(\omega_c - g\sqrt{N}\right)$ and $\left(\omega_c + g\sqrt{N}\right)$. The spectrum shows this normal mode splitting until the pumping is so strong that the ensemble is pushed out of the regime where it can be described by a harmonic oscillator.

2.2.3. Superradiance

The radiative decay of a fully inverted ensemble has been widely studied in the context of superradiance. As the inverted ensemble starts to cascade down the ladder of Dicke states, the emission rate increases, resulting in a large pulse of radiation. This can be seen from

$$\mathrm{S}^{+}\,\mathrm{S}^{-}\,|J,M\rangle = (J+M)\,(J-M+1)\,|J,M\rangle \tag{2.2.11}$$

which is proportional to the spontaneous emission rate of the ensemble [2.7]. For $M = J$ we find the emission rate is $\propto N$ as $J = N/2$, for $M = 0$ however it is $\propto N^2$. This increase can be understood as a result of strong correlations between the atoms in the ensemble that build up during the emission process. The correlation between two atoms $\sigma_i^+ \sigma_j^-$ can be calculated via

$$\begin{aligned}\langle J,M|\,\mathrm{S}^{+}\,\mathrm{S}^{-}\,|J,M\rangle &= \langle J,M|\left(\sum_{i=1}^{N}\sigma_i^+\right)\left(\sum_{j=1}^{N}\sigma_j^-\right)|J,M\rangle \\ &= N\,(N-1)\,\langle J,M|\,\sigma_i^+\sigma_j^-\,|J,M\rangle + \langle J,M|\sum_i^N \sigma_i^+\sigma_i^-\,|J,M\rangle\end{aligned} \tag{2.2.12}$$

where the second term on the right hand side gives the number of excitations $J+M$. Thus the correlation between two spins is given by

$$\langle J,M|\,\sigma_i^+\sigma_j^-\,|J,M\rangle = \frac{J^2-M^2}{N\,(N-1)}\ , \tag{2.2.13}$$

where we used Eq. (2.2.11), and reaches the maximum value of $\approx 1/4$ for $M = 0$ [2.6]. In our case the ensemble does not emit into free space but predominantly into the cavity mode. The dynamics then strongly depends on the quality of the mirrors. For a large cavity decay rate the cavity stays basically empty all the time and acts as a loss channel. In a good cavity the ensemble and the mode will periodically exchange energy.

In the bad cavity limit the strong correlations provide the basis for superradiant lasers where a repumping mechanism is used to maintain superradiant emission. The excitations are predominantly stored in the ensemble, which is also the primary carrier of phase information [2.8, 2.9].

It has to be noted that the states with $J = N/2$ are only a small fraction of all possible states which also include states with $J < N/2$. The collective operators do not couple states with different J and in any description that solely relies on collective operators the states with $J < N/2$ will not be populated if in the initial state $J = N/2$. At the same time processes that are not collective processes, like the emission from independently radiatively damped atoms, cannot be described by collective operators alone [2.10].

2.3. Open quantum systems

There are powerful tools available to treat open quantum systems. The central starting point of all methods is the intuition that damping occurs as a result of the interaction with a large and complex environment. Thus it becomes clear that besides the ability to absorb energy the environment also exerts some sort of backaction on the system. Since the environment is large and its fluctuations are presumably uncorrelated, the backaction can be treated as a noise term. Here we follow the master equation approach and outline the important steps and assumptions for its derivation. The master equation determines the temporal evolution of the density operator describing a quantum system coupled to a bath. Both aspects, dissipation and fluctuations are reflected in the master equation approach.

2.3.1. Master equations

The system we are interested in, e.g. a cavity mode coupled to a spin or a cavity mode alone, is embedded in an environment that takes the role of a heat bath. The Hamiltonian for the system and the bath is

$$\mathrm{H}_{\mathrm{tot}} = \mathrm{H}_{\mathrm{S}} + \mathrm{H}_{\mathrm{B}} + \mathrm{V} \tag{2.3.1}$$

where V describes the interaction between the system and the bath. The dynamics of the density matrix χ for the whole system is determined by the von Neumann equation

$$\frac{\mathrm{d}}{\mathrm{d}t}\chi = \frac{1}{\mathrm{i}\hbar}\left[\mathrm{H}_{\mathrm{tot}}, \chi\right] \ . \tag{2.3.2}$$

Ultimately, we will only be interested in the dynamics of our small system. This leads to the definition of the reduced density matrix

$$\rho = \mathrm{tr}_{\mathrm{B}}\left[\chi\right] \ . \tag{2.3.3}$$

We restrict ourselves here to a short summary of the calculations necessary to derive the master equation. Equation (2.3.2) is transformed into the interaction picture

$$\tilde{\chi} = \mathrm{e}^{(\mathrm{i}/\hbar)(\mathrm{H_S} + \mathrm{H_B})t} \chi \mathrm{e}^{-(\mathrm{i}/\hbar)(\mathrm{H_S} + \mathrm{H_B})t} \tag{2.3.4}$$

to describe only the slow dynamics governed by the interaction Hamiltonian V

$$\frac{\mathrm{d}}{\mathrm{d}t}\tilde{\chi} = \frac{1}{\mathrm{i}\hbar}\left[\tilde{\mathrm{V}}, \tilde{\chi}\right] \ , \tag{2.3.5}$$

where

$$\tilde{\mathrm{V}} = \mathrm{e}^{(\mathrm{i}/\hbar)(\mathrm{H_S} + \mathrm{H_B})t}\, \mathrm{V}\, \mathrm{e}^{-(\mathrm{i}/\hbar)(\mathrm{H_S} + \mathrm{H_B})t} \ . \tag{2.3.6}$$

Equation (2.3.5) is formally integrated and the result is substituted inside the commutator of Eq. (2.3.5) to obtain an integro-differential equation for $\tilde{\chi}$ which reads

$$\frac{\mathrm{d}}{\mathrm{d}t}\tilde{\chi} = \frac{1}{\mathrm{i}\hbar}\left[\tilde{\mathrm{V}}\left(t\right), \tilde{\chi}\left(0\right)\right] - \frac{1}{\hbar^2}\int_0^t \mathrm{d}t' \left[\tilde{\mathrm{V}}\left(t\right), \left[\tilde{\mathrm{V}}\left(t'\right), \tilde{\chi}\left(t'\right)\right]\right] \tag{2.3.7}$$

Taking the partial trace of this equation leads to an equation for $\tilde{\rho}$, the reduced density operator of the system we are interested in, but which still depends on $\tilde{\chi}$ and all of its past. Note that the first term of Eq. (2.3.7) can be eliminated under the assumption that system and bath are uncorrelated at $t = 0$, i.e. $\tilde{\chi}\left(0\right) = \chi\left(0\right) = \rho\left(0\right) B_0$, with initial bath density operator B_0, and the assumption that the bath operators have zero mean in B_0 (which can be arranged by including a shift in the system Hamiltonian). The assumption that the system and the bath are initially uncorrelated and that the interaction is weak justifies the approximation that both systems will remain uncorrelated ($\tilde{\chi}\left(t\right) = \tilde{\rho}\left(t\right) B_0$). Moreover, as the system is thought to be very small compared to the bath, the state of the bath should be unaffected by the interaction. This approximations and assumptions simplify the equation for $\tilde{\rho}$, but the evolution of $\tilde{\rho}$ still depends on its own past. The physical reason for this is that, in principle, an earlier state of the system can leave its footprint in the state of the bath and be influenced by this modified bath later. However, in many situations the correlation time of the bath is short compared to the timescale on which the system evolves. This justifies the assumption that the evolution of $\tilde{\rho}$ is independent of its own past, a property it has in common with Markov processes. The approximation is therefore known as Markov-approximation.

Detailed information about the derivation can be found in [2.11, 2.12].

The master equation for a two-level system with spontaneous decay rate γ coupled to a lossy cavity with decay rate κ reads

$$\frac{\mathrm{d}}{\mathrm{d}t}\rho = \frac{1}{\mathrm{i}\hbar}\left[H,\rho\right] + \mathcal{L}\left[\rho\right] \ , \tag{2.3.8}$$

where H is the Hamiltonian from Eq. (2.1.1) and the Liouville superoperator is given by

$$\begin{aligned}\mathcal{L}\left[\rho\right] =& \mathcal{L}_{\text{cavity}}\left[\rho\right] + \mathcal{L}_{\text{spont}}\left[\rho\right] \\ =& \kappa\left(\bar{n}\left(\omega_c\right)+1\right)\left(2a\rho a^\dagger - a^\dagger a\rho - \rho a^\dagger a\right) \\ &+ \kappa\bar{n}\left(\omega_c\right)\left(2a^\dagger\rho a - aa^\dagger\rho - \rho aa^\dagger\right) \\ &+ \frac{\gamma}{2}\left(2\sigma^-\rho\sigma^+ - \sigma^+\sigma^-\rho - \rho\sigma^+\sigma^-\right) \ .\end{aligned} \tag{2.3.9}$$

We have already included the situation that the cavity is at finite temperature $T \neq 0$, resulting in the thermal occupation of the mode with $\bar{n}$ photons, where

$$\bar{n}\left(\omega\right) = \frac{\mathrm{e}^{-\frac{\hbar\omega}{k_B T}}}{1-\mathrm{e}^{-\frac{\hbar\omega}{k_B T}}} \ . \tag{2.3.10}$$

In the optical regime thermal excitations in general play no role. However, in the GHz regime, in which CPW resonators work, they must be considered. Each of the contributing terms in Eq. (2.3.9) can be assigned to a physical process. The terms proportional to $2a\rho a^\dagger$ and $2a^\dagger\rho a$ describe the transition rates from the states with $(n+1)$ and $(n-1)$ photons into the n photon state. The rates from the n photon state into the $(n+1)$ and $(n-1)$ states are proportional to $-(aa^\dagger\rho + \rho aa^\dagger)$ and $-(a^\dagger a\rho + \rho a^\dagger a)$. The third line of Eq. (2.3.9) accounts for spontaneous emission and, under the assumption that the atom is well isolated, does not include thermal photons.

2.3.2. Operator expectation values

The master equation describes the dynamics of the reduced density operator and is a common starting point for the study of dissipative quantum systems. For small systems the master equation may be solved directly. For larger systems this is out of question as, for example, the density matrix of N two-level atoms has the dimensionality $2^N \times 2^N$. For moderate system sizes a possible way to determine the behavior of a quantum system is the Monte Carlo wave function approach [2.12–2.14]. However, ensemble sizes of $N \approx 10^6 - 10^8$, that we intend to study, are still out of reach.

The approximation we chose to be able to describe our system is that we assume all atoms and their coupling rates to be identical. It is therefor neither necessary nor illuminating to describe N atoms separately. We illustrate this for the master equation

$$\frac{\mathrm{d}}{\mathrm{d}t}\rho = \frac{1}{\mathrm{i}\hbar}\left[H_{\mathrm{TC}}, \rho\right] + \mathcal{L}_{\mathrm{TC}}\left[\rho\right] \ , \tag{2.3.11}$$

with the Hamiltonian in Eq. (2.2.1) and

$$\begin{aligned} \mathcal{L}_{\mathrm{TC}}\left[\rho\right] =& \kappa\left(\bar{n}\left(\omega_c\right)+1\right)\left(2a\rho a^\dagger - a^\dagger a\rho - \rho a^\dagger a\right) \\ &+ \kappa\bar{n}\left(\omega_c\right)\left(2a^\dagger\rho a - aa^\dagger\rho - \rho aa^\dagger\right) \\ &- \frac{\gamma}{2}\sum_{j=1}^{N}\left(\sigma_j^+\sigma_j^-\rho + \rho\sigma_j^+\sigma_j^- - 2\sigma_j^-\rho\sigma_j^+\right) \ . \end{aligned} \tag{2.3.12}$$

In order to describe the dynamics of our system we derive operator expectation value equations, which are a simple way to get information from a master equation [2.12]. We calculate the expectation value equation for the cavity field

$$\begin{aligned} \frac{\mathrm{d}}{\mathrm{d}t}\langle a\rangle &= \mathrm{tr}\left(a\frac{\mathrm{d}}{\mathrm{d}t}\rho\right) \\ &= -\left(\kappa + \mathrm{i}\omega_c\right)\langle a\rangle - \mathrm{i}gN\left\langle\sigma_1^-\right\rangle \ , \end{aligned} \tag{2.3.13}$$

where we use cyclic permutations under the trace and the assumption that all atoms are equal, i.e. $\sum_{j=1}^{N}\sigma_j^- = N\sigma_1^-$. The inversion follows the equation

$$\frac{\mathrm{d}}{\mathrm{d}t}\langle\sigma_1^z\rangle = -2\mathrm{i}g\left(\left\langle\sigma_1^+ a\right\rangle - \left\langle\sigma_1^- a^\dagger\right\rangle\right) - \gamma\left(1 + \langle\sigma_i^z\rangle\right) \tag{2.3.14}$$

which couples to the new quantity $\left\langle\sigma_1^+ a\right\rangle$ that describes the exchange of excitations between the mode and the ensemble. Calculating the expectation value equation for $\left\langle\sigma_1^+ a\right\rangle$ will also yield third order expectation values. In order to obtain a closed set of equations that can be solved either analytically or numerically we have to truncate the set of equations at some point. This truncation can be done at different levels of complexity of the equations, depending on the underlying physical situation we need to describe. For example, the assumption of fixed $\langle \sigma_1^z \rangle = -1$ simplifies matters considerably, as we retain only the dynamics of coupled harmonic oscillators. Nevertheless, this assumption is valid and useful if we want to describe an ensemble which is only weakly excited, i.e. the number of excitations is much less than N.

In order to describe higher order expectation values we have to derive their equations and find a way to deal with expectation values of even higher order that emerge during the calculations. The truncation can be achieved by expanding higher order expectation values by means of lower order expectation values [2.9, 2.15]

$$\langle abc \rangle = \langle abc \rangle_c + \langle ab \rangle \langle c \rangle + \langle ac \rangle \langle b \rangle + \langle cb \rangle \langle a \rangle - 2 \langle a \rangle \langle b \rangle \langle c \rangle \ , \tag{2.3.15}$$

where $\langle \ \cdot \ \rangle_c$ denotes the joint cumulant. Expanding all higher order expectation values and neglecting the joint cumulants finally leads to a closed set of equations. Note that neglecting a joint cumulant is to neglect a correlation. If, for instance, we expand

$$\left\langle \sigma_1^+ \sigma_2^- \right\rangle = \left\langle \sigma_1^+ \sigma_2^- \right\rangle_c + \left\langle \sigma_1^+ \right\rangle \left\langle \sigma_2^- \right\rangle \tag{2.3.16}$$

and neglect $\left\langle \sigma_1^+ \sigma_2^- \right\rangle_c$, we would miss the atom-atom correlations that are responsible for superradiant emission. The derivation of a set of expectation value equations must be carried out up to the order one wishes to keep and to study. However, due to the growing number and complexity of the equations this becomes increasingly difficult unless further approximations are possible.

2.4. Strong coupling regime

The parameter regime where the rate at which a cavity and an atom exchange energy by far exceeds the loss rates of the cavity mirrors and the spontaneous decay rate of the atom, is called strong coupling regime, i.e. $g \gg \kappa, \gamma/2$. A photon that is emitted by the atom is rather reabsorbed than lost via the mirrors of the cavity or into other modes. This regime is characterized by

$$C_1 = \frac{g^2}{\gamma\kappa} \gg 1 \ ,$$

where C_1 is called the cooperativity parameter of the system. In terms of the spectrum of the Jaynes-Cummings model this means that the splitting between the states in Fig. 2.1(a) of $2\hbar g$ exceeds the width of the peaks, governed by κ and γ.

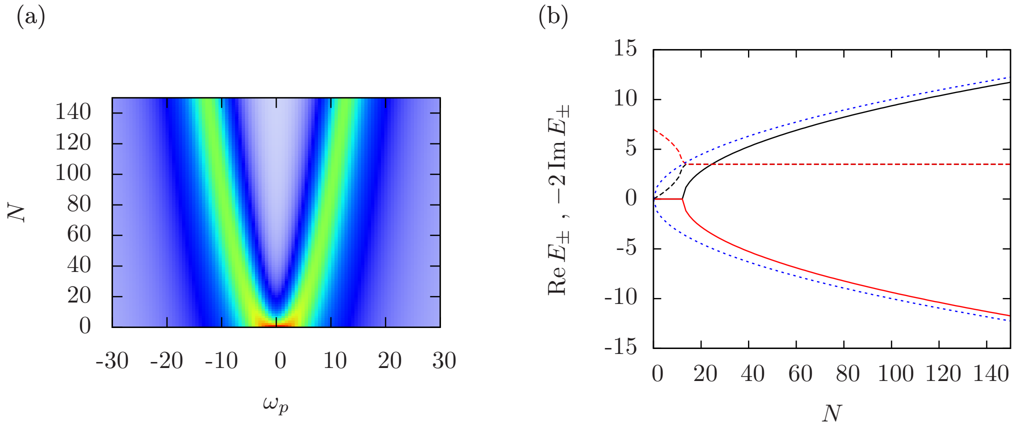

Figure 2.3.: (a): $\left|\langle a\rangle_{\mathrm{st}}\right|^2$ as a function of ω_p and N. (b): $\mathrm{Re}\,E_\pm$ solid lines (black/red) and $-2\,\mathrm{Im}\,E_\pm$ dashed lines (black/red) that correspond to the position and width of the normal mode resonances in the spectrum. In the limit of strong coupling the splitting approaches $2g\sqrt{N}$. As a reference $\pm g\sqrt{N}$ is shown as blue dashed line. The parameters were chosen to $\omega_a = \omega_c = 0$, $\kappa = 5$, $\gamma = 4$, $g = 1$, and $\eta = 1$.

Why is it that we are interested in reaching the strong coupling regime? The strong coupling regime allows for the basic operations needed for the storage of photons and the generation of entangled states between the light field and the atom. By controlling the interaction time between both subsystems, Rabi oscillations can be used to perform complex atom-field interactions. However, the condition $C_1 \gg 1$ is very restrictive in terms of possible experimental setups. The implementation based on Rydberg atoms coupled to a microwave cavity constitutes a successful realization [2.16]. The step towards ensembles of atoms makes more systems available, as the $\sqrt{N}$ enhancement of the coupling comes into play. The condition for collective strong coupling is given by

$$C = NC_1 \gg 1 \ ,$$

which can be met even for very small g with a sufficient number of spins N. As already mentioned in Sec. 2.2.1 the excitation spectrum of the coupled ensemble-cavity system in the weak excitation limit is equivalent to the spectrum of two coupled harmonic oscillators. As long as the number excitations is small compared to N, this description is valid. The coupling to a whole ensemble could therefore allow for the storage of many photons. Storage and retrieval of classical microwave pulses (i.e. far from the single photon limit) has already been demonstrated successfully with the electron spins of nitrogen enclosed in fullerene cages [2.17].

To illustrate the transition to the collective strong coupling regime we look at the steady state field inside a cavity driven by a weak probe field of frequency ω_p and strength η. The cavity is coupled to an ensemble of N identical atoms. The equation for the field

$$\begin{aligned}\frac{\mathrm{d}}{\mathrm{d}t}\langle a\rangle &= \mathrm{tr}\left(a\frac{\mathrm{d}}{\mathrm{d}t}\rho\right) && (2.4.1)\\ &= -\left(\kappa+\mathrm{i}\Delta_c\right)\langle a\rangle - \mathrm{i}gN\left\langle\sigma_1^-\right\rangle + \eta && (2.4.2)\end{aligned}$$

couples to

$$\frac{\mathrm{d}}{\mathrm{d}t}\left\langle\sigma_1^-\right\rangle = -\left(\frac{\gamma}{2}+\mathrm{i}\Delta_a\right)\left\langle\sigma_1^-\right\rangle - \mathrm{i}g\langle a\rangle \tag{2.4.3}$$

where we already used the weak excitation assumption $\langle\sigma_1^z\rangle = -1$ and introduced $\Delta_c = \omega_c - \omega_p$ and $\Delta_a = \omega_a - \omega_p$. The steady state field reads

$$\begin{aligned}\langle a\rangle_{\mathrm{st}} &= \frac{\eta}{\left(\kappa+\mathrm{i}\Delta_c\right) + \frac{g^2N}{\left(\frac{\gamma}{2}+\mathrm{i}\Delta_a\right)}}\\ &= \frac{\eta}{\left(\omega_p - E_+\right)\left(\omega_p - E_-\right)} && (2.4.4)\end{aligned}$$

with the complex poles

$$E_\pm = \frac{1}{2}\left(\omega_a+\omega_c\right) - \frac{1}{2}\mathrm{i}\left(\frac{\gamma}{2}+\kappa\right) \pm \sqrt{g^2N - \frac{1}{4}\left(\frac{\gamma}{2}+\kappa+\mathrm{i}\left(\omega_a-\omega_c\right)\right)^2}\,. \tag{2.4.5}$$

In Fig. 2.3(a) we depict $|\langle a\rangle_{\mathrm{st}}|^2$ as a function of ω_p and N. With increasing N the splitting of the normal modes becomes visible. The regime of oscillations is entered for $g^2N > \frac{1}{4}\left(\frac{\gamma}{2}+\kappa\right)^2$, as can be seen in Fig. 2.3(b). The width of the peaks then is $-2\,\mathrm{Im}\,E_\pm = \frac{\gamma}{2}+\kappa$ [2.18]. In the limit of $g\sqrt{N} \gg \kappa, \gamma/2$ the normal mode splitting approaches $2g\sqrt{N}$. In experiments, the detection of the two-peaked spectrum is usually considered a hallmark for the achievement of strong coupling.

2.5. Cavity emission spectrum

The spectrum of the cavity emission is an important quantity for the characterization of the ongoing dynamics. Moreover, in some experiments the light emitted by the cavity is the only source of information that is accessible. There are different ways of probing a cavity to infer the energy eigenstates, one of them was already described in Sec. 2.4. A probe beam with tunable frequency ω_p excites the coupled system and results in an increased transmission signal whenever a resonance is approached. This is a common procedure in experiments and was also used for the acquisition of the data shown in Sec. 4 and Sec. 5.

Here we briefly discuss the calculation of the cavity emission spectrum by using the Wiener-Khintchine theorem and the quantum regression theorem. Assuming that we deal with stationary and ergodic processes, the spectrum is given by the Fourier transform of the two-time correlation function of the cavity emission

$$\mathrm{S}(\omega) = \frac{1}{2\pi}\int_{-\infty}^{\infty} \mathrm{d}\tau \mathrm{e}^{\mathrm{i}\omega\tau} \left\langle a^\dagger(\tau)\, a(0)\right\rangle \ . \tag{2.5.1}$$

In general the spectrum of a coherently driven cavity is comprised of a coherent and an incoherent part

$$\mathrm{S}(\omega) = \mathrm{S}_{\mathrm{coh}}(\omega) + \mathrm{S}_{\mathrm{inc}}(\omega) \tag{2.5.2}$$

where the coherent part is proportional to a δ-function and located at the driving frequency. In the following we study an incoherently driven cavity, thereby keeping the total phase invariance that allows to assume $\langle a\rangle = \left\langle \sigma_j^\pm\right\rangle = 0$. To calculate the incoherent spectrum of the cavity emission it is necessary to determine the two-time correlation function $\left\langle a^\dagger(\tau)\, a(0)\right\rangle$. The quantum regression theorem states that for linear systems the correlation function $\langle A(t+\tau)\, B(t)\rangle$ with $\tau > 0$ follows the same equation, as a function of τ, as $\langle A(t+\tau)\rangle$ does [2.10]. This implies that from the complex conjugate of Eq. (2.3.13) and by using the stationarity assumption we obtain

$$\frac{\mathrm{d}}{\mathrm{d}\tau}\left\langle a^\dagger(\tau)\, a(0)\right\rangle = -\left(\kappa - \mathrm{i}\omega_c\right)\left\langle a^\dagger(\tau)\, a(0)\right\rangle + \mathrm{i}gN\left\langle \sigma_1^+(\tau)\, a(0)\right\rangle \ , \tag{2.5.3}$$

which couples to the correlation function $\left\langle \sigma_1^+(\tau)\, a(0)\right\rangle$. Analogously to Eq. (2.5.3) we calculate

$$\begin{aligned}\frac{\mathrm{d}}{\mathrm{d}\tau}\left\langle \sigma_1^+(\tau)\, a(0)\right\rangle &= -\left(\frac{w+\gamma}{2} - \mathrm{i}\omega_a\right)\left\langle \sigma_1^+(\tau)\, a(0)\right\rangle - \mathrm{i}g\left\langle \sigma_1^z(\tau)\, a^\dagger(\tau)\, a(0)\right\rangle \\ &= -\left(\frac{w+\gamma}{2} - \mathrm{i}\omega_a\right)\left\langle \sigma_1^+(\tau)\, a(0)\right\rangle - \mathrm{i}g\left\langle \sigma_1^z(\tau)\right\rangle\left\langle a^\dagger(\tau)\, a(0)\right\rangle \ ,\end{aligned} \tag{2.5.4}$$

where we expanded the second term according to Eq. (2.3.15), neglected the cumulant and used the total phase invariance. Equation (2.5.4) also features an incoherent pump rate w that is included in the Liouvillian as an inverse spontaneous decay. For details see Sec. 3.7. Written in matrix form we find

$$\frac{\mathrm{d}}{\mathrm{d}\tau}\begin{pmatrix}\left\langle a^{\dagger}(\tau)\,a(0)\right\rangle\\ \left\langle \sigma_1^{+}(\tau)\,a(0)\right\rangle\end{pmatrix}=\begin{pmatrix}-(\kappa-\mathrm{i}\omega_c) & \mathrm{i}gN\\ -\mathrm{i}g\left\langle\sigma_1^{z}\right\rangle_{\mathrm{st}} & -\left(\frac{w+\gamma}{2}-\mathrm{i}\omega_a\right)\end{pmatrix}\begin{pmatrix}\left\langle a^{\dagger}(\tau)\,a(0)\right\rangle\\ \left\langle \sigma_1^{+}(\tau)\,a(0)\right\rangle\end{pmatrix}. \tag{2.5.5}$$

Due to stationarity we set $\left\langle\sigma_1^z(\tau)\right\rangle=\left\langle\sigma_1^z\right\rangle_{\mathrm{st}}$. The simplest way to proceed is to use the Laplace transform on Eq. (2.5.5) and then to solve for $\left\langle a^{\dagger}a\right\rangle(s)$. For $s=-\mathrm{i}\omega$ we obtain the Fourier transform of the correlation function. The Laplace transform of Eq. (2.5.5) reads

$$\begin{pmatrix}s+(\kappa-\mathrm{i}\omega_c) & -\mathrm{i}gN\\ \mathrm{i}g\left\langle\sigma_1^{z}\right\rangle_{\mathrm{st}} & s+\left(\frac{w+\gamma}{2}-\mathrm{i}\omega_a\right)\end{pmatrix}\begin{pmatrix}\left\langle a^{\dagger}a\right\rangle(s)\\ \left\langle \sigma_1^{+}a\right\rangle(s)\end{pmatrix}=\begin{pmatrix}\left\langle a^{\dagger}a\right\rangle_{\mathrm{st}}\\ \left\langle \sigma_1^{+}a\right\rangle_{\mathrm{st}}\end{pmatrix}. \tag{2.5.6}$$

With Cramers rule we arrive at

$$\left\langle a^{\dagger}a\right\rangle(s)=\frac{\left\langle a^{\dagger}a\right\rangle_{\mathrm{st}}\left(s+\frac{w+\gamma}{2}-\mathrm{i}\omega_a\right)-\mathrm{i}gN\left\langle\sigma_1^{+}a\right\rangle_{\mathrm{st}}}{(s+\kappa-\mathrm{i}\omega_c)\left(s+\frac{w+\gamma}{2}-\mathrm{i}\omega_a\right)-g^2N\left\langle\sigma_1^{z}\right\rangle_{\mathrm{st}}}. \tag{2.5.7}$$

The steady state quantities in Eq. (2.5.7) have to be determined either analytically or numerically, depending on the complexity of the problem. Since the spectrum is proportional to $\left(\left\langle a^{\dagger}a\right\rangle(s)+\mathrm{c.c.}\right)$ it is worthwhile to look at the result in some limiting cases (we restrict the discussion to the resonant situation $\omega_c=\omega_a$ and simplify the notation by defining the frequency axis with respect to ω_c) [2.19]. By rewriting Eq. (2.5.7) we find the very general formula

$$\left\langle a^{\dagger}a\right\rangle(s)=\frac{\left\langle a^{\dagger}a\right\rangle_{\mathrm{st}}\left(s+\frac{w+\gamma}{2}\right)-\mathrm{i}gN\left\langle\sigma_1^{+}a\right\rangle_{\mathrm{st}}}{s^2+s\left(\kappa+\frac{w+\gamma}{2}\right)+\kappa\frac{w+\gamma}{2}-g^2N\left\langle\sigma_1^{z}\right\rangle_{\mathrm{st}}} \tag{2.5.8}$$

that offers some insight into the ongoing physics:

Case 1: $\frac{w+\gamma}{2}, \kappa \gg s$. In the numerator of Eq. (2.5.8) we can neglect s compared to $\frac{w+\gamma}{2}$. Together with the reduced denominator this reads

$$\left\langle a^\dagger a\right\rangle(s) \approx \frac{1}{\kappa+\frac{w+\gamma}{2}} \frac{\left\langle a^\dagger a\right\rangle_{\mathrm{st}} \frac{w+\gamma}{2} - \mathrm{i}gN\left\langle \sigma_1^+ a\right\rangle_{\mathrm{st}}}{s+\frac{\kappa\frac{w+\gamma}{2}-g^2N\left\langle\sigma_1^z\right\rangle_{\mathrm{st}}}{\kappa+\frac{w+\gamma}{2}}} \,. \tag{2.5.9}$$

The resulting spectrum is a Lorentzian with a width (FWHM) of

$$\Gamma = \frac{2}{\kappa+\frac{w+\gamma}{2}}\left[\kappa\frac{w+\gamma}{2} - g^2N\left\langle\sigma_1^z\right\rangle_{\mathrm{st}}\right] \,. \tag{2.5.10}$$

For low pumping rates w we find $\langle\sigma_1^z\rangle_{\mathrm{st}} \approx -1$ which leads to a very large linewidth. For $w > \gamma$ we obtain $\langle\sigma_1^z\rangle_{\mathrm{st}} > 0$, thereby reducing the linewidth of the emission. The reduction takes place until the inversion saturates, i.e. $\langle\sigma_1^z\rangle_{\mathrm{st}} = 1$ and the linewidth grows with increasing w. This behavior is shown in Sec. 3.13 in Fig. 3.15.

Case 2: $\frac{w+\gamma}{2}, \kappa \ll s = -\mathrm{i}\omega \approx \mp\mathrm{i}g\sqrt{N}$. In the numerator only the part proportional to s is kept. We write

$$\begin{aligned}\left\langle a^\dagger a\right\rangle(s) &\approx \frac{s\left\langle a^\dagger a\right\rangle_{\mathrm{st}}}{s^2+s\left(\kappa+\frac{w+\gamma}{2}\right)-g^2N\left\langle\sigma_1^z\right\rangle_{\mathrm{st}}} \\ &= \frac{-\mathrm{i}\omega\left\langle a^\dagger a\right\rangle_{\mathrm{st}}}{g^2N-\omega^2-\mathrm{i}\omega\left(\kappa+\frac{w+\gamma}{2}\right)} \,,\end{aligned} \tag{2.5.11}$$

where we again used that for low pumping we get $\langle\sigma_1^z\rangle_{\mathrm{st}} \approx -1$ [2.19]. With $g^2N - \omega^2 = \left(g\sqrt{N}+\omega\right)\left(g\sqrt{N}-\omega\right)$ we get

$$\left\langle a^\dagger a\right\rangle(-\mathrm{i}\omega) \approx \frac{-\mathrm{i}\omega\left\langle a^\dagger a\right\rangle_{\mathrm{st}}}{\left(g\sqrt{N}+\omega\right)\left(g\sqrt{N}-\omega\right)-\mathrm{i}\omega\left(\kappa+\frac{w+\gamma}{2}\right)} \,. \tag{2.5.12}$$

For $\omega \approx \pm g\sqrt{N}$ we find

$$\left\langle a^\dagger a\right\rangle\left(\mp\mathrm{i}g\sqrt{N}\right) \approx \mp\frac{1}{2}\frac{\mathrm{i}\left\langle a^\dagger a\right\rangle_{\mathrm{st}}}{\left(g\sqrt{N}\mp\omega\right)\mp\frac{\mathrm{i}}{2}\left(\kappa+\frac{w+\gamma}{2}\right)} \,. \tag{2.5.13}$$

Which corresponds to a spectrum with two peaks, separated by $2g\sqrt{N}$, each having a width of $\Gamma' = \left(\kappa + \frac{w+\gamma}{2}\right)$ (FWHM).

The spectrum of the system of spins coupled to the mode shows quite different behavior depending on the parameter regime in which we study it. In the limit of $\gamma \ll \kappa$ Case 1 corresponds to a bad cavity laser [2.9, 2.20]. Case 2 features the Rabi peaks of the collective strong coupling regime that were already discussed in Sec. 2.4.

The calculation of the spectrum becomes more complicated for the case of a coherently driven cavity, where we have a defined phase. The correlation function $\left\langle a^{\dagger}\left(\tau\right)a\left(0\right)\right\rangle$ then couples to the quantities $\left\langle \sigma_1^{+}\left(\tau\right)a\left(0\right)\right\rangle$, $\left\langle a\left(\tau\right)a\left(0\right)\right\rangle$, $\left\langle \sigma_1^{-}\left(t\right)a\left(0\right)\right\rangle$ and $\left\langle \sigma_1^{z}\left(\tau\right)a\left(0\right)\right\rangle$, but in essence the approach is the same. The steady state values necessary for the calculation have to be determined from a more complicated set of equations, since the assumption of total phase invariance is no longer valid, for details see Sec. 3.10. The spectrum of a coherently driven cavity containing N atoms is addressed in detail in [2.1], but in the language of Fokker-Planck equations.

2.6. Experimental Implementations

In general many possible implementations can be envisaged. However, here we concentrate on two special cases of different ensembles coupled to CPW resonators. The intention of this introduction is to point out what the promising innovations of this implementations are and which properties require special attention in the theoretical treatment.

2.6.1. Coplanar waveguide resonators

The resonators considered for the most part of this work are so-called coplanar waveguide resonators (CPW resonators). They consist of two ground planes and a central wire that are made of a superconducting material, for example Niobium. The center conductor is coupled to input and output channels via gap capacitors and has a length of a few centimeters corresponding to a resonance frequency in the GHz regime.

The CPW resonators have a very small mode volume, as the field is strongly localized in the vicinity of the chip surface. This results in a large field per photon which is proportional to the coupling strength g. The temperatures at which CPW resonators are operated are usually in the mK regime. However, in Sec. 3 the influence of thermal excitations in experiments with CPW resonators at higher temperatures is discussed. The motivation for this analysis is that the technical challenges connected with working in the mK regime are such that some configurations, for example the one described in Sec. 2.6.2, are extremely hard to realize. It is therefore worthwhile to study what can still be observed when working at higher temperature.

Strong coupling between a CPW resonator and a superconducting qubit has been successfully demonstrated by several groups [2.21, 2.22]. A superconducting qubit consists of a small island or a loop of superconducting material that has a very anharmonic internal energy level structure such that the lowest two states can be well approximated by a two-level system. The states can be represented by the number of cooper pairs on the superconducting island (charge qubit) or the orientation of the charge flow in the loop (flux qubit). The CPW resonator can also be used to mediate the coupling between two superconducting qubits [2.23]. This field of research is usually referred to as circuit quantum electrodynamics [2.24]. Here, the cavity already has been used as a bus to connect superconducting qubits. The next logical step is to establish the connection with systems well known from atom-based quantum optics, again using the cavity as a bus. Interconnecting elements from circuit quantum electrodynamics and atomic quantum optics could be a possible way to combine the individual advantages of both systems [2.25, 2.26].

2.6.2. Rubidium Ensemble

Here we introduce a particular example of a hybrid quantum system based on a CPW resonator coupling to an ensemble of ultracold ^{87}Rb atoms [2.26]. The magnetic hyperfine transition between the states $|F=1, m_F\rangle$ and $|F=2, m'_F\rangle$, with transition frequency $f_a = 6.83$ GHz, is well suited for the coupling to the CPW resonator. The transverse field of the mode induces transitions with $\Delta m_F = m_F - m'_F = \pm 1$ of which one is selected to be in resonance with the resonator mode by applying a magnetic bias field. The cloud of atoms has to be placed close to the surface of the resonator. The confinement of the atoms near the chip surface is accomplished by wire traps that can be integrated into the chip [2.27]. Depending on the efficiency of the initial trapping and transport procedure the ensemble can contain $N = 10^6 - 10^8$ atoms.

The atoms are very well isolated from any thermal contact, therefore thermal exci-

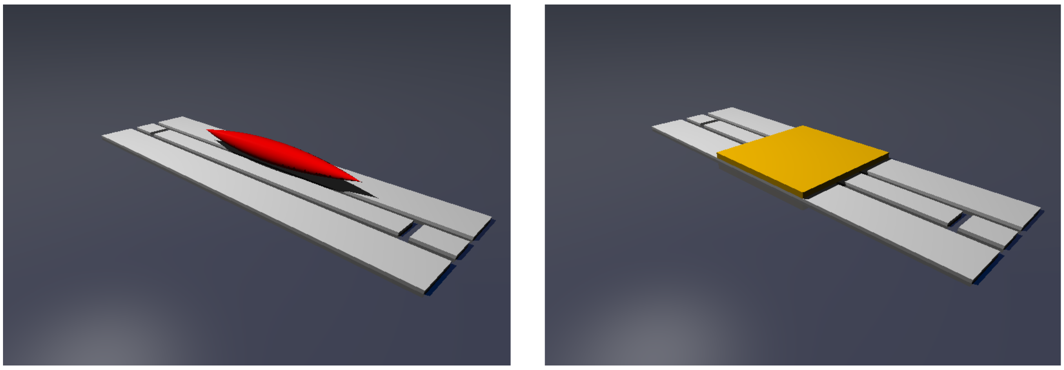

Figure 2.4.: Sketch of the experimental implementations described in Sec. 2.6.2 and Sec. 2.6.3. On the left the CPW resonator with the cloud of ^{87}Rb atoms is depicted. The atoms are trapped close to the surface to ensure sufficient overlap with the mode volume. On the right the atomic cloud is replaced by a diamond containing a high density of NV centers. The diamond can be fixed directly to the chip surface, simplifying the experimental procedure considerably.

tations of the ensemble are not considered. However, the thermal occupation of the mode must be taken into account in the theoretical description, since the resonator is in contact with the rest of the setup at finite temperature. In the experiment some care has to be taken with the cable connection to the resonator to avoid additional heating due to the contact with measurement devices at room temperature.

The results of the theoretical considerations in preparation for the experimental realization are presented in Sec. 3. Moreover, prospects for the implementation of a narrow-linewidth micromaser are discussed.

2.6.3. Nitrogen-Vacancy Centers

Nitrogen vacancy (NV) centers are point defects in the crystal structure of a diamond. Each defect consists of a nitrogen atom replacing a carbon atom and a neighboring vacant lattice site. The electronic structure of NVs has been intensively studied in the recent years [2.28, 2.29]. Here we are interested in NV centers in the negative charge state, where an additional electron from the surrounding crystal and one of the vacancy electrons form a spin $S = 1$ pair. The ground state is a spin triplet where the $m_S = \pm 1$ states are split from the $m_S = 0$ state by approximately 2.88 GHz, as can be seen in Fig. 2.5(a). The splitting is caused by strong spin-spin interaction with the remaining vacancy electrons. A homogeneous magnetic field allows to tune one of the transitions $m_S = 0 \rightarrow m_S = \pm 1$ into resonance with

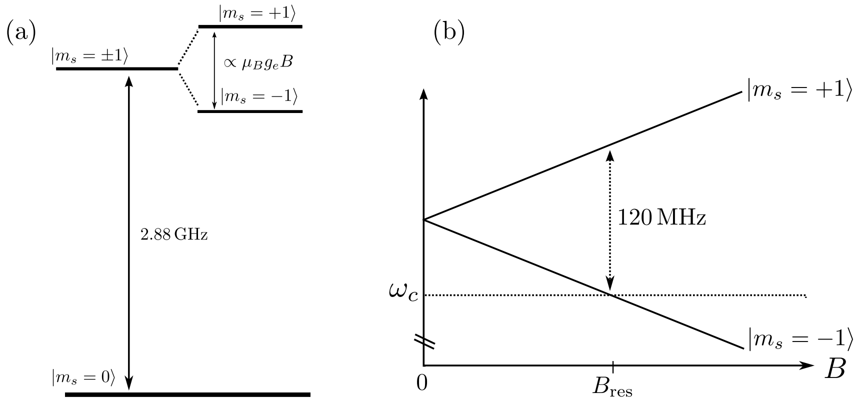

Figure 2.5.: (a) Ground state triplet of the negatively charged NV center. (b) On of the $m_S = 0 \rightarrow m_S = \pm 1$ transitions can be tuned into resonance with the cavity (at $\omega_c/(2\pi) = 2.7$ GHz) by means of a homogeneous magnetic field.

the cavity. In Fig. 2.5(b), the shift of the transition frequencies is indicated. The off-resonant transition causes a frequency shift of the mode.

The NV center can have four different orientations in the crystal due to the symmetry of the unit cell in diamond. An ensemble of NVs is therefore in general divided into four subensembles, each tuning differently, as they enclose four different angles with the applied magnetic field. It is possible to find an orientation of the diamond on the chip so that two of the four subensemble enclose the same angle with the field. The diamond is fixed directly to the chip surface to maximize the overlap between the mode volume and the crystal. The number of NVs coupled to the mode is approximately $N = 10^{12}$. Another important feature of the NV ensemble is the inhomogeneous frequency distribution, having a width of approximately 10 MHz, that can be attributed to local variations of the crystal field. Some of these variations are closely connected to the fabrication process of the sample, where a diamond containing a high concentration of nitrogen is irradiated with neutrons. The neutrons cause the defects necessary to form the NV centers in a subsequent annealing process at about 900 °C. Some of the defects caused by the radiation remain and the majority of the nitrogen atoms is not converted to NV centers. Therefore each NV is surrounded by a different environment, leading to uncontrollable frequency shifts. The exact mechanisms of the inhomogeneous broadening are not yet fully understood and might also have a dynamic component. One has to keep in mind that NVs in the negative charge state can be converted to the neutral charge state, which behaves differently. Experiments at room temperature show that intense radiation at 514 nm switches neutral NVs to the negative charge state, from which they relax back after switching off the irradiation [2.30]. The role of such processes at cryogenic temperatures is yet unknown.

The strong coupling of an NV ensemble to a resonator has been successfully demonstrated in recent years [2.31, 2.32]. For ensembles of other impurity spins the strong coupling regime could also be reached [2.33, 2.34].

For the theoretical description of the system it is necessary to find an appropriate description of the inhomogeneous frequency distribution. Moreover, the ensemble spins couple to a finite temperature bath because the sample is in direct contact with the chip surface. Terms describing this coupling have to be included into the master equation. The results of the experimental and theoretical work on NV center ensembles are presented in Sec. 4 and Sec. 5.

References for Chapter 2

[2.1] H.J. Carmichael. *Statistical Methods in Quantum Optics: Non-classical fields.* Vol. 2. Springer Verlag, 2007.

[2.2] L. Tian and H.J. Carmichael. "Quantum trajectory simulations of two-state behavior in an optical cavity containing one atom." In: *Physical Review A* 46.11 (1992), R6801.

[2.3] A. Faist et al. "Coherent radiation in interaction with two-level system." In: *Helv. Phys. Acta* 45 (1972), p. 956.

[2.4] J.H. Eberly, N.B. Narozhny, and J.J. Sanchez-Mondragon. "Periodic spontaneous collapse and revival in a simple quantum model." In: *Physical Review Letters* 44.20 (1980), pp. 1323–1326.

[2.5] R.H. Dicke. "Coherence in spontaneous radiation processes." In: *Physical Review* 93.1 (1954), pp. 99–110.

[2.6] S. Haroche and J.M. Raimond. *Exploring the quantum: atoms, cavities and photons.* Oxford University Press, USA, 2006.

[2.7] M. Gross and S. Haroche. "Superradiance: an essay on the theory of collective spontaneous emission." In: *Physics Reports* 93.5 (1982), pp. 301–396.

[2.8] J.G. Bohnet et al. "A steady-state superradiant laser with less than one intracavity photon." In: *Nature* 484.7392 (2012), pp. 78–81.

[2.9] D. Meiser et al. "Prospects for a millihertz-linewidth laser." In: *Physical Review Letters* 102.16 (2009), p. 163601.

[2.10] H.J. Carmichael. *Statistical methods in quantum optics 1: Master Equations and Fokker-Planck Equations.* Springer, 1999.

[2.11] C.C. Tannoudji, G. Grynberg, and J. Dupont-Roe. “Atom-photon interactions.” In: (1992).

[2.12] H.J. Carmichael. *An open systems approach to quantum optics: lectures presented at the Université libre de Bruxelles, October 28 to November 4, 1991.* Vol. 18. Springer, 1993.

[2.13] C.W. Gardiner, A.S. Parkins, and P. Zoller. “Wave-function quantum stochastic differential equations and quantum-jump simulation methods.” In: *Physical Review A* 46.7 (1992), p. 4363.

[2.14] A. Vukics and H. Ritsch. “C++ QED: an object-oriented framework for wave-function simulations of cavity QED systems.” In: *The European Physical Journal D-Atomic, Molecular, Optical and Plasma Physics* 44.3 (2007), pp. 585–599.

[2.15] R. Kubo. “Generalized cumulant expansion method.” In: *J. Phys. Soc. Japan* 17.7 (1962), pp. 1100–1120.

[2.16] J.M. Raimond, M. Brune, and S. Haroche. “Manipulating quantum entanglement with atoms and photons in a cavity.” In: *Reviews of Modern Physics* 73.3 (2001), p. 565.

[2.17] H. Wu et al. “Storage of multiple coherent microwave excitations in an electron spin ensemble.” In: *Physical Review Letters* 105.14 (2010), p. 140503. ISSN: 1079-7114.

[2.18] Z. Kurucz, J.H. Wesenberg, and K. Mølmer. “Spectroscopic properties of inhomogeneously broadened spin ensembles in a cavity.” In: *Physical Review A* 83.5 (2011), p. 053852.

[2.19] P. Meystre and M. Sargent. *Elements of quantum optics.* Springer Verlag, 2007.

[2.20] K. Henschel et al. “Cavity QED with an ultracold ensemble on a chip: Prospects for strong magnetic coupling at finite temperatures.” In: *Physical Review A* 82.3 (2010), p. 033810.

[2.21] A. Wallraff et al. “Strong coupling of a single photon to a superconducting qubit using circuit quantum electrodynamics.” In: *Nature* 431.7005 (2004), pp. 162–167.

[2.22] J. Majer et al. “Coupling superconducting qubits via a cavity bus.” In: *Nature* 449.7161 (2007), pp. 443–447. ISSN: 0028-0836. DOI: `10.1038/nature06184`. URL: `http://dx.doi.org/10.1038/nature06184`.

[2.23] J. Majer et al. “Coupling superconducting qubits via a cavity bus.” In: *Nature* 449.7161 (2007), pp. 443–447.

[2.24] R.J. Schoelkopf and S.M. Girvin. “Wiring up quantum systems.” In: *Nature* 451.7179 (2008), pp. 664–669.

[2.25] P. Rabl et al. “Hybrid Quantum Processors: Molecular Ensembles as Quantum Memory for Solid State Circuits.” In: *Phys. Rev. Lett.* 97 (3 2006), p. 033003. DOI: `10.1103/PhysRevLett.97.033003`. URL: `http://link.aps.org/doi/10.1103/PhysRevLett.97.033003`.

[2.26] J. Verdu et al. “Strong Magnetic Coupling of an Ultracold Gas to a Superconducting Waveguide Cavity.” In: *Physical Review Letters* 103.4, 043603 (2009), p. 043603. DOI: `10.1103/PhysRevLett.103.043603`. URL: `http://link.aps.org/abstract/PRL/v103/e043603`.

[2.27] R. Folman et al. “Controlling cold atoms using nanofabricated surfaces: atom chips.” In: *Physical review letters* 84.20 (2000), pp. 4749–4752.

[2.28] F. Jelezko et al. “Observation of coherent oscillations in a single electron spin.” In: *Physical review letters* 92.7 (2004), p. 76401.

[2.29] F. Jelezko and J. Wrachtrup. “Single defect centres in diamond: A review.” In: *physica status solidi (a)* 203.13 (2006), pp. 3207–3225.

[2.30] T. Gaebel et al. “Photochromism in single nitrogen-vacancy defect in diamond.” In: *Applied Physics B: Lasers and Optics* 82.2 (2006), pp. 243–246.

[2.31] Y. Kubo et al. “Strong coupling of a spin ensemble to a superconducting resonator.” In: *Physical Review Letters* 105.14 (2010), p. 140502.

[2.32] R. Amsüss et al. “Cavity QED with Magnetically Coupled Collective Spin States.” In: *Physical Review Letters* 107.6 (2011), pp. 1–5. DOI: `10.1103/PhysRevLett.107.060502`. URL: `http://link.aps.org/doi/10.1103/PhysRevLett.107.060502`.

[2.33] D.I. Schuster et al. “High-Cooperativity Coupling of Electron-Spin Ensembles to Superconducting Cavities.” In: *Physical review letters* 105.14 (2010), p. 140501.

[2.34] P. Bushev et al. “Ultralow-power spectroscopy of a rare-earth spin ensemble using a superconducting resonator.” In: *Physical Review B* 84.6 (2011), p. 060501.

3. Publication

PHYSICAL REVIEW A (2010)

Cavity QED with an ultracold ensemble on a chip: prospects for strong magnetic coupling at finite temperatures[†]

Kathrin Henschel[1], Johannes Majer[2], Jörg Schmiedmajer[2], Helmut Ritsch[1]

[1] *Institute for Theoretical Physics, University of Innsbruck*
Technikerstr. 25, 6020 Innsbruck, Austria
[2] *Atominstitut, TU-Wien, Stadionallee 2,*
1020 Vienna, Austria

We study the nonlinear dynamics of an ensemble of cold trapped atoms with a hyperfine transition magnetically coupled to a resonant microwave cavity mode. Despite the minute single atom coupling one obtains strong coupling between collective hyperfine qubits and microwave photons enabling coherent transfer of an excitation between the long lived atomic qubit state and the mode. Evidence of strong coupling can be obtained from the cavity transmission spectrum even at finite thermal photon number. The system makes it possible to study further prominent collective phenomena such as superradiant decay of an inverted ensemble or the building of a narrowband stripline micromaser locked to an atomic hyperfine transition.

PACS numbers: 37.30.+i, 42.50.Pq

3.1. Introduction

The idea of resonant coupling of an ensemble of atoms to a single cavity mode has been addressed in numerous aspects and contexts, some dating back several decades [3.1]. Recently, in the context of quantum information processing, such

---

[†] The author of the present thesis performed all of the calculations in this publication.

Hamiltonians attracted renewed attention because the ensemble can serve as quantum memory with long coherence times [3.2–3.5]. Despite small coupling of individual atoms, the strong collective coupling of the ensemble to a particular cavity mode allows for the coherent transfer of an excitation to the ensemble, its storage and its retrieval after some time shorter than the coherence time of the system. Hence, due to collective effects, one can utilize atomic transitions and geometries for which the strong coupling regime would not be accessible otherwise.

As a particularly striking example, one can even envisage the use of states that are very weakly coupled to the field, for example, an optically forbidden hyperfine transition, which only couple to the field via magnetic dipole interaction. What makes this idea attractive and possibly feasible with current technology is the fact that it should be possible to fabricate high-Q stripline waveguide cavities on the superconducting surface of a microchip, which confine the microwave mode to a very small effective volume and to simultaneously trap a large ensemble of cold atoms very close to the surface. The combination of high-Q stripline waveguide cavities and atom-trapping technology surely will involve new challenges, but there seem to be no fundamental problems. As already demonstrated, such a cavity can be strongly coupled to on-chip Cooper-pair box qubits [3.6]. By combining the two systems, one thus could establish a connection between the atomic ensemble and solid-state qubits. This setup hence bridges an enormous range of time scales starting from the sub-microsecond scale of solid-state qubits, over the millisecond lifetime of microwave photons, to the atomic hyperfine coherence lifetime of seconds.

In the particular setup discussed here, the ensemble consists of a cloud of ultracold ^{87}Rb trapped in an on-chip magnetic wire trap and pumped to one of the trappable hyperfine levels, for example, $F = 1$, $m_F = -1$. The interaction between the atoms and the field is dominated by the magnetic dipole transitions between $|F = 1, m_F\rangle$ and $|F = 2, m_F'\rangle$. These transitions are widely used for hyperfine manipulations of cold atomic ensembles by externally injected microwaves [3.7]. We assume in the following that the experimental setup guarantees that the cavity is resonant with only one of the possible transitions ($\Delta m_f = m_F - m_F' = \pm 1$ with transition frequency $\omega_a/(2\pi) = 6.83$ GHz, corresponding to $T \approx 330$ mK), and hence allows for the atoms to be treated as two-level systems. Actually, in some cases it is more favorable to use Raman-type coupling employing an extra radio-wave field to choose a suitable microwave transition [3.8].

We ignore some of these technical details at this point and focus on the three main topics: After the introduction of the model in Sec. 3.2, we first investigate conditions for strong coupling between the ensemble and the cavity and the experimental consequences when one adds the obscuring effects of thermal photons due to a finite cavity temperature. In Secs. 3.6 and 3.7 we discuss the methods we use, whereas in Secs. 3.8– 3.11 we address several aspects of the resulting dynamics. Here the optically aligned ensemble, which has much lower effective temperature, can be expected to act as a heat sink for the cavity mode removing thermal photons. As the upper and lower hyperfine states have a virtually infinite lifetime compared with other system time scales, we can also completely invert the system, mimicking an effective negative temperature, and use it to pump energy into the system. As a prominent example, we study in Sec. 3.12 the superradiant decay of a fully inverted ensemble again with some thermal photons initially present. Finally, we exhibit in Sec. 3.13 the possibility of building an ultranarrow linewidth single-chip stripline micromaser operating directly on an atomic clock type transition, which is in close analogy to an optical-lattice-based setup, as recently suggested in [3.9].

3.2. Model

3.3. Collective atom-field Hamiltonian

A single atom, formally represented here by a two-level system resonantly coupled to a cavity mode, can be well described by the Jaynes-Cummings Hamiltonian. For N two-level systems trapped so close to each other in the cavity that they see the same field and thus are coupled to the mode with equal strength g, we then get the generalized Hamiltonian:

$$\mathrm{H} = \hbar\omega_m a^\dagger a + \frac{\hbar\omega_a}{2}\sum_j \sigma_j^z + \hbar g \sum_j \left(\sigma_j^+ a + a^\dagger \sigma_j^-\right) \; . \tag{3.3.1}$$

with a being the annihilation operator for a cavity photon, σ_j^+ being the excitation operator for the jth two-level system and $\left[\sigma_i^+, \sigma_j^-\right] = \sigma_i^z \delta_{ij}$. The frequency of the two-level systems and the mode are denoted by ω_a and ω_m, respectively. The coupling strength $g = \vec{B}\left(\vec{r}\right) \cdot \vec{\mu}/\hbar$ depends on the strength of the magnetic field per photon $\vec{B}$ at the position $\vec{r}$ of the atoms and the magnetic moment $\vec{\mu}$ of the considered transition.

What make an ensemble of atoms coupled to a cavity interesting are collective effects emerging from the common coupling of all atoms to the same mode. This can be well illustrated by introducing collective atomic operators $\mathrm{S}^\pm = \sum_j \sigma_j^\pm$ and $\mathrm{S}^z = \frac{1}{2}\sum_j \sigma_j^z$. The treatment in terms of collective operators provides a convenient basis for classifying the possible states of the ensemble and is therefore discussed here. As we see in Sec. 3.4, we have to resort to Hamiltonian (3.3.1) in our particular treatment. The introduction of $\mathrm{S}^{\pm}$ and S^{z} leads to the Tavis-Cummings form of this Hamiltonian:

$$\mathrm{H}_{\mathrm{TC}} = \hbar\omega_m a^{\dagger} a + \hbar\omega_a \, \mathrm{S}^{z} + \hbar g \left(\mathrm{S}^{+} a + a^{\dagger} \, \mathrm{S}^{-} \right) \tag{3.3.2}$$

where single photons are coupled to distributed (delocalized) excitations in the ensemble [3.1]. Let us shortly review some of its most known properties here. Mathematically, the collective operators follow the standard commutation relations for angular momentum operators $\boldsymbol{S} = (\mathrm{S}^{x}, \mathrm{S}^{y}, \mathrm{S}^{z})$, with $\mathrm{S}^{\pm} = (\mathrm{S}^{x} \pm \mathrm{i}\, \mathrm{S}^{y})$. The corresponding eigenstates of $\boldsymbol{S}^2$ and S^{z} are the so-called Dicke states $|J, M\rangle$, with $\boldsymbol{S}^2 |J, M\rangle = J(J+1) |J, M\rangle$ and $\mathrm{S}^{z} |J, M\rangle = M |J, M\rangle$, where $J = 0, 1, \ldots, N/2$ and $M = -J, \ldots, J$. Formally, a fully inverted ensemble corresponds to the maximum angular momentum of $J = N/2$ [3.10, 3.11] and projection $M = N/2$. Repeated application of the collective downward ladder operator S^{-} on the initial state $|J, J\rangle \mathrel{\widehat{=}} |e, e, \ldots, e\rangle$ gives the lowest state $|J, -J\rangle \mathrel{\widehat{=}} |g, g, \ldots, g\rangle$.

The states in between are generated according to

$$\mathrm{S}^{\pm} |J, M\rangle = \sqrt{(J \pm M + 1)\,(J \mp M)}\, |J, M \pm 1\rangle \ . \tag{3.3.3}$$

The interaction can then be conveniently rewritten in terms of normalized collective operators $\widetilde{\mathrm{S}}^{\pm} = \frac{1}{\sqrt{N}} \sum_i \sigma_i^{\pm}$ to obtain

$$\widetilde{\mathrm{H}} = \hbar\omega_m a^{\dagger} a + \hbar\omega_a \, \widetilde{\mathrm{S}}^{+} \, \widetilde{\mathrm{S}}^{-} + \hbar g_{\mathrm{eff}} \left(\widetilde{\mathrm{S}}^{+} a + a^{\dagger} \, \widetilde{\mathrm{S}}^{-} \right) \ , \tag{3.3.4}$$

with $g_{\mathrm{eff}} = g\sqrt{N}$. Note that in the case where the atoms in the ensemble couple to the cavity with different coupling constants g_i, we generalize to $\widetilde{\mathrm{S}}^{\pm} = \frac{1}{g_{\mathrm{eff}}} \sum_i g_i \sigma_i^{\pm}$, with $g_{\mathrm{eff}} = \sqrt{\sum_i g_i^2}$. This reduces to $g_{\mathrm{eff}} = g\sqrt{N}$ if all g_i are equal. To simplify matters, we remain with the case of equal coupling strength.

Allowing only one excitation in the system, we see that the ground state $|0\rangle_a \mathrel{\widehat{=}} |J, -J\rangle \mathrel{\widehat{=}} |g, g, \ldots, g\rangle$ is only coupled to the symmetric atomic excitation state $\widetilde{\mathrm{S}}^{+} |0\rangle_a = |1\rangle_a = |J, -J+1\rangle \mathrel{\widehat{=}} \frac{1}{\sqrt{N}} \left(|e, g, g, \ldots, g\rangle + |g, e, g, \ldots, g\rangle + \cdots + |g, \ldots, g, e\rangle \right)$, while other atomic states with only one excitation play no role. Hence, in this form we end up again with a two-level atomic system, where the dependence of the atom-cavity coupling on the number of atoms is explicitly visible. Even for transitions with a very small coupling constant g, strong coupling can be achieved for sufficiently large N.

Note that in Eq. (3.3.4) we use $\widetilde{\mathrm{S}}^z \approx -\frac{1}{2} + \frac{\widetilde{\mathrm{S}}^+\widetilde{\mathrm{S}}^-}{N}$, where $\widetilde{\mathrm{S}}^z = \frac{1}{2N}\sum_i \sigma_i^z$. This approximation is exactly valid only either for a single atom or the special case where we consider only one excitation in the system. The constant $-\frac{1}{2}$ is neglected in the Hamiltonian. In general, we find for a state with $J = \frac{N}{2}$ and $M = -J + s$

$$\langle J, -J+s|\, \widetilde{\mathrm{S}}^z \,|J, -J+s\rangle = -\frac{1}{2} + \frac{s}{2J} \tag{3.3.5}$$

and

$$\langle J, -J+s|\, \widetilde{\mathrm{S}}^+\,\widetilde{\mathrm{S}}^- \,|J, -J+s\rangle = s - \frac{s\,(s-1)}{2J}\ . \tag{3.3.6}$$

For $s \ll N$ we neglect the second term on the right-hand side of Eq. (3.3.6) and find the approximation for $\widetilde{\mathrm{S}}^z$, which becomes exact for $s = 1$.

For large ensembles with few excitations this approximation is closely related to the bosonization procedure. For $M \approx -J$ with $J = N/2$ and from

$$\begin{aligned}\left[\widetilde{\mathrm{S}}^+, \widetilde{\mathrm{S}}^-\right] &= \frac{1}{N}\left[\mathrm{S}^+, \mathrm{S}^-\right] \\ &= \frac{2\,\mathrm{S}^z}{N} = \left(-1 + \mathcal{O}\left(\frac{1}{N}\right)\right)\mathbb{1}\ ,\end{aligned} \tag{3.3.7}$$

we find that for few excitations it is possible to identify $\widetilde{\mathrm{S}}^+$ and $\widetilde{\mathrm{S}}^-$ with bosonic creation and annihilation operators. Hence, we end up with a system of coupled oscillators, for which a great deal of solution techniques exist.

Let us now come back to the atom-field interaction [Eq. (3.3.4)]. It is well known that the eigenstates are coherent superpositions of the two previously introduced basis states, where the excitation is located either in the mode or in the ensemble. Let $|0\rangle_m$ and $|1\rangle_m = a^\dagger\,|0\rangle_m$ be the possible states of the mode and $|0\rangle_a$ and $|1\rangle_a$ be the ensemble states. With $\omega_a = \omega_m$, the two eigenstates then read

$$|+\rangle = \frac{1}{\sqrt{2}}\left(|1\rangle_a\,|0\rangle_m + |0\rangle_a\,|1\rangle_m\right)\ , \tag{3.3.8}$$

$$|-\rangle = \frac{1}{\sqrt{2}}\left(|1\rangle_a\,|0\rangle_m - |0\rangle_a\,|1\rangle_m\right)\ , \tag{3.3.9}$$

and as expected are separated by the energy difference $2g_{\text{eff}}$. Of course, the system possesses more states containing essentially one excitation quantum, but those are not directly coupled to the ground state if we consider only collective operators. The collective operators couple states within one J manifold, like the previously discussed manifold with maximum angular momentum $J = N/2$ and $M = -J \dots J$. Taking into account the manifolds of states with $J < N/2$, one can see that in general there is a large number of states describing an ensemble with n excitations. In the forthcoming calculations including spontaneous emissions, such states with $J < N/2$ can be populated as well [3.12]. In addition, we also do not restrict the dynamics to a single excitation.

3.4. Master equation including decoherence and thermal noise

In any realistic implementation of the preceding model, coupling of the thermal environment to the field mode and the atoms is unavoidable. This generates several sources of noise and decoherence we have to address to be able to reliably describe the dynamics. Despite its high Q value, the microwave resonator still has a non-negligible finite linewidth $\kappa = 1/\tau$. In other words, a stored photon is likely to be lost from the cavity after the time τ. Similarly, atomic excitations are assumed to decay with a rate that is, fortunately, in our case negligibly small in practice [3.13]. However, we have to consider trap loss of atoms leaving the cavity mode, which generates an effectively faster decay of the atomic excitation, denoted by the rate γ_a. This can be to some extent controlled by a suitable choice of the trapping states and trap geometry. An additional and in general quite serious source of noise are thermal photons that leak into the cavity. For an unperturbed cavity mode they lead to an average occupation number of

$$\bar{n}(\omega_m, T) = \frac{\mathrm{e}^{-\frac{\hbar\omega_m}{k_B T}}}{1 - \mathrm{e}^{-\frac{\hbar\omega_m}{k_B T}}} , \tag{3.4.1}$$

where T denotes the temperature of the environment. In principle, such thermal photons are also present on the atomic transition and lead to a thermalization of the optically pumped atomic ensemble. Fortunately, the weak dipole moment of the atom renders this thermalization rate so slow that it can be ignored at the experimentally relevant time scales. In principle, even this rate could be collectively enhanced, but it largely addresses collective states only very weakly coupled to the cavity mode.

Putting all these noise sources together, we can use standard quantum optical methods to derive a corresponding master equation for the reduced atom-cavity density matrix [3.14]:

$$\frac{\mathrm{d}}{\mathrm{d}t}\rho = \frac{1}{\mathrm{i}\hbar}\left[H,\rho\right] + \mathcal{L}\left[\rho\right] \ , \tag{3.4.2}$$

with the Liouvillian

$$\begin{aligned}\mathcal{L}\left[\rho\right] =& \mathcal{L}_{\text{cavity}}\left[\rho\right] + \mathcal{L}_{\text{spont}}\left[\rho\right] \\ =& \kappa\left(\bar{n}+1\right)\left(2a\rho a^{\dagger} - a^{\dagger}a\rho - \rho a^{\dagger}a\right) \\ &+ \kappa\bar{n}\left(2a^{\dagger}\rho a - aa^{\dagger}\rho - \rho aa^{\dagger}\right) \\ &- \frac{\gamma_a}{2}\sum_{j=1}^{N}\left(\sigma_j^{+}\sigma_j^{-}\rho + \rho\sigma_j^{+}\sigma_j^{-} - 2\sigma_j^{-}\rho\sigma_j^{+}\right) \ .\end{aligned} \tag{3.4.3}$$

We assumed here that direct thermal excitations of the atoms can be neglected due to the weak coupling of the hyperfine transition to the environment. The only significant influx of thermal energy thus occurs via the cavity input-output couplers (mirrors). Note that the part of the Liouvillian describing spontaneous emission reflects the assumption that the atoms are coupled to N statistically independent reservoirs. The main reason for this treatment is that the decay rate γ_a summarizes the very small decay rate of atomic excitations and the loss rate of atoms from the trap. Since the loss of individual atoms from the trap is a noncollective process, the independent reservoirs assumption is advisable. This part of the Liouvillian cannot be written in terms of collective operators, and therefore it will not conserve J [3.15]. Therefore, states with $J < N/2$, including dark states, become accessible.

3.5. Signatures of strong coupling

A decisive first step toward applications of such system is the precise characterization and determination of their limits. In particular, the experimental confirmation of sufficiently strong atom-field coupling compared to the inherent decoherence processes is of vital importance. This has to be seen in connection with extra limitations induced by thermal photons in the mode, which in contrast to optical setups play an important role in the microwave domain. We thus need reliable methods to determine the atom number, their effective coupling strength, and noise properties. In particular, we want to find the minimum temperature requirements that would make it possible to observe strong coupling.

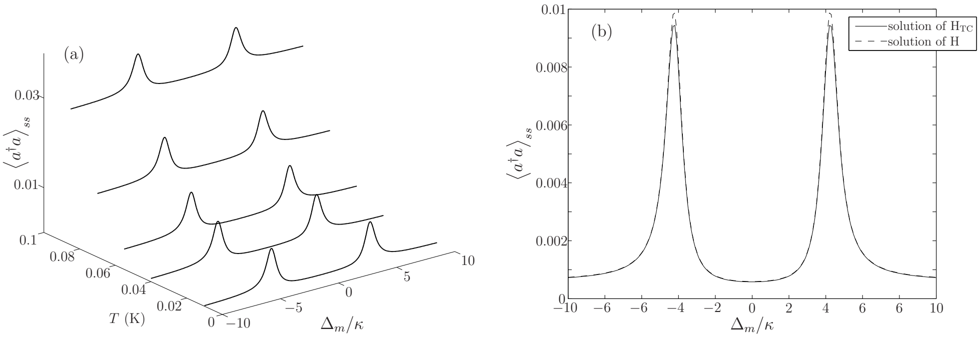

Figure 3.1.: (a) Steady-state number of photons $\left\langle a^\dagger a \right\rangle_{ss}$ in the pumped cavity for different detunings $\Delta_m = \omega_m - \omega_l$ and different temperatures, obtained from Hamiltonian $\mathrm{H_{TC}}$. The parameters chosen were $\kappa = 1$, $N = 2$, $g = 3$, $\gamma_a = 0.05$, $\eta = 0.1$. With increasing temperature the two peaks indicating strong coupling are superimposed by thermal photons. To compare the dynamics of $\mathrm{H_{TC}}$ and H, we plot both results for $T = 0.04$ K ($\bar{n} = 3 \times 10^{-4}$) in (b).

3.6. Numerical solution for small particle number

To get some first qualitative understanding of finite T effects, we study the coupled atom-field dynamics in the regime of strong coupling under the influence of thermal photons based on the direct numerical solution of the master equation. Of course, here we have to resort to the limit of only a few atoms with increased coupling per particle. Nevertheless, at least the qualitative influence of thermal photons will become visible. For the practical implementation, we rely on the quantum optics toolbox for Matlab to explicitly calculate the dynamics of the density matrix [3.16], which allows straightforward implementation of the Hamiltonian in Eq. (3.3.2) formulated in terms of the collective operators.

The cavity is pumped by a coherent microwave field with frequency ω_l and strength η, which in the frame rotating with ω_l is represented in the Hamiltonian by the additional term $\mathrm{H}_p = \mathrm{i}\hbar \left(\eta a^\dagger - \eta^* a \right)$. From the stationary solution, we then determine the steady-state photon number in the cavity for different frequencies of the pump field to determine the central system resonances, where the pump frequency matches the eigenfrequencies $\omega_m \pm g_{\mathrm{eff}}$ of the coupled ensemble-cavity system. At zero temperature and weak pumping, we get the well-known vacuum Rabi splitting showing two distinct resonances separated by $2g_{\mathrm{eff}}$. With increasing temperature and number of thermal photons, these two peaks will get increasingly broadened and reside on a broad background. Figure 3.1(a) illustrates the effect.

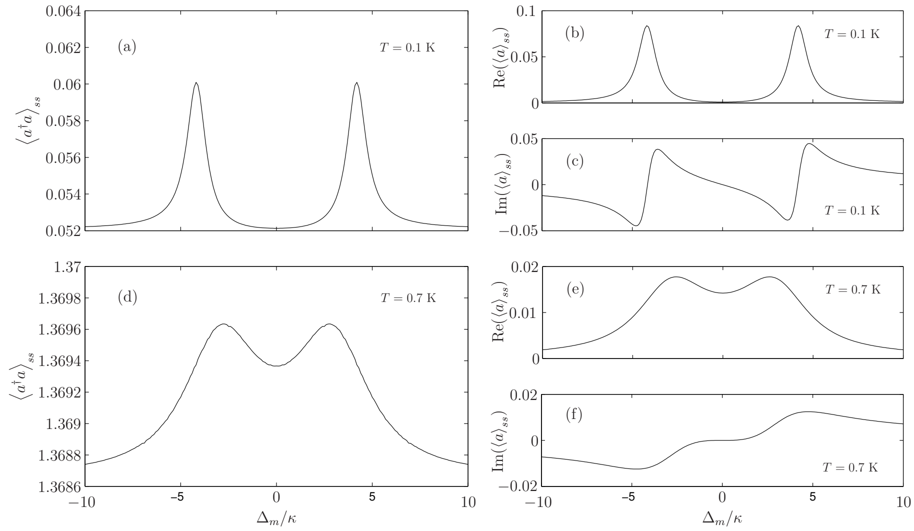

Figure 3.2.: Effects of higher temperatures: For $T = 0.1$ K, (a) shows the steady-state number of photons, whereas (b) and (c) show the real and imaginary part of the steady state field in the cavity. The peaks in the photon number start to broaden and finally vanish. The amplitude of the field shows similar behavior. Panels (d), (e), and (f) show the same quantities for $T = 0.7$ K. The remaining parameters were chosen as in Fig. 3.1.

To compare the dynamics obtained from the restricted Tavis-Cummings Hamiltonian H_{TC} in Eq. (3.3.2) with the dynamics of Hamiltonian H in Eq. (3.3.1), we compare the results for both cases in Fig. 3.1(b). Even for the rather small atom numbers chosen here, the difference and thus the influence of the nonsymmetric states is hardly visible in this observable.

The peaks in the photon number in principle stay visible also for higher temperatures, but they start to broaden and finally vanish. Regardless, the detection on the thermal background gets technically more challenging. The intracavity steady-state amplitude of the field shows a similar behavior and a determination of the splitting becomes increasingly impossible, despite the fact that phase-sensitive detection (homodyne) can help. An example is shown in Fig. 3.2. This effect is expected to be less important if the ensemble contains a large number of atoms. However, this regime is not accessible for direct numerical simulations and we have to develop alternative semianalytic approaches.

3.7. Truncated cumulant expansion of collective observables

To overcome the system size restrictions of a direct numerical solution, we now turn to an alternative approach that does not rely on the simulation of the dynamics of the whole density matrix. Instead, we derive a system of coupled differential equations for the expectation values of the relevant system variables. The inversion of atom i then obeys

$$\begin{aligned}\frac{\mathrm{d}}{\mathrm{d}t}\left\langle\sigma_i^z\right\rangle &= \mathrm{Tr}\{\sigma_i^z\frac{\mathrm{d}}{\mathrm{d}t}\rho\}\\ &= -\mathrm{i}2g\left(\left\langle\sigma_i^+ a\right\rangle - \left\langle\sigma_i^- a^\dagger\right\rangle\right) - \gamma_a\left(\left\langle\sigma_i^z\right\rangle + 1\right)\end{aligned}\tag{3.7.1}$$

which couples to $\left\langle\sigma_i^+ a\right\rangle$ and $\left\langle\sigma_i^- a^\dagger\right\rangle = \left\langle\sigma_i^+ a\right\rangle^*$. We assume that all atoms are equal, which allows us to replace $\left\langle\sigma_i^z\right\rangle$ with $\left\langle\sigma_1^z\right\rangle$. Expectation values for pairs of different atoms like $\left\langle\sigma_i^+\sigma_j^-\right\rangle$ can be replaced with $\left\langle\sigma_1^+\sigma_2^-\right\rangle$.

While these equations are exact in principle, the procedure ultimately leads to an infinite set of coupled equations. We thus have to start approximations and truncate this set at a chosen point, neglecting higher-order cumulants [3.9, 3.17]. The truncation has to be carefully chosen and tested in general. Here we stop at third order, which in similar situations has proven to be well suited to describe the essential correlations [3.9].

The expansion for an expectation value of the form $\langle ab\rangle$ is the well-known relation $\langle ab\rangle = \langle ab\rangle_c + \langle a\rangle\langle b\rangle$, with $\langle ab\rangle_c$ being the covariance between a and b. Along this line, one expands third-order terms in the form

$$\begin{aligned}\langle abc\rangle \quad = \quad &\underbrace{\langle abc\rangle_c}_{\text{neglected}} + \langle ab\rangle_c\langle c\rangle + \langle ac\rangle_c\langle b\rangle\\ &+ \langle bc\rangle_c\langle a\rangle + \langle a\rangle\langle b\rangle\langle c\rangle \ .\end{aligned}\tag{3.7.2}$$

We make one exception in this expansion when it comes to the quantity $\left\langle a^\dagger a\sigma_1^z\right\rangle$; the reason for this is discussed in Appendix 3.17.

The number of equations depends on the order of the cumulants we wish to keep track of. Furthermore, the problem is greatly simplified if there is no coherent input field driving our cavity. In this case, no defined phase exists in our system, so we can assume that $\langle a\rangle = \left\langle a^\dagger\right\rangle = \left\langle\sigma_1^\pm\right\rangle = 0$. Note that while for a single system trajectory

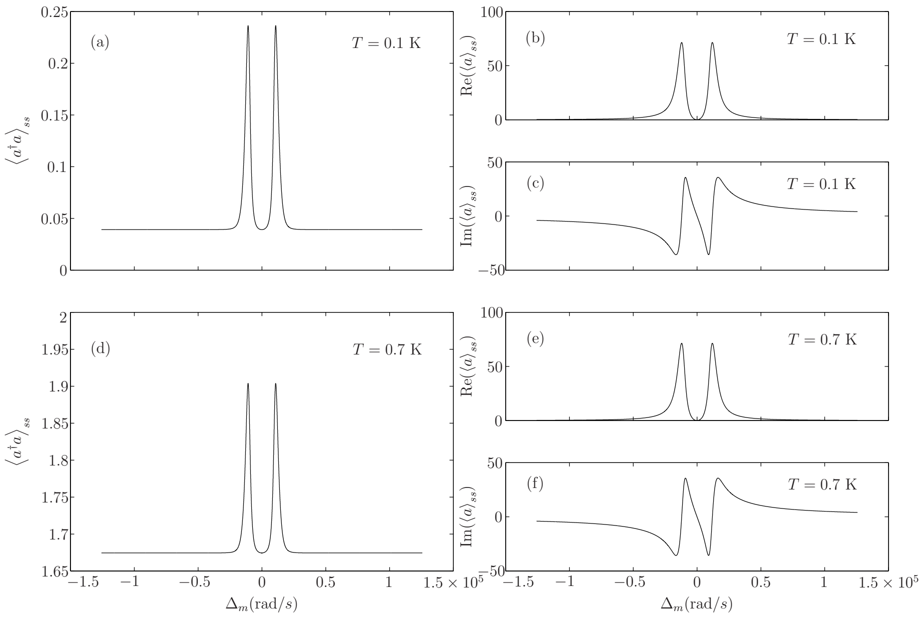

Figure 3.3.: The steady-state field and photon number in the cavity for different frequencies of the pump. The size of the ensemble was chosen to be $N = 10^5$ and we set $\kappa = 7 \times 10^3$, $\eta = 5 \times 10^5$, $\gamma_a = 0.3$ and $g = 40$. Panel (a) shows the steady-state number of photons, whereas (b) and (c) show the real and imaginary parts of the steady-state field in the cavity for $T = 0.1$ K, which corresponds to $\bar{n} = 0.04$. The remaining figures show the same quantities for $T = 0.7$ K, corresponding to $\bar{n} = 1.67$. The results show that for a sufficiently large number of atoms strong coupling remains observable despite of the presence of thermal photons.

a coherent field can build up as in a laser, for an average over many realizations the preceding assumption holds. For a covariance like $\left\langle \sigma_1^+ a \right\rangle_c = \left\langle \sigma_1^+ a \right\rangle - \left\langle \sigma_1^+ \right\rangle \langle a \rangle$, we therefore find $\left\langle \sigma_1^+ a \right\rangle = \left\langle \sigma_1^+ a \right\rangle_c$. The four remaining equations are

$$\frac{\mathrm{d}}{\mathrm{d}t} \langle \sigma_1^z \rangle = -\,\mathrm{i}2g \left(\left\langle \sigma_1^+ a \right\rangle - \left\langle \sigma_1^- a^\dagger \right\rangle \right) - \gamma_a \left(\langle \sigma_1^z \rangle + 1 \right) \ , \tag{3.7.3}$$

$$\frac{\mathrm{d}}{\mathrm{d}t} \left\langle a^\dagger a \right\rangle = -\,\mathrm{i}gN \left(\left\langle a^\dagger \sigma_1^- \right\rangle - \left\langle a \sigma_1^+ \right\rangle \right) - 2\kappa \left\langle a^\dagger a \right\rangle + 2\kappa\bar{n} \ , \tag{3.7.4}$$

$$\begin{aligned}\frac{\mathrm{d}}{\mathrm{d}t}\left\langle a\sigma_1^+\right\rangle =& -\left(\kappa+\frac{\gamma_a}{2}+\mathrm{i}\left(\omega_m-\omega_a\right)\right)\left\langle a\sigma_1^+\right\rangle \\ & -\mathrm{i}g\left(\frac{\langle\sigma_1^z\rangle+1}{2}+\left\langle a^\dagger a\right\rangle\langle\sigma_1^z\rangle+(N-1)\left\langle\sigma_1^+\sigma_2^-\right\rangle\right)\ , \end{aligned} \tag{3.7.5}$$

and

$$\frac{\mathrm{d}}{\mathrm{d}t}\left\langle\sigma_1^+\sigma_2^-\right\rangle = -\gamma_a\left\langle\sigma_1^+\sigma_2^-\right\rangle - \mathrm{i}g\,\langle\sigma_1^z\rangle\left(\left\langle\sigma_1^- a^\dagger\right\rangle-\left\langle\sigma_1^+ a\right\rangle\right)\ . \tag{3.7.6}$$

To inject energy into our system without losing the property of having no defined phase, we can introduce an incoherent pump of the atoms. In essence, this gives an additional term in the Liouvillian very much resembling spontaneous emission in opposite direction. Formally, it reads $-\frac{w}{2}\sum_{j=1}^{N}\left(\sigma_j^-\sigma_j^+\rho+\rho\sigma_j^-\sigma_j^+-2\sigma_j^+\rho\sigma_j^-\right)$, where w denotes the rate of the pump. The modifications of Eqs. (3.7.3)–(3.7.6) narrow down to the replacement of γ_a with γ_a+w and of $-\gamma_a\left(\langle\sigma_1^z\rangle+1\right)$ with $-\left(\gamma_a+w\right)\left(\langle\sigma_1^z\rangle+\frac{w-\gamma_a}{w+\gamma_a}\right)$ in Eq. (3.7.3).

Introducing a coherent pump leads to a larger set of 13 coupled equations for the quantities $\langle a\rangle$, $\langle\sigma_1^z\rangle$, $\left\langle\sigma_1^+\right\rangle$, $\left\langle a\sigma_1^+\right\rangle_c$, $\langle a\sigma_1^z\rangle_c$, $\left\langle\sigma_1^+\sigma_2^-\right\rangle_c$, $\left\langle a^\dagger a\right\rangle_c$, $\left\langle a\sigma_1^-\right\rangle_c$, $\left\langle a^\dagger a^\dagger\right\rangle_c$, $\left\langle\sigma_1^-\sigma_2^-\right\rangle_c$, $\left\langle\sigma_1^z\sigma_2^+\right\rangle_c$, $\langle\sigma_1^z\sigma_2^z\rangle_c$ and $\left\langle a^\dagger a\sigma_1^z\right\rangle$; for details, see Appendix 3.16. In this case we transform into a rotating frame with respect to the frequency of the pump ω_l. This results in $\Delta_m=\omega_m-\omega_l$ for the detuning of the cavity and $\Delta_a=\omega_a-\omega_l$ for the detuning of the atoms with respect to the pump frequency.

In general, the set of equations is too complex for a direct analytical solution and has to be integrated numerically. In this way we obtain the steady-state expectation values of relevant observables as the occupation number of the cavity $\left\langle a^\dagger a\right\rangle$ or the inversion of the ensemble $\langle\sigma_1^z\rangle$.

To compare the results of the obtained equations with the results in Sec. 3.6, we plot the steady-state number of photons and the field in the cavity for different frequencies of the pump laser in Fig. 3.3. We clearly see that effective strong coupling appears for a sufficiently large number of weakly coupled atoms and can stay visible also at higher temperatures. Further discussion is given in Sec. 3.10. In Fig. 3.4 we schematically depict the setup including the described loss and pump processes.

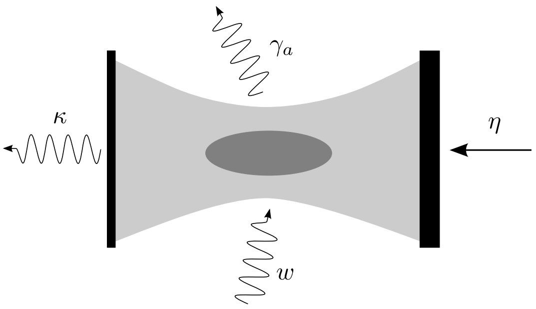

Figure 3.4.: To simplify matters, we depict the cavity as a Fabry-Perot cavity which can be pumped through a mirror with high reflectivity. The observation of the dynamics is carried out using the second mirror, which has a lower reflectivity. Additionally, we can pump the ensemble incoherently from the side.

3.8. Cavity output spectrum at finite temperature

Naturally, the total field intensity in the cavity is only part of the story and significant physical information can be obtained from a spectral analysis of the transmitted field. Using the quantum regression theorem, the spectrum of the light transmitted through one of the mirrors can be expressed in terms of the Fourier transform of the corresponding autocorrelation function of the field amplitude.

At finite T this is not the full story, and to obtain the actual spectrum of the light impinging on the detector, one has to include the thermal photons in the output mode reflected from the cavity. Hence, the normalized first-order correlation function of the field outside the cavity will have additional contributions from the correlation function of the thermal field, as well as of the correlation between the thermal field and the cavity field [3.18]. The latter is causing interference effects between cavity field and the thermal field. The correlations between reservoir operators and cavity operators can be expressed in terms of averages involving cavity operators alone [3.15, 3.18]. For a cavity radiating into a thermal reservoir, we find for the normalized first-order correlation function

$$
\begin{aligned}
g\left(\tau\right) =& \frac{1}{\mathcal{N}}\left\{\frac{1}{2\pi g\left(\omega\right)}\left\langle r_f^{\dagger}\left(0\right) r_f\left(\tau\right)\right\rangle + 2\kappa\left[\lim_{t\to\infty}\left\langle a^{\dagger}\left(t\right) a\left(t+\tau\right)\right\rangle\right]\right. \\
&\left. +2\kappa\bar{n}\left(\omega_m, T\right)\left[\lim_{t\to\infty}\left\langle\left[a^{\dagger}\left(t\right), a\left(t+\tau\right)\right]\right\rangle\right]\right\} , \qquad (3.8.1)
\end{aligned}
$$

with

$$
\mathcal{N} = \frac{1}{2\pi g\left(\omega\right)}\left\langle r_f^{\dagger} r_f\right\rangle + 2\kappa\left(\left\langle a^{\dagger} a\right\rangle_{\mathrm{ss}} - \bar{n}\left(\omega_m, T\right)\right) . \qquad (3.8.2)
$$

Here, r_f denotes the annihilation operator of a reservoir photon and $g\left(\omega\right)$ denotes the density of states in the reservoir. Equations for the correlation functions in Eq. (3.8.1) can be obtained via the quantum regression theorem. The resulting system of coupled equations is Laplace transformed to give the contributions to the spectrum that arise from the reservoir, the cavity and cavity-reservoir interference. The initial conditions necessary for the Laplace transform are the steady-state values obtained either numerically for the coherently pumped cavity or analytically (see Sec. 3.13).

We show the spectrum of the cavity without any pump, coherent or incoherent, but with $T = 0.1$ K in Fig. 3.5. The spectrum shows absorption dips at the frequencies of the coupled ensemble-cavity system. Some thermal photons that leak into the cavity are absorbed and lost into modes other than the cavity mode. In this form the thermal field is a broadband probe of resonant system absorption.

3.9. Cooling the field mode with the atomic ensemble

The spectra depicted in Fig. 3.5 show a weak loss of thermal photons from the coupled ensemble-cavity system. Cavity photons are absorbed and sometimes scattered into a mode other than the cavity mode. As the ensemble can be nearly perfectly optically pumped into a particular state, its effective temperature is close to zero and hence well below the mode temperature. A relative purity of the ensemble of 10^{-5} corresponds to $T \sim 28$ mK, where we used $\hbar\omega_a/k_bT = \ln\left(10^{-5}\right)$ with $\omega_a/2\pi = 6.83$ GHz. This leads to the question as to what extent the thermal occupation of the mode can be reduced by thermal contact between the two systems

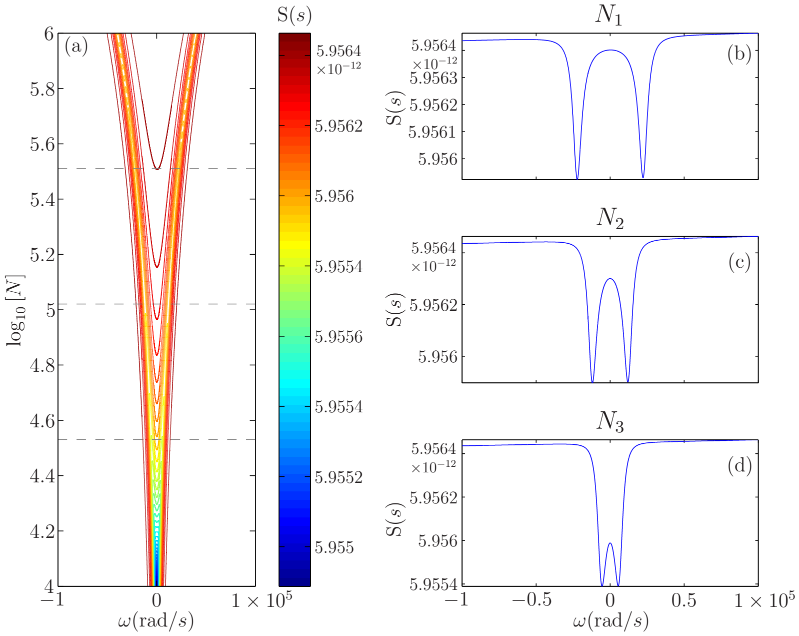

Figure 3.5.: (Color online) Overview of the transmitted spectrum S for different sizes of the ensemble (a). The temperature of the cavity is set to $T = 0.1$ K ($\bar{n} = 0.04$). The remaining parameters were chosen to be $\kappa = 7 \times 10^3$, $\gamma_a = 0.3$, $g = 40$, $\omega_a = \omega_m = 2\pi \times 6.83$ GHz. The dips in the spectrum indicate that thermal photons are absorbed by the ensemble and re-emitted into modes other than the cavity mode. The increasing distance between the absorption dips reflects the increasing number of atoms. In panels (b)-(d) we depict the spectra at $N_1 = 3.2 \times 10^5$, $N_2 = 1 \times 10^5$, and $N_3 = 3.4 \times 10^4$, indicated in (a) by the dashed horizontal lines.

via such energy transfer and loss. In Fig. 3.6(a) we show the dynamics of the photon number in the mode at different temperatures after putting the systems into contact. In Fig. 3.6(b) we consider different loss or decay rates γ_a of the excited atoms. In practice one could think of coupling to an magnetically untrapped atomic state or adding some repumping mechanism to increase this intrinsically very low rate. The dynamics is found numerically by integrating Eqs. (3.7.3)–(3.7.6). To see the effect for increasing temperature in Fig. 3.6(a), we initialize the ensemble with all atoms in the ground state, whereas the mode contains $\bar{n}\,(\omega_m, T)$ photons. The decay rate of the atoms is chosen to be $\gamma_a = 5 \times 10^4$. With increasing temperature the initial number of photons also increases. Due to coherent transfer and decay via the atoms, a constant fraction of the photons is removed from the cavity mode. In Fig. 3.6 (b) we show the same effect except that we now keep the temperature fixed to $T = 4$ K and vary the decay of the atoms $\gamma_a = 1 \times 10^3 \ldots 2 \times 10^5$. The steady state of the photon number strongly depends on γ_a. The red curve (with diamond markers) is

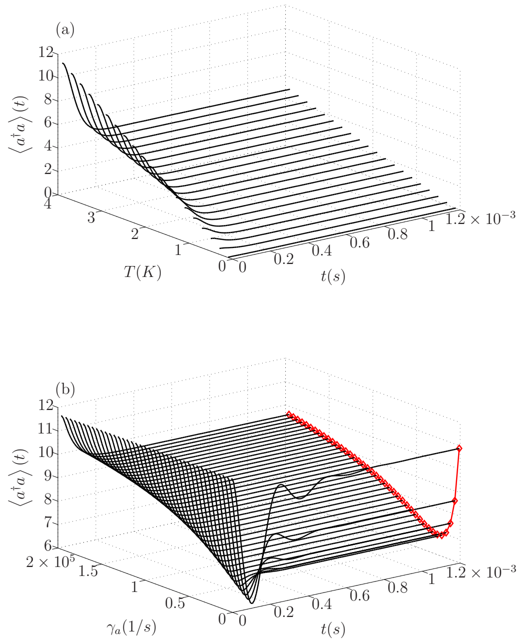

Figure 3.6.: (Color online) Loss of photons from the cavity mode. (a) Dynamics of the occupation of the mode for different temperatures and $\gamma_a = 5 \times 10^4$. A constant fraction of the photons is removed from the cavity mode. (b) For fixed $T = 4$ K ($\bar{n} = 11.7$), the loss rate of the atoms is varied between $\gamma_a = 1 \times 10^3$ and 2×10^5. The steady-state number of photons shows that there is an optimal loss rate. The red curve (with diamond markers) corresponds to the expected number of photons according to Eq. (3.9.1). The remaining parameters were chosen to be $\kappa = 7 \times 10^3$, $g = 40$, $\omega_a = \omega_m = 2\pi \times 6.83$ GHz, $N = 10^5$.

the expected number of photons remaining in the cavity

$$\left\langle a^\dagger a \right\rangle_{ss} = \bar{n}\left(\omega_m, T\right) - \frac{1}{2\kappa} N \gamma_a \left(\frac{1 + \langle \sigma_1^z \rangle_{\mathrm{ss}}}{2} \right) \tag{3.9.1}$$

which coincides with the numerical results. The inversion $\langle \sigma_1^z \rangle_{\mathrm{ss}}$ can be calculated analytically from Eqs. (3.7.3)–(3.7.6). The loss of thermal photons is proportional to the loss rate γ_a and the number of atoms in the excited state $N\left(\frac{1+\langle \sigma_1^z \rangle_{\mathrm{ss}}}{2}\right)$. The latter becomes very small if γ_a becomes large. Hence there is an optimal loss rate for each set of parameters.

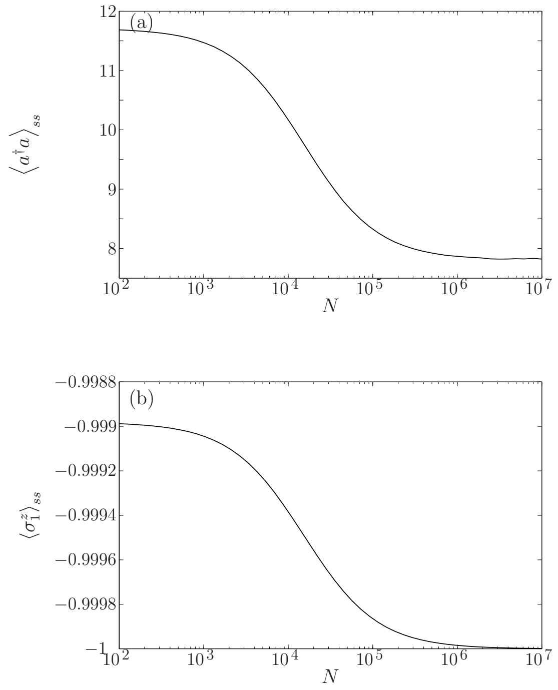

Figure 3.7.: Steady state of the photon number (a) and the inversion (b) for a loss rate $\gamma_a = \kappa = 7 \times 10^3$. Increasing the number of atoms N leads to a more effective removal of thermal photons. The remaining parameters are chosen to be $g = 40$, $\omega_a = \omega_m = 2\pi \times 6.83$ GHz, $T = 4$ K ($\bar{n} = 11.7$).

The removal of thermal photons becomes more effective if the number of atoms is increased. Meanwhile, the inversion of the ensemble also drops since the fraction of excited atoms is decreased. Overall, the effect is clearly visible (see Fig. 3.7), but it seems that for the actual parameters here its practical value remains limited. However, with a larger atom number and more tailored decay rates the method could be employed to reset a particular mode shortly before starting any quantum gate operation. Note that this treatment of the cooling process is limited to short time scales since the permanent loss of excitations via γ_a involves the loss of atoms from the ensemble. The number of lost atoms after the time t, approximated by the number of thermal photons that entered the cavity $t\kappa\bar{n}$, has to be much smaller than the ensemble size N, which restricts the time t.

In the situation where the mode is at $T \approx 0$ K and the atoms are subject to in-

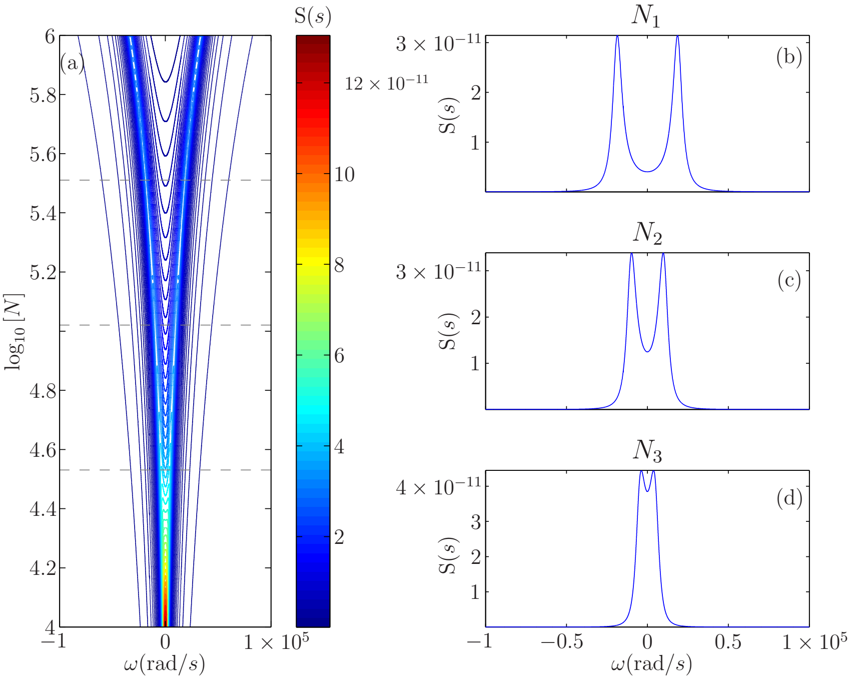

Figure 3.8.: (Color online) The temperature of the cavity is now set to $T = 0.001$ K ($\bar{n} = 0$) and an incoherent pump of the atoms with $w = 0.05$ is switched on. The spectrum now shows increased emission at the frequencies of the coupled system. Again figures (b)-(d) depict the spectra at $N_1 = 3.2 \times 10^5$, $N_2 = 1 \times 10^5$, and $N_3 = 3.4 \times 10^4$, indicated in (a) by the dashed horizontal lines.

coherent pumping we find increased transmission for the resonance frequencies (see Fig. 3.8). We again recover the $\sqrt{N}$ dependence of the splitting of the peaks.

3.10. Coherently driven cavity mode

An experimentally readily accessible quantity is the cavity field amplitude, which can be deduced by phase-sensitive (homodyne) detection of the output. This quantity is much less obscured by random thermal field fluctuations than the spectral intensity in total. As a phase reference, we therefore now introduce a coherent phase stable pump of the cavity, which is again represented in the Hamiltonian by the additional term $\mathrm{H}_p = \mathrm{i}\hbar\left(\eta a^\dagger - \eta^* a\right)$.

As mentioned previously, a coherent pump strongly increases the number of nonvan-

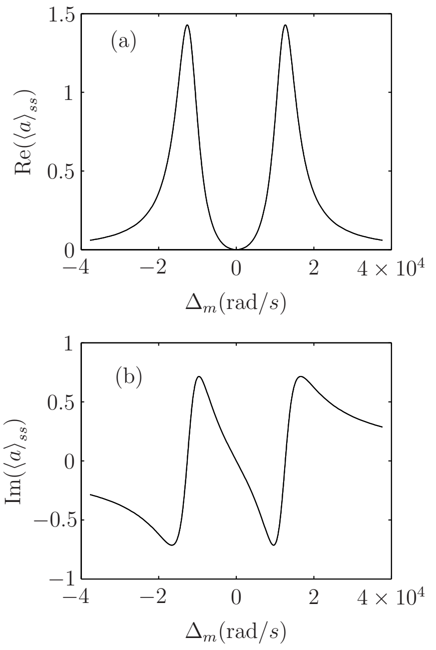

Figure 3.9.: Steady state field in the driven cavity, real part (a) and imaginary part (b). The size of the ensemble is chosen to be $N = 10^5$. The lines for $T = 0.01$ K ($\bar{n} = 0$) and $T = 10$ K ($\bar{n} = 30$) coincide.

ishing cumulants and at our level of truncation leads to a set of 13 coupled equations, which can be found in Appendix 3.16. Based on this set, we can calculate the stationary real- and imaginary part of the field in the cavity after transient dynamics. The amplitude of the field inside the cavity becomes maximal if the frequency ω_l of the driving laser hits one of the resonances of the coupled system. As we give a phase reference now the effect of a higher temperature on the field in the cavity is barely visible, in particular if we chose a large ensemble of $N = 10^5$ atoms (see Fig. 3.9).

Note that although not giving the vacuum Rabi splitting, the average atom-field coupling can be still deduced from these resonances as g enters in their frequency. If we go back to a rather small ensemble of $N = 10^2$ atoms, the influence of the temperature becomes visible. To ensure that we still can observe well split levels, which are not covered by the linewidth of the cavity, we increase the coupling constant g in our simulation. The results in Fig. 3.10 show that thermal effects become visible in the field only if the number of thermal photons is not negligible compared to N.

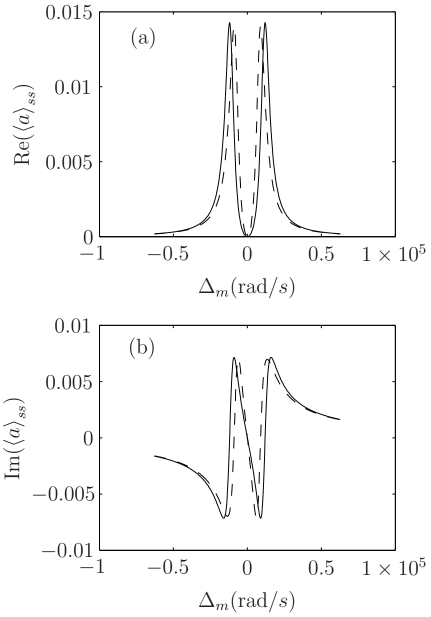

Figure 3.10.: Steady state field in the driven cavity, real part (a) and imaginary part (b), for $T = 0.01$ K ($\bar{n} = 0$) (solid lines) and $T = 10$ K ($\bar{n} = 30$) (dashed lines). For the small ensemble with $N = 10^2$ atoms we recover the effects of the thermal photons. To compensate for the lower number of atoms, the coupling is chosen to $g = 1200$. Otherwise, the splitting would be covered by the cavity linewidth.

3.11. Spectrum of the coherently driven cavity

The spectral intensity distribution of the coherently pumped cavity is calculated in a way similar to that described in Sec. 3.8. In contrast to the incoherent pump process that excites atoms in a noncollective way, as can be seen from the Liouvillian, the interaction with the coherently pumped mode is a collective interaction. To demonstrate this behavior, we calculate the spectral distribution of the mode intensity, without caring about the reservoir it radiates into, and the spectrum of the fluorescence of the atoms.

The cavity mode and the atomic transition are assumed to be on resonance with $\omega_a = \omega_m = 2\pi \times 6.83$ GHz, which is also the frequency of the pump laser. To calculate the incoherent part of the spectra we need the Fourier transform of the two-time correlation functions

$$\lim_{t\to\infty} \left\langle a^{\dagger}\left(t\right) a\left(t+\tau\right)\right\rangle_{c} = \lim_{t\to\infty} \left(\left\langle a^{\dagger}\left(t\right) a\left(t+\tau\right)\right\rangle - \left\langle a^{\dagger}(t)\right\rangle \left\langle a\left(t+\tau\right)\right\rangle\right) \qquad (3.11.1)$$

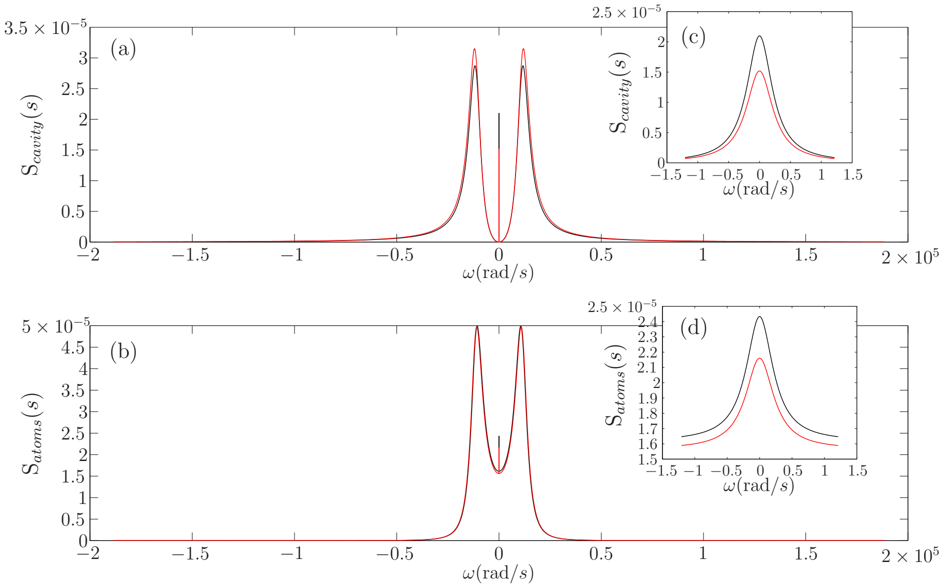

Figure 3.11.: (Color online) Incoherent spectrum of the mode (a) and of the fluorescence of the ensemble (b) for $T = 0.025$ K, $\kappa = 7 \times 10^3$, $\gamma = 0.3$, $N = 10^5$, $\eta = 9 \times 10^5$ in red (gray) and $\eta = 10^6$ in black. The pump driving the system is on resonance with the cavity and the ensemble. Insets (c) and (d) show a magnification of the central peak of each spectrum. The lower red (gray) line represents the result for $\eta = 9 \times 10^5$.

and

$$\lim_{t\to\infty} \left\langle \sigma_i^+ (t)\, \sigma_j^- (t+\tau) \right\rangle_c = \lim_{t\to\infty} \left(\left\langle \sigma_i^+ (t)\, \sigma_j^- (t+\tau) \right\rangle - \left\langle \sigma_i^+ (t) \right\rangle \left\langle \sigma_j^- (t+\tau) \right\rangle \right) . \tag{3.11.2}$$

The quantum regression theorem and Eqs. (3.16.1) to (3.16.5) give

$$\frac{\mathrm{d}}{\mathrm{d}\tau} \left\langle a^\dagger (0)\, a(\tau) \right\rangle_c = -\left(\kappa + \mathrm{i}\Delta_m\right) \left\langle a^\dagger (0)\, a(\tau) \right\rangle_c - \mathrm{i} g N \left\langle a^\dagger (0)\, \sigma_i^- (\tau) \right\rangle_c \tag{3.11.3}$$

and

$$\begin{aligned}\frac{\mathrm{d}}{\mathrm{d}\tau}\left\langle \sigma_i^+(0)\,\sigma_j^-(\tau)\right\rangle_c = &-\left(\frac{\gamma_a}{2}+\mathrm{i}\Delta_a\right)\left\langle \sigma_i^+(0)\,\sigma_j^-(\tau)\right\rangle_c \\ &+\mathrm{i}g\left(\langle a(\tau)\rangle\left\langle \sigma_i^+(0)\,\sigma_j^z(\tau)\right\rangle_c+\langle\sigma_i^z(\tau)\rangle\left\langle \sigma_i^+(0)\,a(\tau)\right\rangle_c\right)\end{aligned} \tag{3.11.4}$$

where we use

$$\lim_{t\to\infty}\left\langle a^\dagger(t)\,a(t+\tau)\right\rangle_c \equiv \left\langle a^\dagger(0)\,a(\tau)\right\rangle_c$$

and

$$\lim_{t\to\infty}\left\langle \sigma_i^+(t)\,\sigma_j^-(t+\tau)\right\rangle_c \equiv \left\langle \sigma_i^+(0)\,\sigma_j^-(\tau)\right\rangle_c \ .$$

Equations (3.11.3) and (3.11.4) couple to four other two-time correlation functions that have to be calculated. To solve for the desired quantities, we Laplace transform both sets of equations and use Cramer's rule to obtain $\langle a^\dagger(0)\,a(\tau)\rangle_c(s)$ and $\left\langle \sigma_i^+(0)\,\sigma_j^-(\tau)\right\rangle_c(s)$. The necessary steady-state values are obtained numerically.

The incoherent spectra of the mode and of the atoms both show a narrow peak at $\omega_a=\omega_m$ which has a width of $\approx 2\gamma_a$ (see Fig. 3.11). The double-peaked structure is a remainder of thermal excitations acting as a broad band probe for the ensemble-cavity system. With increasing strength of the coherent pump the narrow central peak becomes dominant. The appearance of the central peak is probably related to weak contributions from almost-dark states (very weakly coupled to the mode). Let us mention in this context that the atomic ensemble is not restricted to a manifold of the Dicke states with fixed J since we include spontaneous emission in our model. It is hence possible that the ensemble ends up in a dark state, where it does not couple to the cavity mode. The time-constant that determines the decay into and the decay of such a dark state is of the order $1/\gamma_a$. This allows for the buildup of long time coherences, and the times the ensemble is in a dark state significantly change the statistics of the photon emission. The result is then a narrow peak in the incoherent spectrum [3.19, 3.20], where the width of the peak is determined by the characteristic time the ensemble resides in a bright or dark state, in our case γ_a. In the case of an incoherently pumped ensemble, the narrow peak does not arise. A reason for this can be the nature of the incoherent pump which is noncollective and hence able to pump the ensemble out of a dark state in a shorter time. This is not possible in the case of the coherently pumped cavity: Spontaneous emission brings the ensemble to a dark state, but the collective interaction with the mode cannot reach it there.

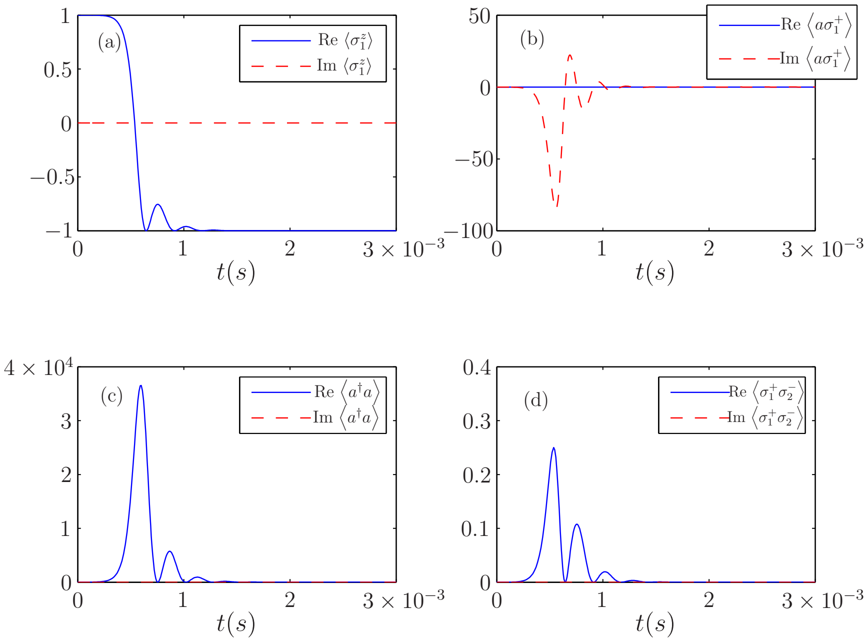

Figure 3.12.: (Color online) Dynamics of superradiant emission: numerical solutions of the dynamical equations for an ensemble of $N = 10^5$ atoms. The rapid drop of the inversion $\langle\sigma_1^z\rangle$ during the emission can be seen in (a). The exchange of excitations between the ensemble and the cavity is characterized by $\left\langle a\sigma_1^+\right\rangle$ in (b). Negative imaginary part of $\left\langle a\sigma_1^+\right\rangle$ indicates emission from the ensemble into the cavity, where a positive imaginary part indicates absorption of cavity photons by the ensemble. In (c) the number of photons in the cavity is depicted. Panel (d) shows the spin-spin correlation $\left\langle\sigma_1^+\sigma_2^-\right\rangle$. In this example the temperature of the mode was chosen to be $T = 4$ K.

3.12. Superradiance

A great advantage of the considered setup is that one has full control of the atomic state. Hence, instead of starting at a zero-temperature ground state we can prepare an almost fully inverted ensemble, which can feed energy into the system and corresponds to an effective negative temperature [3.21]. Since we have no initial phase bias in the system, Eqs. (3.7.3)–(3.7.6) are suitable for describing the dynamics. The resulting superradiant dynamics for an initially fully inverted ensemble is depicted in Fig. 3.12. In free space the emission occurs in a characteristic burst of duration $\approx \frac{1}{\gamma_a N}$ [3.22]. The presence of the cavity causes a partial reabsorption of the emitted

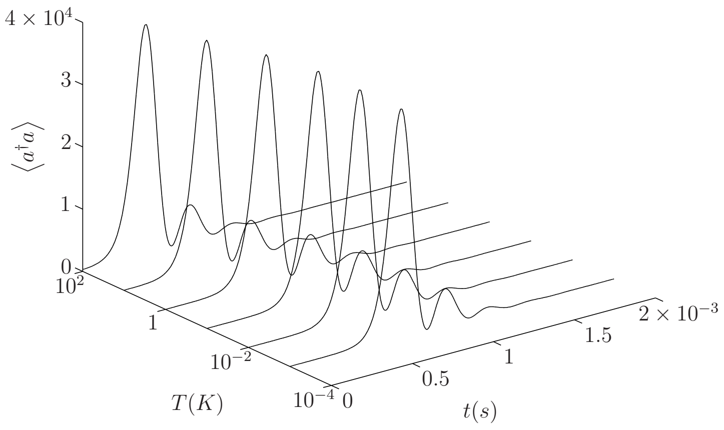

Figure 3.13.: Dynamics of the photon number in the cavity with increasing temperature. The onset of the superradiant emission is shifted to earlier times since the initially present thermal photons contribute to the fluctuations that trigger the emission process.

photons, which can be seen in Fig. 3.12 (c). Due to the large number of emitted photons it should be clearly detectable even on a fairly high thermal background. Following the pulse shape, one also can extract the effective coupling parameters to characterize the system.

The process of superradiance can create a transient entangled state of the ensemble [3.23]. This entanglement can be revealed by entanglement witnesses which can be inferred from the calculated observables. We have seen some indication of such entanglement appearing. However, the persistence of the entanglement under the influence of noise and with the presence of the cavity will be part of future work.

The onset of superradiant emission is determined by spontaneously emitted photons that trigger the forthcoming burst of radiation. The presence of thermal photons is expected to reduce the time until the onset of the burst. This behavior is recovered by our equations as shown in Fig. 3.13, where we depict the dynamics of the photon number in the cavity for different temperatures.

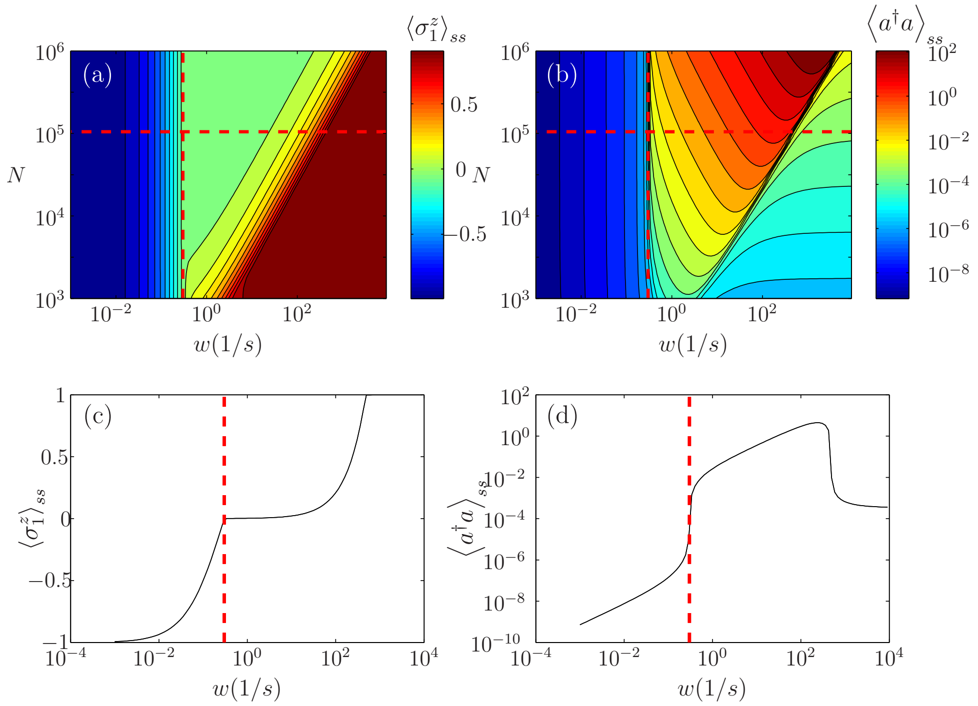

Figure 3.14.: (Color online) Steady-state inversion of the ensemble (a) and occupation of the cavity mode (b) for varying ensemble size N and pump strength w. The temperature was chosen to be $T_1 = 0.001$ K, which corresponds to an empty cavity ($\bar{n} = 0$). Vertical red dashed lines mark the masing threshold $w = \gamma_a = 0.3$. The horizontal red dashed lines at $N = 10^5$ indicate the position of the curves shown in (c) and (d). From (c) we recover the passage of the inversion through zero for $w = \gamma_a = 0.3$. At this point we see in (d) a rapid increase of the photon number in the mode.

3.13. Narrowbandwidth hyperfine micromaser

The collectively coupled ensemble can be used to construct a stripline micromaser with a very low linewidth. To this aim the inversion of the ensemble is sustained by an external incoherent pump of the atoms. In contrast to the calculations in Sec. 3.8, we ignore the fact that the cavity radiates into a thermally occupied reservoir. After passing the masing threshold, the thermal occupation outside becomes negligible. To determine the linewidth of the emitted light we calculate the Laplace transform of the two-time correlation function $\left\langle a^\dagger(t)a(0)\right\rangle$. Using the quantum regression theorem we find

$$\frac{\mathrm{d}}{\mathrm{d}t}\begin{pmatrix}\left\langle a^\dagger(t)a(0)\right\rangle\\ \left\langle\sigma_1^+(t)a(0)\right\rangle\end{pmatrix}=\begin{pmatrix}-\kappa & \mathrm{i}gN\\ -\mathrm{i}g\left\langle\sigma_1^z\right\rangle_{ss} & -\frac{w+\gamma_a}{2}\end{pmatrix}\times\begin{pmatrix}\left\langle a^\dagger(t)a(0)\right\rangle\\ \left\langle\sigma_1^+(t)a(0)\right\rangle\end{pmatrix}\ . \tag{3.13.1}$$

Laplace Transform of Eq. (3.13.1) gives

$$\begin{pmatrix}\kappa+s & -\mathrm{i}gN\\ \mathrm{i}g\left\langle\sigma_1^z\right\rangle_{ss} & \frac{w+\gamma_a}{2}+s\end{pmatrix}\times\begin{pmatrix}\langle\widetilde{a^\dagger(t)a(0)}\rangle\\ \left\langle\widetilde{\sigma_1^+(t)a(0)}\right\rangle\end{pmatrix}=\begin{pmatrix}\left\langle a^\dagger a\right\rangle_{ss}\\ \left\langle\sigma_1^+a\right\rangle_{ss}\end{pmatrix}\ , \tag{3.13.2}$$

where $\langle\ \cdot\ \rangle_{ss}$ denotes steady state values and $\widetilde{\ \cdot\ }$ denotes Laplace transformed quantities.

The steady-state values on the right-hand side of Eq. (3.13.2) can be obtained analytically. Setting the time derivatives of the dynamical equations to zero, a quadratic equation for $\left\langle\sigma_1^z\right\rangle_{ss}$ is attained. One of the solutions yields a physically meaningful result for calculating the remaining steady-state values and hence $\left\langle a^\dagger a\right\rangle_{ss}$ and $\left\langle\sigma_1^+a\right\rangle_{ss}$. To illustrate the effect of the increasing pump strength, we show the steady-state inversion of the ensemble and the occupation of the cavity in Figs. 3.14 and 3.17. Once the critical pump strength is reached, the systems behave identically for different temperatures. The number of atoms in the ensemble is varied between 10^3 and 10^6, whereas the pump parameter w ranges from 10^{-3} to 10^4. In both figures we mark the pump strength $w=\gamma_a=0.3$, for which we find the inversion becomes positive, with a vertical red dashed line. At this point we also find a rapid increase of the number of photons in the cavity. The horizontal lines mark the cross sections for $N=10^5$ shown in what follows.

To solve for $\langle\widetilde{a^\dagger(t)a(0)}\rangle$, we use Cramers rule on Eq. (3.13.2), which yields

$$\langle\widetilde{a^\dagger(t)a(0)}\rangle(s)=\frac{\left\langle a^\dagger a\right\rangle_{ss}\left(\frac{w+\gamma_a}{2}+s\right)-\mathrm{i}gN\left\langle\sigma_1^+a\right\rangle_{ss}}{(\kappa+s)(\frac{w+\gamma_a}{2}+s)-g^2N\left\langle\sigma_1^z\right\rangle_{ss}}\ , \tag{3.13.3}$$

so that with $s=-\mathrm{i}\omega$ the spectrum is given by

$$\mathrm{S}\left(\omega\right)=\frac{1}{2\pi}\left(\langle\widetilde{a^\dagger(t)a(0)}\rangle\left(\omega\right)+\langle\widetilde{a^\dagger(t)a(0)}\rangle^*\left(\omega\right)\right)\ . \tag{3.13.4}$$

For each set of parameters we calculate the spectrum and determine the linewidth numerically. The linewidth of the maser for two different temperatures $T_1=0.001$ K and $T_2=0.1$ K is shown in Figs. 3.15(a) and 3.16(a). For $w=\gamma_a=0.3$ we see a

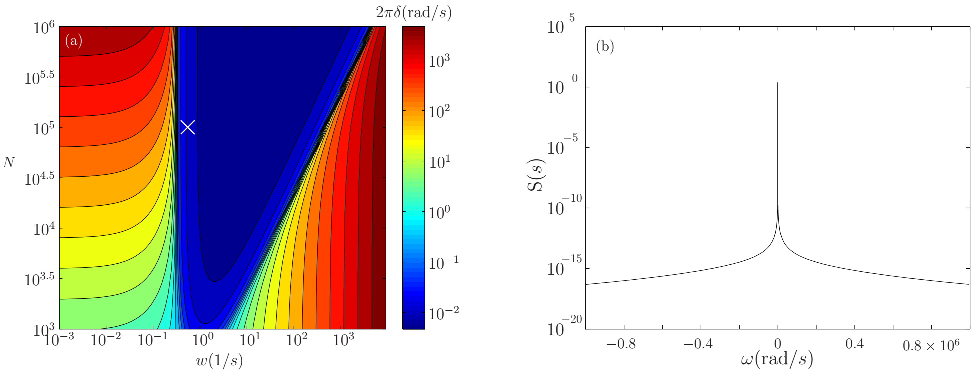

Figure 3.15.: (Color online) (a) Linewidth of the spectrum $\mathrm{S}\,(\omega)$. For each set of parameters we numerically determine the linewidth of the spectrum. The parameters were chosen to be $\kappa = 7 \times 10^5$, $\gamma_a = 0.3$, $g = 40$, $\omega_m = \omega_a = 2\pi \times 6.83 \times 10^9$, $T = 0.001$. (b) Exemplary spectrum for $N = 10^5$ and $w = 0.55$, marked in (a) by the white cross.

rapid drop in the linewidth for both temperatures and a resulting minimal linewidth of $\delta = \frac{1}{2\pi} 4.7 \times 10^{-3}$ Hz. Above the critical pump strength the pump noise destroys the coherence between the individual atoms [3.9]. In in Figs. 3.15(b) and 3.16(b) we plot exemplary spectra for $N = 10^5$ and $w = 0.55$, marked by the white cross.

For $T_2 = 0.1$ K the cavity contains on average $\bar{n} = 0.04$ photons that can be recovered from the constant background in Figs. 3.17(b) and 3.17(d). Since the number of thermal photons is small compared to the considered ensembles, the inversion is nonsensitive to the increased temperature.

In Fig. 3.16 we recover the linewidth of the cavity $\kappa = 7 \times 10^5$ if the pump is below threshold and again if the pump exceeds a critical strength $w_{\max}$. Above $w_{\max}$ the coherence between different spins is destroyed by the pump noise [3.9]. The behavior between the threshold and $w_{\max}$ resembles the behavior for $T = 0.001$ K shown in Fig. 3.15.

3.14. Conclusions

Our studies show that a hybrid cavity QED system consisting of a stripline microwave resonator at finite T and an ensemble of ultracold atoms is a rich and versatile setup for observing and testing prominent quantum physics phenomena. The effectively very cold temperature and good localization of the atomic cloud al-

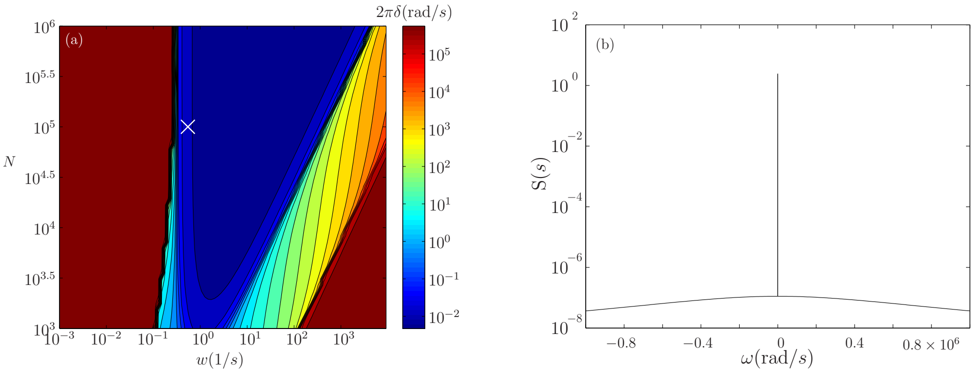

Figure 3.16.: (Color online) Finite temperature effects in the spectrum. Panel (a) again shows the linewidth of the spectrum. Below the critical pump strength we recover the linewidth of the cavity. The parameters were chosen to be $\kappa = 7 \times 10^5$, $\gamma_a = 0.3$, $g = 40$, $\omega_g = \omega_a = 2\pi \times 6.83 \times 10^9$, $T = 0.1$. (b): Exemplary spectrum for $N = 10^5$ and $w = 0.55$, marked in (a) by the white cross.

low symmetric collective strong coupling to the microwave mode. While the weak magnetic dipole coupling requires large atom numbers and an extremely well localized microwave mode to obtain significant coupling, it also makes the system quite immune to external noise. In addition to the long lifetime of the atomic states, this renders the system an ideal quantum memory or allows for very narrow spectral response or gain. As all the atoms are identical and well trapped, the system exhibits only a very narrow inhomogeneous broadening. Operated in an active way, one thus can envisage a truly microscopic maser with an very narrow linewidth directly locked to an atomic clock transition. The uniform coupling and the possibility of efficient optical pumping enables the study of superradiant decay into the stripline mode, where a precise phase and intensity analysis of the emitted radiation can be performed.

While many of our considerations are guided by parameters expected from an ultracold atom ensemble, it is easy to generalize to alternative setups using NV-centers or other solid-state ensembles. There larger ensembles can be easily envisaged but one also gets much more varying coupling constants and larger inhomogeneous widths. It is not obvious whether the technically more simple setup and larger numbers in this case can compensate for these imperfections.

This could be particularly important for a next step: possible optical readout of the ensemble. For the atomic case, the uniformity of the coupling over many optical wavelengths should allow a nice directional readout of the ensemble state, once a laser could coupled in.

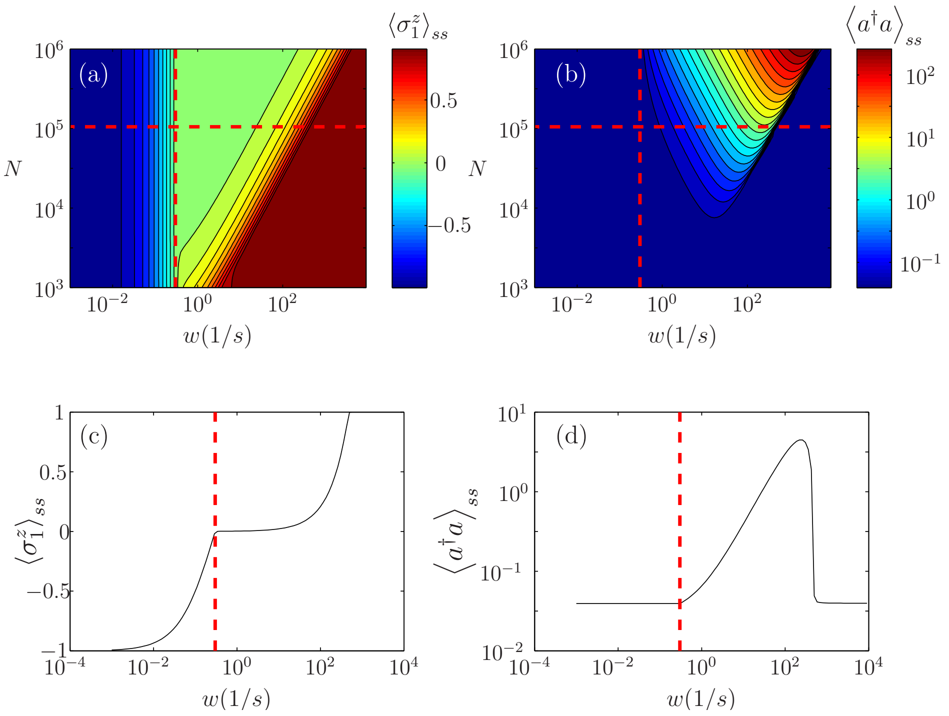

Figure 3.17.: (Color online) Same as Fig. 3.14 with $T_2 = 0.1$, which corresponds to $\bar{n} = 0.04$. In (d) the thermal excitations in the mode appear as a constant background from which the increase due to the pump stands out.

3.15. Acknowledgment

This work was supported by a DOC-fFORTE-fellowship of the Austrian Academy of Sciences and the European Union project MIDAS.

3.16. Appendix A: Coupled Equations

Transformation to a rotating frame with respect to the frequency of the pump ω_l results in $\Delta_m = \omega_m - \omega_l$ for the detuning of the cavity and $\Delta_a = \omega_a - \omega_l$ for the detuning of the atoms. The coupled equations are given by:

$$
\begin{aligned}
\frac{\mathrm{d}}{\mathrm{d}t}\left\langle a\right\rangle &= -\left(\kappa+\mathrm{i}\Delta_m\right)\left\langle a\right\rangle - \mathrm{i}gN\left\langle \sigma_1^-\right\rangle + \eta && (3.16.1)\\
\frac{\mathrm{d}}{\mathrm{d}t}\left\langle a^\dagger\right\rangle &= -\left(\kappa-\mathrm{i}\Delta_m\right)\left\langle a^\dagger\right\rangle + \mathrm{i}gN\left\langle \sigma_1^+\right\rangle + \eta^* && (3.16.2)
\end{aligned}
$$

$$
\begin{aligned}
\frac{\mathrm{d}}{\mathrm{d}t}\left\langle \sigma_1^z\right\rangle = &- \gamma_a\left(1+\left\langle \sigma_1^z\right\rangle\right)\\
&- 2\mathrm{i}g\left(\left(\left\langle \sigma_1^+ a\right\rangle_c + \left\langle \sigma_1^+\right\rangle\left\langle a\right\rangle\right) - \left(\left\langle \sigma_1^- a^\dagger\right\rangle_c + \left\langle \sigma_1^-\right\rangle\left\langle a^\dagger\right\rangle\right)\right) && (3.16.3)\\
\frac{\mathrm{d}}{\mathrm{d}t}\left\langle \sigma_1^-\right\rangle = &-\left(\frac{\gamma_a}{2}+\mathrm{i}\Delta_a\right)\left\langle \sigma_1^-\right\rangle + \mathrm{i}g\left(\left\langle \sigma_1^z a\right\rangle_c + \left\langle \sigma_1^z\right\rangle\left\langle a\right\rangle\right) && (3.16.4)\\
\frac{\mathrm{d}}{\mathrm{d}t}\left\langle \sigma_1^+\right\rangle = &-\left(\frac{\gamma_a}{2}-\mathrm{i}\Delta_a\right)\left\langle \sigma_1^+\right\rangle - \mathrm{i}g\left(\left\langle \sigma_1^z a^\dagger\right\rangle_c + \left\langle \sigma_1^z\right\rangle\left\langle a^\dagger\right\rangle\right) && (3.16.5)
\end{aligned}
$$

$$
\begin{aligned}
\frac{\mathrm{d}}{\mathrm{d}t}\left(\left\langle a\sigma_1^+\right\rangle_c + \left\langle a\right\rangle\left\langle \sigma_1^+\right\rangle\right) = &-\left(\kappa+\frac{\gamma_a}{2}+\mathrm{i}\left(\Delta_m-\Delta_a\right)\right)\left(\left\langle a\sigma_1^+\right\rangle_c + \left\langle a\right\rangle\left\langle \sigma_1^+\right\rangle\right)\\
&- \mathrm{i}g\left(\frac{\left\langle \sigma_1^z\right\rangle+1}{2} + (N-1)\left(\left\langle \sigma_1^+\sigma_2^-\right\rangle_c + \left\langle \sigma_1^+\right\rangle\left\langle \sigma_2^-\right\rangle\right)\right)\\
&- \mathrm{i}g\left\langle \sigma_1^z a^\dagger a\right\rangle + \eta\left\langle \sigma_1^+\right\rangle && (3.16.6)
\end{aligned}
$$

$$
\begin{aligned}
&\frac{\mathrm{d}}{\mathrm{d}t}\left(\left\langle a\sigma_1^z\right\rangle_c + \left\langle \sigma_1^z\right\rangle\left\langle a\right\rangle\right) = -\left(\kappa+\mathrm{i}\Delta_m\right)\left(\left\langle a\sigma_1^z\right\rangle_c + \left\langle \sigma_1^z\right\rangle\left\langle a\right\rangle\right) + \eta\left\langle \sigma_1^z\right\rangle\\
&- 2\gamma_a\left(\left\langle a\sigma_1^+\right\rangle_c\left\langle \sigma_1^-\right\rangle + \left\langle a\sigma_1^-\right\rangle_c\left\langle \sigma_1^+\right\rangle + \left\langle a\right\rangle\left\langle \sigma_1^+\sigma_1^-\right\rangle\right)\\
&- \mathrm{i}g\Big[2\left(2\left\langle \sigma_1^+ a\right\rangle_c\left\langle a\right\rangle + \left\langle aa\right\rangle_c\left\langle \sigma_1^+\right\rangle + \left\langle a\right\rangle\left\langle a\right\rangle\left\langle \sigma_1^+\right\rangle\right) && (3.16.7)\\
&\qquad - \left(1+2\left\langle a^\dagger a\right\rangle_c\right)\left\langle \sigma_1^-\right\rangle - 2\left\langle a\sigma_1^-\right\rangle_c\left\langle a^\dagger\right\rangle\\
&\qquad -2\left\langle a^\dagger\sigma_1^-\right\rangle_c\left\langle a\right\rangle - 2\left\langle a^\dagger\right\rangle\left\langle a\right\rangle\left\langle \sigma_1^-\right\rangle\\
&\qquad + (N-1)\left(\left\langle \sigma_1^z\sigma_2^-\right\rangle_c + \left\langle \sigma_1^z\right\rangle\left\langle \sigma_2^-\right\rangle\right)\Big]
\end{aligned}
$$

$$
\begin{aligned}
\frac{\mathrm{d}}{\mathrm{d}t}\left(\left\langle \sigma_1^+\sigma_2^- \right\rangle_c + \left\langle \sigma_1^+ \right\rangle \left\langle \sigma_2^+ \right\rangle\right) = &- \mathrm{i}g\left[\left\langle \sigma_1^z\sigma_2^- \right\rangle_c \left\langle a^\dagger \right\rangle + \left\langle \sigma_1^z a^\dagger \right\rangle_c \left\langle \sigma_1^- \right\rangle\right.\\
&+ \left\langle \sigma_1^- a^\dagger \right\rangle_c \langle \sigma_1^z \rangle + \left\langle \sigma_1^- \right\rangle \langle \sigma_1^z \rangle \left\langle a^\dagger \right\rangle\\
&- \left(\left\langle \sigma_1^z\sigma_2^+ \right\rangle_c \langle a \rangle + \langle \sigma_1^z a \rangle_c \left\langle \sigma_1^+ \right\rangle\right.\\
&\left.\left. + \left\langle \sigma_1^+ a \right\rangle_c \langle \sigma_1^z \rangle + \left\langle \sigma_1^+ \right\rangle \langle \sigma_1^z \rangle \langle a \rangle\right)\right]\\
&- \gamma_a\left(\left\langle \sigma_1^+\sigma_2^- \right\rangle_c + \left\langle \sigma_1^+ \right\rangle \left\langle \sigma_2^- \right\rangle\right)
\end{aligned}
\tag{3.16.8}
$$

$$
\begin{aligned}
\frac{\mathrm{d}}{\mathrm{d}t}\left(\left\langle a^\dagger a \right\rangle_c + \left\langle a^\dagger \right\rangle \langle a \rangle\right) = &- \mathrm{i}gN\left(\left(\left\langle a^\dagger\sigma_1^- \right\rangle_c + \left\langle a^\dagger \right\rangle \left\langle \sigma_1^- \right\rangle\right)\right.\\
&\left.- \left(\left\langle a\sigma_1^+ \right\rangle_c + \langle a \rangle \left\langle \sigma_1^+ \right\rangle\right)\right)\\
&- 2\kappa\left(\left\langle a^\dagger a \right\rangle_c + \left\langle a^\dagger \right\rangle \langle a \rangle\right) + 2\kappa\bar{n} + \eta^* \langle a \rangle + \eta \left\langle a^\dagger \right\rangle
\end{aligned}
\tag{3.16.9}
$$

$$
\begin{aligned}
\frac{\mathrm{d}}{\mathrm{d}t}\left(\left\langle a\sigma_1^- \right\rangle_c + \langle a \rangle \left\langle \sigma_1^- \right\rangle\right) = &- \left(\mathrm{i}\left(\Delta_m + \Delta_a\right) + \kappa + \frac{\gamma_a}{2}\right)\left(\left\langle a\sigma_1^- \right\rangle_c + \langle a \rangle \left\langle \sigma_1^- \right\rangle\right)\\
&- \mathrm{i}g(N-1)\left(\left\langle \sigma_1^-\sigma_2^- \right\rangle_c + \left\langle \sigma_1^- \right\rangle \left\langle \sigma_1^- \right\rangle\right) + \eta \left\langle \sigma_1^- \right\rangle\\
&+ \mathrm{i}g\left(2\left\langle \sigma_1^z a \right\rangle_c \langle a \rangle + \langle aa \rangle_c \langle \sigma_1^z \rangle + \langle a \rangle \langle a \rangle \langle \sigma_1^z \rangle\right)
\end{aligned}
\tag{3.16.10}
$$

$$
\begin{aligned}
\frac{\mathrm{d}}{\mathrm{d}t}\left(\left\langle a^\dagger a^\dagger \right\rangle_c - \left\langle a^\dagger \right\rangle \left\langle a^\dagger \right\rangle\right) = &- \left(2\kappa - \mathrm{i}2\Delta_m\right)\left(\left\langle a^\dagger a^\dagger \right\rangle_c + \left\langle a^\dagger \right\rangle \left\langle a^\dagger \right\rangle\right)\\
&+ 2\mathrm{i}gN\left(\left\langle \sigma_1^+ a^\dagger \right\rangle_c + \left\langle a^\dagger \right\rangle \left\langle \sigma_1^+ \right\rangle\right) + 2\eta^* \left\langle a^\dagger \right\rangle
\end{aligned}
\tag{3.16.11}
$$

$$
\begin{aligned}
\frac{\mathrm{d}}{\mathrm{d}t}\left(\left\langle\sigma_1^-\sigma_2^-\right\rangle_c+\left\langle\sigma_1^-\right\rangle\left\langle\sigma_1^-\right\rangle\right) = &-2\left(\frac{\gamma_a}{2}+\mathrm{i}\Delta_a\right)\left(\left\langle\sigma_1^-\sigma_2^-\right\rangle_c+\left\langle\sigma_1^-\right\rangle\left\langle\sigma_2^-\right\rangle\right)\\
&+\mathrm{i}2g\Big(\left\langle\sigma_1^z\sigma_2^-\right\rangle_c\langle a\rangle+\langle\sigma_1^z a\rangle_c\left\langle\sigma_1^-\right\rangle\\
&+\left\langle\sigma_1^- a\right\rangle_c\langle\sigma_1^z\rangle+\langle\sigma_1^z\rangle\left\langle\sigma_1^-\right\rangle\langle a\rangle\Big)
\end{aligned}
\tag{3.16.12}
$$

$$
\begin{aligned}
&\frac{\mathrm{d}}{\mathrm{d}t}\left(\left\langle\sigma_1^z\sigma_2^+\right\rangle_c+\langle\sigma_1^z\rangle\left\langle\sigma_1^+\right\rangle\right) = \left(-\frac{\gamma_a}{2}+\mathrm{i}\Delta_a\right)\left(\left\langle\sigma_1^z\sigma_2^+\right\rangle_c+\langle\sigma_1^z\rangle\left\langle\sigma_2^+\right\rangle\right)\\
&-2\gamma_a\left(\left\langle\sigma_1^+\sigma_1^-\right\rangle\left\langle\sigma_1^+\right\rangle+\left\langle\sigma_1^+\sigma_2^+\right\rangle_c\left\langle\sigma_1^-\right\rangle+\left\langle\sigma_1^-\sigma_2^+\right\rangle_c\left\langle\sigma_1^+\right\rangle\right)\\
&-\mathrm{i}g\Big[2\Big(\left\langle\sigma_1^+\sigma_2^+\right\rangle_c\langle a\rangle+2\left\langle\sigma_1^+ a\right\rangle_c\left\langle\sigma_1^+\right\rangle\\
&\qquad+\left\langle\sigma_1^+\right\rangle\left\langle\sigma_1^+\right\rangle\langle a\rangle-\left\langle\sigma_1^-\sigma_2^+\right\rangle_c\left\langle a^\dagger\right\rangle-\\
&\qquad\left\langle\sigma_1^- a^\dagger\right\rangle_c\left\langle\sigma_1^+\right\rangle-\left\langle\sigma_1^+ a^\dagger\right\rangle_c\left\langle\sigma_1^-\right\rangle\\
&\qquad-\left\langle\sigma_1^+\right\rangle\left\langle\sigma_1^-\right\rangle\left\langle a^\dagger\right\rangle\Big)+\\
&\qquad\ \langle\sigma_1^z\sigma_2^z\rangle_c\left\langle a^\dagger\right\rangle+2\left\langle\sigma_1^z a^\dagger\right\rangle_c\langle\sigma_1^z\rangle+\langle\sigma_1^z\rangle\langle\sigma_1^z\rangle\left\langle a^\dagger\right\rangle\Big]
\end{aligned}
\tag{3.16.13}
$$

$$
\begin{aligned}
\frac{\mathrm{d}}{\mathrm{d}t}\left(\langle\sigma_1^z\sigma_2^z\rangle_c+\langle\sigma_1^z\rangle\langle\sigma_1^z\rangle\right) = &-4\mathrm{i}g\Big(\left\langle\sigma_1^z\sigma_2^+\right\rangle_c\langle a\rangle+\langle\sigma_1^z a\rangle_c\left\langle\sigma_1^+\right\rangle+\left\langle\sigma_1^+ a\right\rangle_c\langle\sigma_1^z\rangle\\
&+\langle a\rangle\langle\sigma_1^z\rangle\left\langle\sigma_1^+\right\rangle-\left\langle\sigma_1^-\sigma_2^z\right\rangle_c\left\langle a^\dagger\right\rangle-\left\langle\sigma_1^z a^\dagger\right\rangle_c\left\langle\sigma_1^-\right\rangle\\
&-\left\langle\sigma_1^- a^\dagger\right\rangle_c\langle\sigma_1^z\rangle-\left\langle a^\dagger\right\rangle\left\langle\sigma_1^-\right\rangle\langle\sigma_1^z\rangle\Big)\\
&-4\gamma_a\left(\left\langle\sigma_1^+\sigma_1^-\right\rangle\langle\sigma_1^z\rangle+\left\langle\sigma_1^+\sigma_2^z\right\rangle_c\left\langle\sigma_1^-\right\rangle+\left\langle\sigma_1^-\sigma_2^z\right\rangle_c\left\langle\sigma_1^+\right\rangle\right)
\end{aligned}
\tag{3.16.14}
$$

3.17. Appendix B: Validity of the cumulant expansion

The validity of the truncation of the expansion performed previously relies on the assumption that higher-order cumulants are negligible. This can be checked in principle by truncating at higher orders and comparing the results. In general,

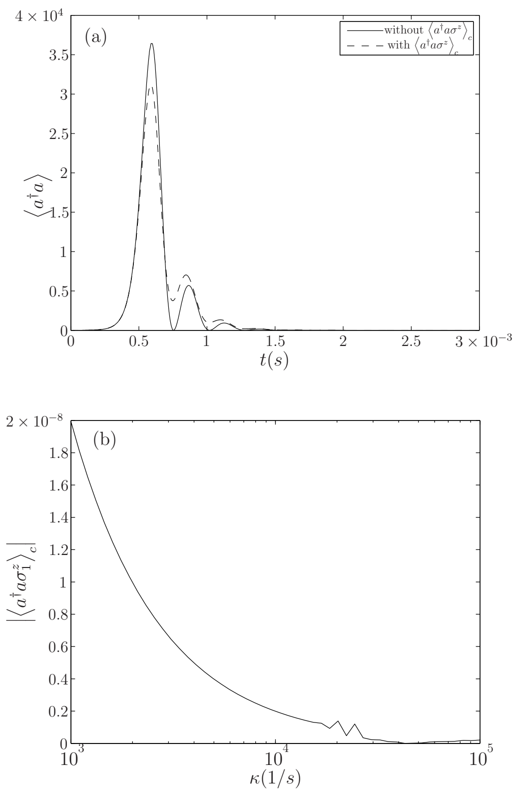

Figure 3.18.: (a) Dynamics of the photon number in the cavity mode for an initially fully inverted ensemble. The solid line shows the dynamics produced by the set of equations where $\langle a^\dagger a\sigma_1^z\rangle_c$ was neglected. The dashed curve is the result of the full set of 13 equations in which $\langle a^\dagger a\sigma_1^z\rangle_c$ is kept. (b) Numerically obtained cumulant $\langle a^\dagger a\sigma_1^z\rangle_c$ in the steady state. With increasing loss rate of the cavity κ the correlation between photon number and inversion decreases.

it turns out that there is one cumulant which requires more care: the correlation between the inversion and the photon number $\langle a^\dagger a\sigma_1^z\rangle$. In the regime where $\frac{g_{\text{eff}}}{\kappa} > 1$ and $\frac{g_{\text{eff}}}{\gamma_a} > 1$ holds, the number of photons necessary to saturate the ensemble is low. Therefore small fluctuations of the photon number can cause significant changes in the inversion [3.24]. The correlation between the photon number and the inversion $\langle a^\dagger a\sigma_1^z\rangle_c$ is therefore kept in our calculations. Hence, an expansion like in Eq. (3.7.2) would not be advantageous because none of the terms could be dropped. We therefore calculate the dynamical equation for $\langle a^\dagger a\sigma_1^z\rangle$ which gives

$$\begin{aligned}\frac{\mathrm{d}}{\mathrm{d}t}\left\langle a^\dagger a\sigma_1^z\right\rangle &= \left(-2\kappa-\gamma_a\right)\left\langle a^\dagger a\sigma_1^z\right\rangle-\gamma_a\left\langle a^\dagger a\right\rangle+2\kappa\bar{n}\left\langle\sigma_1^z\right\rangle\\ &-\mathrm{i}g\left(\left\langle a\sigma_1^+\right\rangle-\left\langle a^\dagger\sigma_1^-\right\rangle+2\left(\left\langle a^\dagger aa\sigma_1^+\right\rangle-\left\langle a^\dagger a^\dagger a\sigma_1^-\right\rangle\right)\right)\\ &-\mathrm{i}g\left(N-1\right)\left(\left\langle a^\dagger\sigma_1^z\sigma_2^-\right\rangle-\left\langle a\sigma_1^z\sigma_2^+\right\rangle\right)\\ &+\eta\left\langle a^\dagger\sigma_1^z\right\rangle+\eta^*\left\langle a\sigma_1^z\right\rangle\end{aligned} \tag{3.17.1}$$

The expectation values of products of three operators are expanded as in Eq. (3.7.2), except for $\left\langle a^\dagger a\sigma_1^z\right\rangle$. The expansion of expectation values with four operators is more involved and produces also expectation values of products of three operators which are again expanded. Cumulants of order three and four are neglected. The resulting equation for $\left\langle a^\dagger a\sigma_1^z\right\rangle$ can be integrated numerically along with the equations for the other quantities mentioned previously.

To estimate the influence of the correlation between the photon number and the inversion $\left\langle a^\dagger a\sigma_1^z\right\rangle_c$ on the dynamics we plot the photon number in the cavity during the decay of a fully inverted ensemble. We therefore integrate a set of 12 equations that is obtained if $\left\langle a^\dagger a\sigma_1^z\right\rangle$ is expanded and $\left\langle a^\dagger a\sigma_1^z\right\rangle_c$ is neglected. For comparison we also show the dynamics obtained from the full set of 13 equations in which $\left\langle a^\dagger a\sigma_1^z\right\rangle_c$ is kept [see Fig. 3.18 (a)].

The steady state of both solutions differs only slightly. The correlation $\left\langle a^\dagger a\sigma_1^z\right\rangle_c$ is shown in Fig. 3.18 (b). With increasing cavity decay rate κ the correlation between photon number and inversion decreases.

References for Chapter 3

[3.1] M. Tavis and F.W. Cummings. “Exact solution for an N-molecule—radiation-field Hamiltonian.” In: *Physical Review* 170.2 (1968), pp. 379–384.

[3.2] L.M. Duan et al. “Long-distance quantum communication with atomic ensembles and linear optics.” In: *Nature* 414.6862 (2001), pp. 413–418.

[3.3] P. Rabl et al. “Hybrid quantum processors: molecular ensembles as quantum memory for solid state circuits.” In: *Physical review letters* 97.3 (2006), p. 33003.

[3.4] A. Imamoglu. “Cavity-QED based on collective magnetic dipole coupling: spin ensembles as hybrid two-level systems.” In: *Arxiv preprint arXiv:0809.2909* (2008).

[3.5] J. Verdú et al. “Strong magnetic coupling of an ultracold gas to a superconducting waveguide cavity.” In: *Physical Review Letters* 103.4 (2009), p. 43603.

[3.6] A. Wallraff et al. “Strong coupling of a single photon to a superconducting qubit using circuit quantum electrodynamics.” In: *Nature* 431.7005 (2004), pp. 162–167.

[3.7] P. Böhi et al. “Coherent manipulation of Bose–Einstein condensates with state-dependent microwave potentials on an atom chip.” In: *Nature Physics* 5 (2009), pp. 592–597.

[3.8] M.R. Matthews et al. “Dynamical response of a Bose-Einstein condensate to a discontinuous change in internal state.” In: *Physical Review Letters* 81.2 (1998), pp. 243–247.

[3.9] D. Meiser et al. “Prospects for a Millihertz-Linewidth Laser.” In: *Phys Rev Lett* 102 (2009), p. 163601.

[3.10] S. Haroche and J.M. Raimond. *Exploring the quantum: atoms, cavities and photons.* Oxford University Press, USA, 2006.

[3.11] R.H. Dicke. “Coherence in spontaneous radiation processes.” In: *Physical Review* 93.1 (1954), pp. 99–110.

[3.12] F. Haake et al. “Superradiant laser.” In: *Physical review letters* 71.7 (1993), pp. 995–998.

[3.13] B Kasch et al. “Cold atoms near superconductors: atomic spin coherence beyond the Johnson noise limit.” In: *New Journal of Physics* 12.6 (2010), p. 065024.

[3.14] C.W. Gardiner. *Handbook of stochastic methods.* Springer Berlin, 1985.

[3.15] H.J. Carmichael. *Statistical methods in quantum optics 1: Master Equations and Fokker-Planck Equations.* Springer, 1999.

[3.16] S.M. Tan. “A computational toolbox for quantum and atomic optics.” In: *Journal of Optics B: Quantum and Semiclassical Optics* 1 (1999), pp. 424–432.

[3.17] R. Kubo. “Generalized cumulant expansion method.” In: *J. Phys. Soc. Japan* 17.7 (1962), pp. 1100–1120.

[3.18] H.J. Carmichael. “Spectrum of squeezing and photocurrent shot noise: a normally ordered treatment.” In: *Journal of the Optical Society of America B* 4.10 (1987), pp. 1588–1603.

[3.19] M.B. Plenio and P.L. Knight. “The quantum-jump approach to dissipative dynamics in quantum optics.” In: *Reviews of Modern Physics* 70.1 (1998), pp. 101–144.

[3.20] P. Zoller, M. Marte, and DF Walls. “Quantum jumps in atomic systems.” In: *Physical Review A* 35.1 (1987), pp. 198–207.

[3.21] C.W. Gardiner and P. Zoller. *Quantum noise.* Springer Berlin, 1991.

[3.22] M. Gross and S. Haroche. “Superradiance: an essay on the theory of collective spontaneous emission.” In: *Phys. Rep* 93.5 (1982), pp. 301–396.

[3.23] P. Milman. “Witnessing entanglement from N-qubit radiation emission.” In: *Physical Review A* 74.4 (2006), p. 42317.

[3.24] P.R. Rice and H.J. Carmichael. “Photon statistics of a cavity-QED laser: A comment on the laser-phase-transition analogy.” In: *Phys Rev A* 50.5 (1994), pp. 4318–4329.

4. Publication

PRL 107, 060502 (2011) PHYSICAL REVIEW LETTERS week ending 5 August 2011

Cavity QED with magnetically coupled collective spin states[†]

R. Amsüss[1], Ch. Koller[1,2], T. Nöbauer[1], S. Putz[1], S. Rotter[3], K.Sandner[4],
S. Schneider[1], M. Schramböck[1,2], G. Steinhauser[1], H. Ritsch[4], J. Schmiedmajer[1],
and J. Majer[1,2]

[1] *Vienna Center for Quantum Science and Technology, Atominstitut,*
TU Wien, 1020 Vienna, Austria
[2] *Center for Micro- and Nanostructures ZNMS, TU Wien, 1040 Vienna, Austria*
[3] *Institute for Theoretical Physics, TU Wien, 1040 Vienna, Austria*
[4] *Institute for Theoretical Physics, University of Innsbruck Technikerstr. 25, 6020 Innsbruck,*
Austria

We report strong coupling between an ensemble of nitrogen-vacancy center electron spins in diamond and a superconducting microwave coplanar waveguide resonator. The characteristic scaling of the collective coupling strength with the square root of the number of emitters is observed directly. Additionally, we measure hyperfine coupling to ^{13}C nuclear spins, which is a first step towards a nuclear ensemble quantum memory. Using the dispersive shift of the cavity resonance frequency, we measure the relaxation time of the NV center at mK temperatures in a non-destructive way.

PACS numbers: 03.67.-a,42.50.Pq,61.72.jn,76.30.-v

Building a practical quantum information processor will profit from a hybridization of different quantum systems in order to fulfill the requirements of long storage times,

---

[†] The author of the present thesis acted in an advisory role concerning the interpretation of the measured transmission signals.

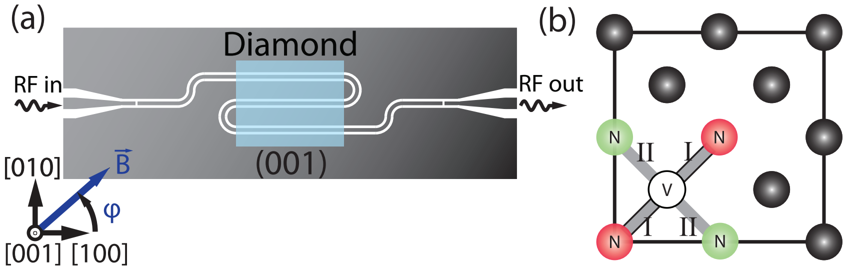

Figure 4.1.: (a) (Color online) Schematic of the experimental setup. A (001) diamond is positioned in the middle and parallel to the surface of a $\lambda/2$ CPW resonator. The chip dimensions are 12×4 mm, the center conductor is 20 μm wide, the gaps are 8.3 μm. A 2-axis Helmholtz coil configuration creates a magnetic field in an arbitrary direction φ within the (001) plane, tuning the NV centers. (b) Sketch of a diamond lattice with the four possible NV center orientations. Due to the diamond symmetry, the NV ensembles denoted as I (red) and II (green) are tuned equivalently, since these ensembles enclose the same angle with the applied magnetic field.

fast processing speeds, long-distance information transfer and scalability. A variety of hybrid systems have been conceived, including cold atoms and ions, nanomechanics, and molecules [4.1–4.6]. Superconducting (SC) qubits [4.7] are appealing processing devices due to the fast processing speed and their customizability. Superconducting coplanar waveguide (CPW) resonators have been used to reversibly transfer quantum states between two qubits and the resonator [4.8]. Color centers in solids on the other hand – most prominently the negatively charged nitrogen-vacancy defect in diamond (NV) – show astonishingly long coherence times even at room temperature [4.9] and provide coherent bridges between electron spin resonances (ESR) in the GHz range and optical photons suitable for long-distance transfer [4.10].

The coupling between a single spin and the electromagnetic field is typically rather weak. However, when writing single excitations into ensembles of N spins, it is enhanced by a factor $\sqrt{N}$ [4.11]. Provided that excitations can be coherently written to and retrieved from the ensemble by strong coupling to high-Q resonators, quantum memories can be constructed [4.12, 4.13]. Efforts parallel to this work have succeeded in demonstrating strong ensemble-resonator coupling using NVs [4.14] and other impurity spins [4.15–4.17]. Schemes such as gradient echoes [4.18] and controlled reversible inhomogeneous broadening [4.19] can be used to store quantum information [4.20].

In this Letter, we employ a strongly coupled system consisting of a CPW resonator and an ensemble of NVs to directly demonstrate key features of ensemble coupling, such as the $\sqrt{N}$ scaling of the coupling rate. Properties of the spin ensemble includ-

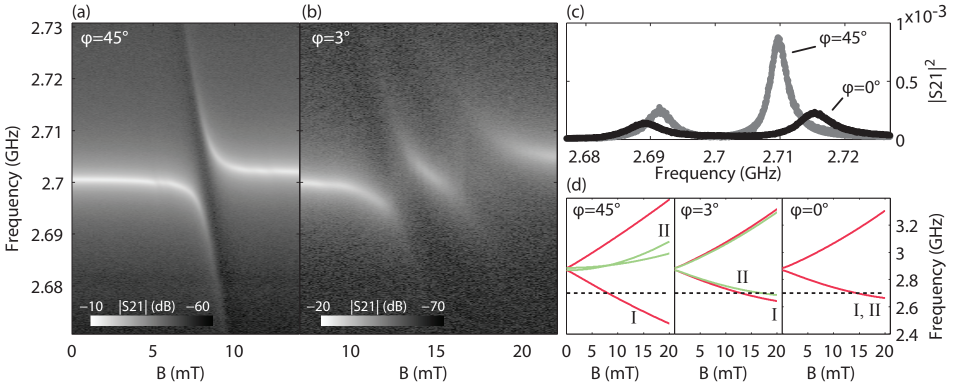

Figure 4.2.: (Color online) Resonator transmission $|S_{21}|^2$ as a function of the magnetic field for (a) $\varphi = 45°$ and (b) $\varphi = 3°$. While in (a) an avoided crossing of the coupled resonator-spin ensemble system is observed when $\omega_r = \omega_-^I$, we see in (b) the additional splitting of the ω_-^{II} transition. (c) Comparison of the vacuum Rabi splitting of $2g_I/2\pi = 18.5$ MHz for $\varphi = 45°$ ($B = 8.2$ mT) (gray line) and the $\sqrt{2}$ larger splitting of $2g/2\pi = 26.3$ MHz (black line) for $\varphi = 0°$ ($B = 14.3$ mT). Each dataset is fitted by a two-peak Lorentzian curve. (d) Transition frequencies $\omega_\pm^I$ and $\omega_\pm^{II}$ between the ground $|0\rangle_{I,II}$ and the excited states $|\pm\rangle_{I,II}$ for different magnetic field angles ($\varphi = 45°, 3°, 0°$).The dashed lines indicate the cavity frequency.

ing the NV spin-lattice relaxation time T_1 and ESR zero-field splitting parameters, are determined via the cavity resonance shift caused by dispersive interactions. We also observe the hyperfine interaction between NVs and nearby ^{13}C nuclear spins.

The experimental setup is sketched in Fig. 4: A $4.5\times2.25\times0.5$ mm^3 high-temperature high-pressure diamond is placed on top of a superconducting coplanar waveguide resonator and fixated via a spring-loaded metallic pin. Our single crystal diamond sample has two polished (100) surfaces and is specified to contain a nitrogen impurity concentration of about 200 ppm. In order to form negatively charged NV defect centers, the sample was neutron irradiated with a fluence of 5×10^{17} cm^{-2} to create vacancies [4.21]. Subsequent annealing for four hours at 900 °C resulted in an NV concentration of about 6 ppm which was determined by comparing the fluorescence intensity of an ensemble to a single NV. Resonator chip and diamond are enclosed in a copper box and positioned in the center of two pairs of perpendicular Helmholtz coils. This coil configuration allows to apply a homogeneous magnetic field B (up to about 25 mT) over the extent of the diamond and allows for adjusting the magnetic field direction in the plane of the resonator surface, without changing the resonators frequency [4.22].

To explain our experimental observations, we consider the spin Hamiltonian of a single NV center [4.23]

$$H_{NV} = g_e\beta_e\mathbf{B}\cdot\mathbf{S} + \mathbf{S}\overset{\leftrightarrow}{\mathbf{D}}\mathbf{S} - g_n\beta_n\mathbf{B}\cdot\mathbf{I} + \mathbf{I}\overset{\leftrightarrow}{\mathbf{A}}\mathbf{S}, \tag{4.0.1}$$

where the first and third term describe the Zeeman interaction of an electronic NV spin ($S = 1$, $g_e = 2.0028$) and a ^{13}C nuclear spin ($I = 1/2$, $g_n = 1.4048$) with an external magnetic field $\mathbf{B}$, the second the zero-field splitting (ZFS) ($D/h =$ 2.877 GHz, $E/h = 7.7$ MHz) of the NV ground state and the last the hyperfine interaction of the electron and nuclear spin (hyperfine coupling parameters $A_{\|}/h =$ 200 MHz, $A_{\perp}/h = 120$ MHz). The Bohr magneton and the nuclear magneton are denoted as β_e and β_n. The eigenenergy spectrum was obtained by diagonalizing the Hamiltonian and confirmed with EasySpin [4.24].

Although the main axis of an NV center is along any of the four crystallographic $\langle 111\rangle$ directions, for the (001) crystal plane there are only two magnetically inequivalent directions, labeled I and II in Fig. 4(b). Hence, applying a magnetic field in an arbitrary direction within the (001) plane divides the whole ensemble of NV centers into two magnetic subensembles due to the electron Zeeman effect. Consequently, each subensemble will be tuned into resonance with the CPW resonator at a different magnetic field value (see Fig. 4(d)). For the CPW resonator, we chose a capacitively coupled $\lambda/2$ niobium SC-resonator, fabricated on sapphire substrate. A meander geometry ensures a large overlap of the magnetic mode volume with the spin ensemble. At zero magnetic field and with the diamond on top, the resonator has a center frequency of $\omega_r/2\pi = 2.701$ GHz and a quality factor $Q \approx 3200$. Comparing these values with the empty and coupling limited resonator ($\omega_r/2\pi = 2.897$ GHz and $Q \approx 4 \times 10^4$) shows that the diamond introduces considerable losses, possibly due to surface conductivity effects [4.25]. All subsequently shown measurements of the resonator S_{21}-parameter are performed by using a vector network analyzer with a probe power corresponding to roughly 8×10^4 photons in the resonator. Lowering the power did not alter the signal, except for lowering the signal to noise ratio [4.26]. During all measurements the temperature was below 60 mK, ensuring a high degree of spin-polarization and a low thermal photon background in the frequency range of interest.

A calculation similar to Verdu *et al.* [4.2] adapted for NV centers (see also Kubo *et al.* [4.14]) shows that the small mode volume of a CPW resonator leads to a coupling strength of $g_0/2\pi \approx 12$ Hz for a single NV center 1 μm above the center conductor. This is not enough to exceed the losses $\kappa/2\pi \approx 0.8$ MHz of the resonator and the decoherence rate of the color center. However, by coupling a large number of spins $N \approx 10^{12}$ collectively to the same electromagnetic mode of the resonator, an enhancement of $g_{col}/2\pi \approx \sqrt{N}g_0/2\pi \approx 10$ MHz allows to enter the strong coupling regime. This can be modeled by a generalized Hamiltonian

$$H = \hbar\omega_r a^\dagger a + \frac{\hbar}{2}\sum_{i,j}\omega_{ij}\sigma^z_{ij} + \hbar\sum_{i,j} g_{ij}(\sigma^+_{ij}a + a^\dagger\sigma^-_{ij}),$$

where the index i runs over the different Zeeman subensembles I, II and j accounts for an inhomogeneous distribution of spin transition frequencies ω_{ij} as well as coupling strengths g_{ij}. The operators σ^+_{ij} and σ^-_{ij} describe the spin raising and lowering operators, $a^\dagger$ and a denote the creation and annihilation of a cavity photon. Although the presence of inhomogeneous broadening of the spin transitions has interesting consequences [4.27, 4.28], the subsequent analysis assumes $\omega_{ij} = \omega_i$. The effective coupling strength then reduces to $g_{col} = \sqrt{\sum_i g_i^2}$. Furthermore, if the number of excitations meets $n_{exc} \ll \sqrt{N}$, the spin ensemble is well approximated by a system of coupled harmonic oscillators [4.29].

For strong coupling, an avoided crossing with a level-splitting of $2g_{col}$ is expected when the ensemble of spins is tuned into resonance with the cavity. Fig. 4(a) shows the transmission through the resonator as the magnetic field amplitude is varied for a field direction of $\varphi = 45°$. There, a large Rabi splitting of $2g_I/2\pi = 18.5$ MHz is observed, corresponding to a single Zeeman subensemble in resonance ($\omega_r = \omega^I_-$). The FWHM linewidths of the two peaks are found to be slightly different $\approx 2\pi \times (4.4, 3.3)$ MHz at the avoided crossing. By applying a field in the [100] direction ($\varphi = 0°$), where the energy levels of the two subensembles I and II coincide, we can directly measure the $\sqrt{N}$-enhancement. Since twice as many spins couple to the field mode, an enhancement compared to the case for $\varphi = 45°$ of $g_{col} \approx \sqrt{2}g_I$ is expected. Indeed we obtain an enhancement by a factor of 1.42 ($2g_{col}/2\pi = 26.3$ MHz). We also note an increase of the linewidth of the two peaks to $\approx 2\pi \times 7.3$ MHz for $\varphi = 0°$. In case the magnetic field projections experienced by the two NV subensembles do not coincide (e.g. $\varphi = +3°$), two distinct avoided crossings are observed (see Fig. 4(b), (d)).

Qualitatively one can understand the observed difference in peak amplitude and peak width in Fig. 4(c) by the presence of higher lying NV states ($|+\rangle_I$, $|-\rangle_{II}$). Including these states leads to a model of three (or more) coupled oscillators, where the peaks do not have equal height and width [4.30]. Furthermore inhomogeneous broadening, which is not contained in a model of coupled oscillators, influences the width and shape of the peaks [4.28].

Another interesting observation is the appearance of weak satellite lines around the main ESR line, visualized in Fig. 4(b) by the resonator transmission amplitude as a

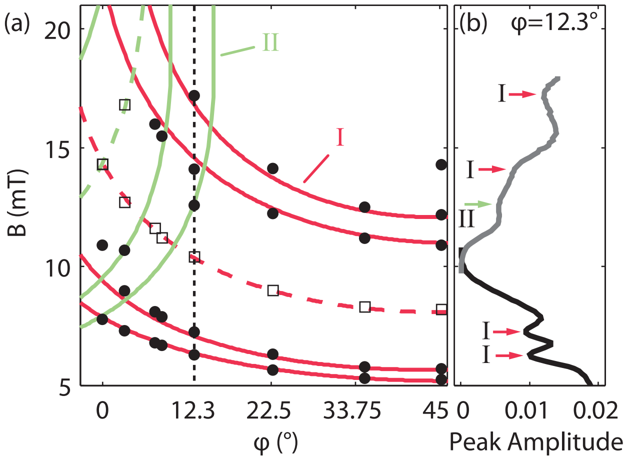

Figure 4.3.: (Color online) (a) Measured (dots) and simulated (solid lines) nearest neighbor ^{13}C satellite lines as a function of the magnetic field angle (colors denote the subensembles I and II). Also shown is the measured (center of the avoided crossing) and theoretical position of the main NV ESR (squares and dashed lines). The dotted line marks the angle at which the data in (b) is taken. (b) Amplitude of the lower (black) and higher (gray) frequency peak of the transmission signal obtained from Lorentzian fits as a function of the magnetic field. Satellite lines due to the hyperfine interaction of nearest neighbor ^{13}C nuclear spins with the electronic NV are visible and indicated by arrows. For $\varphi = 12.3°$ we see the four allowed ESR transitions of subensemble I (red arrow) and one of subensemble II (green arrow).

function of the magnetic field. As previously shown [4.23], the hyperfine interaction of a nearest neighbor ^{13}C nuclear spin with the NV spin leads to an ESR doublet split by 130 MHz in zero field. However, for our geometry and a non-zero magnetic field, the pseudo-nuclear Zeeman effect [4.31] gives rise to two additional transitions, resulting in four allowed ESR lines (selection rules $|\Delta m_S| = 1$, $|\Delta m_I| = 0$). In Fig. 4(a) we show the position of the satellite lines as a function of the magnetic field direction. These findings agree well with the simulation of the full spin Hamiltonian Eq. 4.0.1 when we assume hyperfine coupling parameters $A_{\parallel}/h = 200$ MHz and $A_{\perp}/h = 120$ MHz [4.32]. Since the isotope ^{13}C only appears at its natural abundance of 1.1% in our samples, we estimate the coupling strength of these resonances to be weaker by a factor of $\sqrt{3 \times 1.1/100}$. For this reason we do not observe an avoided crossing for these lines but only a reduction of the transmission amplitude and an increased linewidth. Also note that some remote satellite lines observed are not predicted by the model.

Additionally, we use a cavity readout scheme in the dispersive regime of cavity QED, where $\Delta = |\omega_r - \omega_\pm| \gg \sqrt{N}g$. Here the atomic ensemble can be seen as a refractive medium, lowering the resonator frequency by $\Delta_c \simeq Ng^2/\Delta$ when the ensemble is polarized in the ground state. If we add an additional MW tone $\omega_d = \omega_\pm$, a fraction of the NV ensemble is excited, leading to a positive shift which is plotted in figure 4. In Fig. 4(a) we scan the spectroscopy frequency ω_d across the NV ESR lines and obtain the zero-field splitting parameters of the diamond sample by making use of the aforementioned dispersive interaction. We extract values for the parallel component of the zero-field splitting $D/h = 2.877$ GHz and the transversal component $E/h = 7.7$ MHz from the position of the minimum and the distance of the two peak maxima, respectively. As a fit function we used a simple asymmetric lineshape [4.33]. These values are in accordance with ODMR measurements of the same sample and taking temperature effects into account [4.34].

We also present a relaxation measurement of the spin ensemble after excitation at $\omega_d/2\pi = 2.885$ GHz (see Fig. 4(b)). In this measurement we first excite the NV centers, then wait for a given time after the dispersive tone has been switched off and finally probe the cavity resonance. This sequence is repeated for different waiting times. The resonant cavity probe signal is switched on only in this last part of the measurement sequence. From an exponential fit we determine a relaxation time constant $\tau = 44 \pm 4$ s. This value agrees well with previous T1 measurements of NV centers in diamond at low temperature [4.35, 4.36]. In order to study the influence of the probe signal on the spin relaxation, we excite the NV centers as before and then probe the cavity continuously on resonance. For low probe powers ($\approx 5 \times 10^4$ photons) the obtained time constant $\tau = 45 \pm 4$ s agrees with the previously measured decay time. This shows that the measurement is non-destructive which is due to the fact that the dispersive measurement is a quantum non-demolition measurement at low probe power. However, we note that for higher probe powers the observed time constant substantially decreases and the form of the decay deviates from a simple monoexponential decay.

In conclusion we have shown the strong coupling of an NV spin ensemble to a CPW resonator and its $\sqrt{N}$-scaling with the number of emitters. We determined the spin-lattice relaxation time and ZFS parameters at 60 mK using dispersive measurements, a powerful technique in cavity QED. Furthermore the observed coupling to nuclear spin degrees of freedom in diamond may provide an avenue towards extended storage times and quantum information processing with auxiliary nuclear spins.

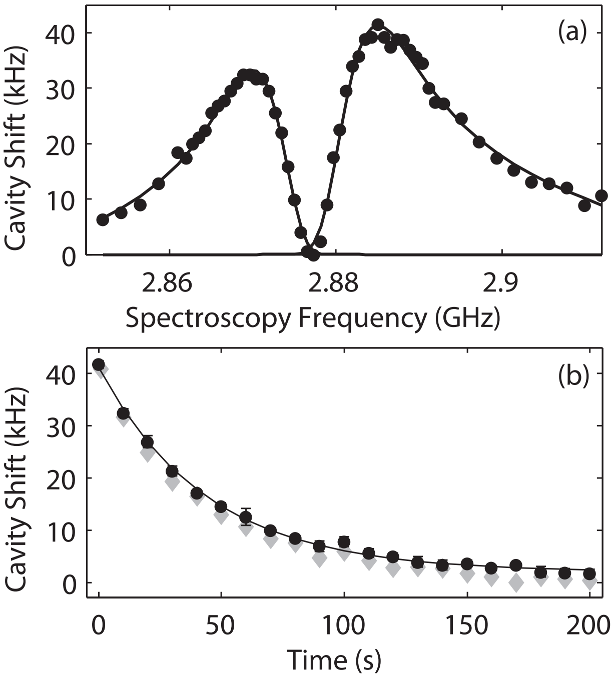

Figure 4.4.: (a) Dispersive resonator shift as a function of the spectroscopy frequency $\omega_d/2\pi$ ($B = 0$ mT). This measurement allows to extract the zero-field splitting parameters $D/h = 2.877$ GHz and $E/h = 7.7$ MHz. (b) NV spin relaxation measured via the resonator shift after the excitation frequency has been switched off ($B = 0$ mT, $\omega_d/2\pi = 2.885$ GHz). Black dots refer to resonator frequency measurements after a given time after switch off ($\tau = 44 \pm 4$ s), diamonds mark measurements with a continuously probed resonator ($\tau = 45 \pm 4$ s) (see text for details). An exponential fit of the black data points is also displayed.

Acknowledgments

This work was supported by the the Austrian FWF through the Wittgenstein Prize and the EU (MI-DAS, AQUTE). R.A., T.N. were supported by CoQuS, C.K. by FunMat and, K.S. the DOC-fFORTE doctoral program. We thank J. Wrachtrup, F. Jelezko, H. Fedder and M. Trupke for helpful discussions.

References for Chapter 4

[4.1] M Wallquist et al. "Hybrid quantum devices and quantum engineering." In: *Physica Scripta* T137 (Dec. 2009), p. 014001. ISSN: 0031-8949. DOI: `10.1088/0031-8949/2009/T137/014001`. URL: `http://iopscience.iop.org/1402-4896/2009/T137/014001/`.

[4.2] J. Verdú et al. "Strong Magnetic Coupling of an Ultracold Gas to a Superconducting Waveguide Cavity." In: *Physical Review Letters* 103.4 (July 2009), p. 043603. DOI: `10.1103/PhysRevLett.103.043603`. URL: `http://link.aps.org/doi/10.1103/PhysRevLett.103.043603`.

[4.3] A. Andre et al. "A coherent all-electrical interface between polar molecules and mesoscopic superconducting resonators." In: *Nat Phys* 2.9 (2006), pp. 636–642. ISSN: 1745-2473. DOI: `10.1038/nphys386`. URL: `http://dx.doi.org/10.1038/nphys386`.

[4.4] P. Rabl et al. "Hybrid Quantum Processors: Molecular Ensembles as Quantum Memory for Solid State Circuits." In: *Physical Review Letters* 97.3 (July 2006), pp. 033003–4. DOI: `10.1103/PhysRevLett.97.033003`. URL: `http://link.aps.org/abstract/PRL/v97/e033003`.

[4.5] J. Twamley and S. D. Barrett. "Superconducting cavity bus for single nitrogen-vacancy defect centers in diamond." In: *Physical Review B* 81.24 (June 2010), p. 241202. DOI: `10.1103/PhysRevB.81.241202`. URL: `http://link.aps.org/doi/10.1103/PhysRevB.81.241202`.

[4.6] D. Marcos et al. "Coupling Nitrogen-Vacancy Centers in Diamond to Superconducting Flux Qubits." In: *Physical Review Letters* 105.21 (Nov. 2010), p. 210501. DOI: `10.1103/PhysRevLett.105.210501`. URL: `http://link.aps.org/doi/10.1103/PhysRevLett.105.210501`.

[4.7] John Clarke and Frank K. Wilhelm. "Superconducting quantum bits." In: *Nature* 453.7198 (June 2008), pp. 1031–1042. ISSN: 0028-0836. DOI: `10.1038/nature07128`. URL: `http://dx.doi.org/10.1038/nature07128`.

[4.8] J. Majer et al. "Coupling superconducting qubits via a cavity bus." In: *Nature* 449.7161 (2007), pp. 443–447. ISSN: 0028-0836. DOI: `10.1038/nature06184`. URL: `http://dx.doi.org/10.1038/nature06184`.

[4.9] Gopalakrishnan Balasubramanian et al. "Ultralong spin coherence time in isotopically engineered diamond." In: *Nat Mater* 8.5 (May 2009), pp. 383–387. ISSN: 1476-1122. DOI: `10.1038/nmat2420`. URL: `http://dx.doi.org/10.1038/nmat2420`.

[4.10] E. Togan et al. “Quantum entanglement between an optical photon and a solid-state spin qubit.” In: *Nature* 466.7307 (2010), pp. 730–734. ISSN: 0028-0836. DOI: `10.1038/nature09256`. URL: `http://dx.doi.org/10.1038/nature09256`.

[4.11] R. H. Dicke. “Coherence in Spontaneous Radiation Processes.” In: *Physical Review* 93.1 (1954), p. 99.

[4.12] Atac Imamoglu. “Cavity QED Based on Collective Magnetic Dipole Coupling: Spin Ensembles as Hybrid Two-Level Systems.” In: *Physical Review Letters* 102.8 (Feb. 2009), p. 083602. DOI: `10.1103/PhysRevLett.102.083602`. URL: `http://link.aps.org/doi/10.1103/PhysRevLett.102.083602`.

[4.13] J. H. Wesenberg et al. “Quantum Computing with an Electron Spin Ensemble.” In: *Physical Review Letters* 103.7 (2009), p. 070502. DOI: `10.1103/PhysRevLett.103.070502`. URL: `http://link.aps.org/doi/10.1103/PhysRevLett.103.070502`.

[4.14] Y. Kubo et al. “Strong Coupling of a Spin Ensemble to a Superconducting Resonator.” In: *Physical Review Letters* 105.14 (2010), p. 140502. DOI: `10.1103/PhysRevLett.105.140502`. URL: `http://link.aps.org/doi/10.1103/PhysRevLett.105.140502`.

[4.15] D. I. Schuster et al. “High-Cooperativity Coupling of Electron-Spin Ensembles to Superconducting Cavities.” In: *Physical Review Letters* 105.14 (2010), p. 140501. DOI: `10.1103/PhysRevLett.105.140501`. URL: `http://link.aps.org/doi/10.1103/PhysRevLett.105.140501`.

[4.16] P. Bushev et al. “Rare earth spin ensemble magnetically coupled to a superconducting resonator.” In: *arXiv:1102.3841* (Feb. 2011). URL: `http://arxiv.org/abs/1102.3841`.

[4.17] I. Chiorescu et al. “Magnetic strong coupling in a spin-photon system and transition to classical regime.” In: *Physical Review B* 82.2 (July 2010), p. 024413. DOI: `10.1103/PhysRevB.82.024413`. URL: `http://link.aps.org/doi/10.1103/PhysRevB.82.024413`.

[4.18] A. L. Alexander et al. “Photon Echoes Produced by Switching Electric Fields.” In: *Physical Review Letters* 96.4 (Feb. 2006), p. 043602. DOI: `10.1103/PhysRevLett.96.043602`. URL: `http://link.aps.org/doi/10.1103/PhysRevLett.96.043602`.

[4.19] B. Kraus et al. “Quantum memory for nonstationary light fields based on controlled reversible inhomogeneous broadening.” In: *Physical Review A* 73.2 (Feb. 2006), p. 020302. DOI: `10.1103/PhysRevA.73.020302`. URL: `http://link.aps.org/doi/10.1103/PhysRevA.73.020302`.

[4.20] Hua Wu et al. “Storage of Multiple Coherent Microwave Excitations in an Electron Spin Ensemble.” In: *Physical Review Letters* 105.14 (2010), p. 140503. DOI: `10.1103/PhysRevLett.105.140503`. URL: `http://link.aps.org/doi/10.1103/PhysRevLett.105.140503`.

[4.21] Y. Mita. “Change of absorption spectra in type-Ib diamond with heavy neutron irradiation.” In: *Physical Review B* 53.17 (1996), p. 11360.

[4.22] JE Healey et al. “Magnetic field tuning of coplanar waveguide resonators.” In: *Applied Physics Letters* 93 (2008), p. 043513.

[4.23] F. Jelezko et al. “Observation of Coherent Oscillations in a Single Electron Spin.” In: *Physical Review Letters* 92.7 (Feb. 2004), p. 076401. DOI: `10.1103/PhysRevLett.92.076401`. URL: `http://link.aps.org/abstract/PRL/v92/e076401`.

[4.24] Stefan Stoll and Arthur Schweiger. “EasySpin, a comprehensive software package for spectral simulation and analysis in EPR.” In: *Journal of Magnetic Resonance* 178.1 (Jan. 2006), pp. 42–55. ISSN: 1090-7807. DOI: `10.1016/j.jmr.2005.08.013`. URL: `http://www.sciencedirect.com/science/article/B6WJX-4H68T8N-2/2/8530290c49669b6a28a576f4630193eb`.

[4.25] F. Maier et al. “Origin of Surface Conductivity in Diamond.” In: *Physical Review Letters* 85.16 (Oct. 2000), p. 3472. DOI: `10.1103/PhysRevLett.85.3472`. URL: `http://link.aps.org/doi/10.1103/PhysRevLett.85.3472`.

[4.26] J. Gripp et al. “Anharmonicity of the vacuum Rabi peaks in a many-atom system.” In: *Phys. Rev. A* 54 (5 Nov. 1996), R3746–R3749. DOI: `10.1103/PhysRevA.54.R3746`. URL: `http://link.aps.org/doi/10.1103/PhysRevA.54.R3746`.

[4.27] I. Diniz et al. “Strongly coupling a cavity to inhomogeneous ensembles of emitters : potential for long lived solid-state quantum memories.” In: *arXiv:1101.1842* (Jan. 2011). URL: `http://arxiv.org/abs/1101.1842`.

[4.28] Z. Kurucz, J. H Wesenberg, and K. Mø lmer. “Spectroscopic properties of inhomogeneously broadened spin ensembles in a cavity.” In: *1101.4828* (Jan. 2011). URL: `http://arxiv.org/abs/1101.4828`.

[4.29] Kathrin Henschel et al. “Cavity QED with an ultracold ensemble on a chip: Prospects for strong magnetic coupling at finite temperatures.” In: *Physical Review A* 82.3 (2010), p. 033810. DOI: `10.1103/PhysRevA.82.033810`. URL: `http://link.aps.org/doi/10.1103/PhysRevA.82.033810`.

[4.30] B. M. Garraway. “Nonperturbative decay of an atomic system in a cavity.” In: *Phys. Rev. A* 55 (3 Mar. 1997), pp. 2290–2303. DOI: `10.1103/PhysRevA.55.2290`. URL: `http://link.aps.org/doi/10.1103/PhysRevA.55.2290`.

[4.31] B. Bleaney. In: *Hyperfine Interactions.* Ed. by Arthur J. Freeman and Richard B. Frankel. Academic Press, 1967.

[4.32] S. Felton et al. "Hyperfine interaction in the ground state of the negatively charged nitrogen vacancy center in diamond." In: *Physical Review B* 79.7 (Feb. 2009), p. 075203. DOI: `10.1103/PhysRevB.79.075203`. URL: `http://link.aps.org/doi/10.1103/PhysRevB.79.075203`.

[4.33] A.L. Stancik and E.B. Brauns. "A simple asymmetric lineshape for fitting infrared absorption spectra." In: *Vibrational Spectroscopy* 47.1 (2008), pp. 66–69.

[4.34] V. M. Acosta et al. "Diamonds with a high density of nitrogen-vacancy centers for magnetometry applications." In: *Physical Review B* 80.11 (2009), p. 115202. DOI: `10.1103/PhysRevB.80.115202`. URL: `http://link.aps.org/doi/10.1103/PhysRevB.80.115202`.

[4.35] J. Harrison, M.J. Sellars, and N.B. Manson. "Measurement of the optically induced spin polarisation of N-V centres in diamond." In: *Diamond and Related Materials* 15.4-8 (Apr. 2006), pp. 586–588. ISSN: 0925-9635. DOI: `10.1016/j.diamond.2005.12.027`. URL: `http://www.sciencedirect.com/science/article/B6TWV-4JCBKN5-2/2/452735991009a5d38f70257fba53109c`.

[4.36] A. Jarmola, V.M. Acosta, and D. Budker. In: (to be published).

5. Publication

PHYSICAL REVIEW A (2012)

Strong magnetic coupling of an inhomogeneous nitrogen-vancancy ensemble to a cavity[†]

Kathrin Sandner[1], Helmut Ritsch[1], Robert Amsüss[2], Christian Koller[2], Tobias Nöbauer[2], Stefan Putz[2], Jörg Schmiedmajer[2], Johannes Majer[2]

[1] *Institute for Theoretical Physics, University of Innsbruck*
Technikerstr. 25, 6020 Innsbruck, Austria
[2] *Atominstitut, TU-Wien, Stadionallee 2,*
1020 Vienna, Austria

We study experimentally and theoretically a dense ensemble of negatively charged nitrogen-vacancy centers in diamond coupled to a high-Q superconducting coplanar waveguide cavity mode at low temperature. The nitrogen-vacancy centers are modeled as effective spin-one defects with inhomogeneous frequency distribution. For a large enough ensemble the effective magnetic coupling of the collective spin dominates the mode losses and inhomogeneous broadening of the ensemble and the system exhibits well-resolved normal-mode splitting in probe transmission spectra. We use several theoretical approaches to model the probe spectra and the number and frequency distribution of the spins. This analysis reveals an only slowly temperature-dependent q-Gaussian energy distribution of the defects with a yet unexplained decrease of effectively coupled spins at very low temperatures below 100 mK. Based on the system parameters we predict the possibility to implement an extremely stable maser by adding an external pump to the system.

PACS numbers: 42.50.Pq,42.50.Ct,61.72.jn,03.67.-a

[†] The author of the present thesis performed all of the calculations in this publication, except those for the tuning of the NV ensemble in the magnetic field in Fig. 5.1(b) which was done by Robert Amsüss.

5.1. Introduction

Systems of spin ensembles coupled to a cavity mode are considered a promising physical realization for processing and storage of quantum information [5.1], ultra-sensitive high-resolution magnetometers [5.2], or localized field probes. Collective magnetic coupling of a large ensemble to the field mode allows us to reach the strong-coupling regime, even if a single particle is hardly coupled. Implementations based on superconducting coplanar waveguide (CPW) resonators provide an interface of the spin ensemble with processing units for superconducting qubits. Here the spins can serve as a quantum memory or as a bridge to optical readout and communication [5.3].

Different types of ensembles were proposed for this setup, ranging from clouds of ultracold atoms [5.3] over polar molecules [5.4] to solid-state systems like rare-earth spin ensembles [5.5] or color centers in diamond [5.6, 5.7]. Here we focus on the negatively charged nitrogen-vacancy (NV) defects in diamond . Those are naturally present in diamond but can also be readily engineered with very high densities, still maintaining long lifetimes and slow dephasing in particular at low temperatures of $T < 1$ K. In the optical domain, they are extremely stable and have been very well studied for many years [5.8].

The magnetic properties of the relevant defect states can be conveniently modeled by effective independent spin-one particles, where the effective local interaction of the electrons within the defect shifts the ($m_S = \pm 1$) states with respect to the $m_S = 0$ state [5.9]. On the one hand, this coupling provides the desired energy gap in the 3 GHz regime, but, on the other hand, as a consequence of local variations of the crystal field, this shift exhibits a frequency distribution leading to an inhomogeneous broadening of the ensemble. The inhomogeneities are thought to be predominantly caused by crystal strain and excess nitrogen, which is not paired with a neighboring vacancy [5.10].

While, for a perfectly monochromatic ensemble of N particles in a cavity, strong coupling simply requires an effective coupling $g_{\text{single}}\sqrt{N}$ larger than the cavity and spin decay rates, not only the width, but also the details of the inhomogeneous distribution are known to strongly influence the dynamic properties of the real world system [5.11–5.13]. In particular, Gaussian and Lorentzian distributions of equal half widths, lead to different widths and magnitudes of the vacuum Rabi splitting. Only above a critical coupling strength the rephasing via common coupling to the cavity mode will prevent dephasing of the collective excitation and lead to a well resolved vacuum Rabi splitting.

In our theoretical studies we use different approximation levels to analyze the central physical effects present in the coupled system of cavity and inhomogeneously broadened ensemble, as they are observed in the measurements. While many qualitative features can be readily understood from a simple, coupled damped oscillator model with an effective linewidth, a detailed understanding of the observed frequency shifts and coupling strengths in the experiments requires more sophisticated modeling of the energy distributions and dephasing mechanisms. In particular the observed temperature dependence relies on a finite temperature master-equation treatment of a collective spin with proper dephasing terms. This is compared to the experimental values of up to ($N \approx 10^{12}$) particles as presented already in [5.7]. We focus on the interplay between the cavity mode and the ensemble and in particular on the role of the frequency distribution of the ensemble. This analysis is also applicable to systems other than NV ensembles. Though the detailed microscopic mechanisms within the NV ensemble that cause the inhomogeneous frequency distribution are of considerable relevance, our central point of interest is the effect of the inhomogeneity rather than its origin. A thorough investigation of the broadening mechanisms is beyond the scope of this manuscript.

The paper is organized as follows. The general properties of the system are introduced in Sec. 5.2. A first approximative treatment using coupled harmonic oscillators is shown in Sec. 5.6. In Sec. 5.7 we incorporate the inhomogeneous frequency distribution of the NVs via an extra decay of the polarization of the ensemble. In this context we also analyze the effects of thermal excitations in the spin ensemble and in the cavity. Finally, in Sec. 5.8 we interpret our measurements using the resolvent formalism in order to extract the exact form of the inhomogeneity [5.13]. The prospect of implementing a narrow bandwidth transmission line micro-maser using an inhomogeneously broadened ensemble is discussed in Sec. 5.9.

5.2. General system properties and experimental implementation

The ground state of the NV center is a spin triplet ($S = 1$), where the $m_S = \pm 1$ states are split from the $m_S = 0$ state by about 2.88 GHz at zero magnetic field [5.10]. In addition the degeneracy between the $m_S = \pm 1$ states is lifted due to the broken C_{3v} symmetry. Applying a homogeneous magnetic field enables Zeeman tuning of the $m_S = \pm 1$ states, so that the $m_S = 0 \to \pm 1$ transitions can be tuned selectively into resonance with the CPW cavity.

Note that here the Zeeman tuning is also varying with the NV centers orientation relative to the applied field direction. In NV center ensembles all the four symmetry allowed orientations of the NV main axis are found and in general each orientation will enclose a different angle with the magnetic field and will be shifted by a different amount.

However, if the magnetic field direction is oriented within the (001) plane of the diamond, always two of four orientations exhibit the same angle with the field and at special angles all four are tuned by the same amount.

In general we therefore have to distinguish between the $m_S^{\mathrm{I,II}} = \pm 1$ states of subensemble I and II. The Hamiltonian for one NV subensemble can be written as

$$\mathrm{H}_{\mathrm{NV}} = \tilde{g}\mu_B \mathbf{B} \cdot \mathbf{S} + DS_z^2 + E(S_x^2 - S_y^2), \tag{5.2.1}$$

where the first term describes the Zeeman effect with $\tilde{g} = 2$ for an NV center and μ_B is the Bohr magneton. The second term denotes the zero-field splitting with $D = 2.88$ GHz and typical strain-induced E parameters of several MHz. The presence of non-zero E parameters in large NV ensembles causes a mixing of the pure Zeeman states for low magnetic field values which are denoted as $|0, \pm\rangle$. As the magnetic-field amplitude is increased, the eigenstates are again well approximated by pure Zeeman states.

The transition frequencies $\omega_\pm^{\mathrm{I,II}}$ between the eigenstates $|0\rangle_{\mathrm{I,II}}$ and $|\pm\rangle_{\mathrm{I,II}}$ are depicted in Fig. 5.1(b).

5.3. Theoretical model

Assuming that only the transition $|0\rangle_{\mathrm{I}} \rightarrow |-\rangle_{\mathrm{I}}$ with frequency ω_-^{I} is in or close to resonance with the cavity mode, we can reduce the description of a single NV to a two-level system. The effects caused by the presence of the far detuned $|+\rangle_{\mathrm{I}}$ state can be included in a constant effective frequency shift as addressed in Sec. 5.6. We thus approximate the composed system of cavity and ensemble with the Tavis-Cummings Hamiltonian

$$\mathrm{H}_{\mathrm{TC}} = \omega_c a_c^\dagger a_c + \frac{1}{2}\sum_j^N \omega_j \sigma_j^z + \sum_j^N \left(g_j \sigma_j^+ a_c + \mathrm{H.c.} \right) \;, \tag{5.3.1}$$

where $\hbar = 1$. The first two terms describe the unperturbed energies of the cavity, with frequency ω_c and creation operator $a_c^\dagger$, and of the N ensemble spins using the usual Pauli spin operators $\left(\left[\sigma_i^+, \sigma_j^-\right] = \sigma_i^z \delta_{ij}\right)$. Each spin can have a different frequency ω_j which is statistically spread around the center frequency ω_-^{I}. The third term describes the coupling to the cavity with individual strength g_j. Assuming that the ensemble spins are confined to a volume that is small compared to the wavelength, the ensemble will interact collectively with the mode. In the case of few excitations, the ensemble behaves like a harmonic oscillator which couples to the mode with the collective coupling strength Ω. The collective coupling strength is given by $\Omega = \sqrt{\sum_j^N |g_j|^2}$ which for identical $g_j = g_{\text{single}} = g$ gives $\Omega = g\sqrt{N}$. The effects of unequal coupling of the spins are addressed in [5.14]. To include the probe field of the cavity we add another term $\mathrm{H}_p = \mathrm{i}\left(\eta a_c^\dagger \mathrm{e}^{-\mathrm{i}\omega_p t} - \eta^* a_c \mathrm{e}^{\mathrm{i}\omega_p t}\right)$, to Eq. (5.3.1).

Effects of the coupling to a finite temperature bath are analyzed in Sec. 5.7, where we study the master equation of the ensemble-cavity system.

For an ensemble with identical frequencies and coupling strengths we find that we can reach the regime of coherent oscillations between the cavity and the ensemble spins if the collective coupling Ω dominates the linewidth of the cavity κ and the decay rate of the single spin γ_{hom}. This is commonly known as strong-coupling regime. In the case of an ensemble with inhomogeneous frequency distribution it is not immediately clear under which conditions we can observe the avoided crossing. Here we address the influence of the width and form of the inhomogeneous frequency distribution on the avoided crossing.

5.4. Experimental setup and parameters

The experimental set-up has been described already in detail in [5.7] and is explained here only in brevity in the following. The heart of the experiment is a $\lambda/2$ superconducting coplanar waveguide (CPW) resonator with a center frequency of 2.7 GHz that is cooled down to 20 mK in a dilution refrigerator. In order to couple NV defect centers to the microwave field in the cavity, a (001)-cut single-crystal diamond is placed in the middle of the resonator, where the oscillating magnetic field exhibits an antinode. A meander geometry of the resonator ensures that a large fraction of the magnetic mode volume is covered by spins. The high-pressure high-temperature diamond chosen in this setup contains an NV concentration of about 6 ppm, which corresponds to an average separation of about 10 nm.

A two-axis Helmholtz coil configuration creates a homogeneous static magnetic field oriented with an arbitrary direction within the (001) plane of the diamond, which is at the same time parallel to the resonator chip surface. Since perpendicular magnetic field components with respect to the resonator surface would shift the resonance frequency of the cavity, great care was taken during the alignment of the set-up. With the diamond on top of the chip the cavity quality factor is $Q = 3200$.

In a typical experiment, we first set the magnetic field direction and amplitude and then measure the microwave transmission through the cavity with a vector network analyzer.

5.5. Cavity transmission spectra for inhomogeneous ensembles

As a generic experiment to test and characterize the system properties we analyze the weak-field probe transmission spectrum through the resonator in the weak-field limit, where the number of excitations is negligible compared to the ensemble size. Hence, at least at low temperatures, we can largely ignore saturation effects and apply various simplified theoretical descriptions to extract the central system parameters. In fact, as we deal with more than $N > 10^{11}$ spins in a transition frequency range of about 10^7 Hz, we have several thousand spins per Hz frequency range and up to a million spins within the homogeneous width of at least several kHz. Hence theoretical modelling as a collection of effective oscillators should provide an excellent model basis. This has to be taken with care at higher temperatures, $k_B T \approx \hbar\omega_c$, when we have a significant fraction of the particles excited.

5.6. Coupled collective oscillator approximation

A photon that enters the cavity will be absorbed into a symmetric excitation of the ensemble spins with a weight given by the individual coupling strength. Subsequently the broad distribution of the spin frequencies induces a relative dephasing of this excitation so that the backcoupling to the cavity mode is suppressed. As spontaneous decay ($T_1 \approx 44$ s) is negligibly slow [5.7], the decay rate of the polarization of the ensemble is just proportional to this dephasing and thus the inhomogeneous width of the spins.

As the number of photons entering the ensemble is very small compared to N in a first model, we simply approximate the ensemble as a harmonic oscillator with frequency $\omega_{a1} = \omega_-^{\mathrm{I}}$ and an effective large width γ that mimics the inhomogeneity. The ensemble oscillator is coupled to the cavity with frequency ω_c and decay rate κ.

This very simplified model already allows us to study the coupling dynamics of the collective energy levels of the broadened ensemble and the cavity mode, and in particular the avoided crossing of the energy levels, when the relative energies are varied.

To keep the model as simple as possible but still grasping the essential properties, the presence of the other offresonant spin ensembles at ω_+^{I}, ω_-^{II}, and ω_+^{II} is modelled by additional oscillators with frequency ω_{aj}, $(j = 2, 3, 4)$ and equal decay rate γ.

For a small probe field injected into the cavity with the frequency ω_p the corresponding equations in a frame rotating with ω_p then read:

$$\frac{\mathrm{d}}{\mathrm{d}t}\langle a_c\rangle = -\left(\kappa + \mathrm{i}\Delta_c\right)\langle a_c\rangle - \mathrm{i}g\sum_{j=1}^{4} N_j \left\langle \sigma_j^-\right\rangle + \eta \tag{5.6.1}$$

$$\frac{\mathrm{d}}{\mathrm{d}t}\left\langle \sigma_j^-\right\rangle = -\left(\frac{\gamma}{2} + \mathrm{i}\Delta_{aj}\right)\left\langle \sigma_j^-\right\rangle - \mathrm{i}g\langle a_c\rangle \ , \tag{5.6.2}$$

with probe amplitude η, $\Delta_c = \omega_c - \omega_p$ and $\Delta_{aj} = \omega_{aj} - \omega_p$. From Eqs. (5.6.1) and (5.6.2) we can calculate the steady state field in the cavity $\langle a_c\rangle_{\mathrm{st}}$, which can be written as

$$\langle a_c\rangle_{\mathrm{st}} = \frac{\eta}{\kappa + \Gamma_a + \mathrm{i}\left(\Delta_c - U_a\right) + \frac{g^2 N_1}{\gamma/2 + \mathrm{i}\Delta_{a1}}} \ , \tag{5.6.3}$$

where

$$\Gamma_a = \sum_{j=2}^{4} \frac{g^2 N_j \gamma/2}{\left(\gamma/2\right)^2 + \Delta_{aj}^2} \quad \text{and} \quad U_a = \sum_{j=2}^{4} \frac{g^2 N_j \Delta_{aj}}{\left(\gamma/2\right)^2 + \Delta_{aj}^2} \ . \tag{5.6.4}$$

In the absence of the offresonant levels ($N_2 = N_3 = N_4 = 0$) we recover the situation, where for $\omega_{a1} = \omega_c$ and $g\sqrt{N_1} > (\gamma/2 - \kappa)/2$ we find two normal modes split by $2\sqrt{g^2 N_1 - (\gamma/2 - \kappa)^2/4}$. The offresonant transitions make the situation more com-

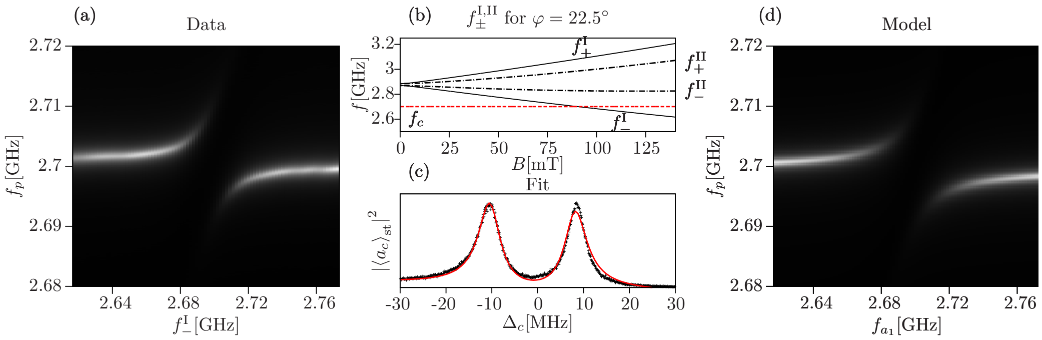

Figure 5.1.: (a) (Color online) Measured transmission as a function of $f_-^{\mathrm{I}} = \omega_-^{\mathrm{I}}/(2\pi)$ tuned by the magnetic field and pump frequency $f_p = \omega_p/(2\pi)$. (b) Transition frequencies $f_\pm^{\mathrm{I,II}} = \omega_\pm^{\mathrm{I,II}}/(2\pi)$ as a function of the magnetic field for a field angle of $\varphi = 22.5^\circ$. The frequency of the cavity $f_c = \omega_c/(2\pi)$ is denoted by the (red) dashed line. (c) Fit of $\left|\langle a_c \rangle_{\mathrm{st}}\right|^2$ to the transmitted signal close to the resonance. We obtain the decay rate $\gamma = 10.92$ MHz. (d) $\left|\langle a_c \rangle_{\mathrm{st}}\right|^2$ as a function of f_{a_1} and f_p incorporating the parameters obtained from the fit.

plex. As it can be seen in Eq. (5.6.3), they induce a shift U_a of the cavity frequency and increase the decay rate of the cavity by Γ_a. Both, shift and additional decay rate, depend on the probe frequency ω_p. For the parameters in our measurement we find that Γ_a is negligible compared to κ. We further approximate U_a by setting $\omega_p = \omega_c$ (as the scan range of ω_p around ω_c is small compared to ω_{aj} $(j = 2, 3, 4)$). We obtain the model of two coupled oscillators, where one of them has been shifted by the offresonant transitions. As a function of ω_p and ω_{a1} (tuned by the magnetic field), $|\langle a_c \rangle_{\mathrm{st}}|^2$ shows an avoided crossing. Although the offresonant transitions are shifted by the magnetic field as well, the effect in U_a is negligibly small, so that we assume that U_a is constant.

We show the measured signal at the avoided crossing in Fig. 5.1(a). By fitting $|\langle a_c \rangle_{\mathrm{st}}|^2$ to the normal mode splitting we can deduce the inhomogeneous width γ and the effective coupling $g\sqrt{N}$. The Q factor of our cavity corresponds to $\kappa/(2\pi) = 0.4$ MHz, then 2κ is the full width at half maximum (FWHM) of the cavity resonance. An exemplary fit result is shown in Fig. 5.1(c). We have included a linear term in the fit to account for a background in the data. In Fig. 5.1(d) we plot $|\langle a_c \rangle_{\mathrm{st}}|^2$ using the obtained parameters.

From the fit we deduce a decay rate $\gamma = 10.92$ MHz of the ensemble oscillator and an effective coupling of $g\sqrt{N} = 9.51$ MHz. To demonstrate the effect of the ensemble oscillator width γ on the normal mode splitting, we plot $|\langle a_c \rangle_{\mathrm{st}}|^2$ for $\omega_c - U_a = \omega_{a1}$

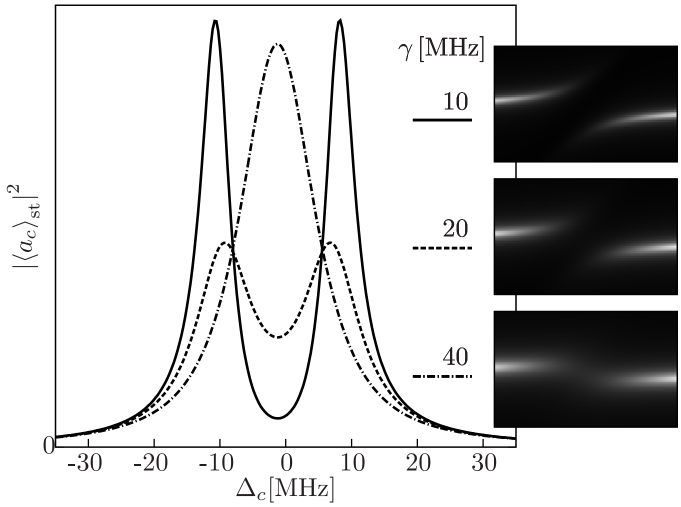

Figure 5.2.: Simulation of the normal mode splitting at resonance ($\omega_c - U_a = \omega_{a1}$) for different values of γ. Finally for large values of γ the doublet is not resolved any more and the avoided crossing (sketched on the right) becomes blurred.

and different values of γ in Fig. 5.2.

Treating the ensemble as a broad harmonic oscillator with decay rate γ corresponds to the assumption that the frequency distribution of the real ensemble is a Lorentzian distribution, given that all spins couple with equal strength [5.13].

5.7. Polarization decay and collective coupling at finite temperature

Despite the fact that cooling to very low temperatures is possible in the experiments, it is still important and instructive to study the role of thermal excitations in the system. In contrast to previous models based on virtually zero T atomic ensembles, the NV centers are in thermal contact with the chip at small but finite T. We will now investigate how sensitive the system reacts on thermal fluctuations.

At this point we include any shifts caused by the off-resonant ensembles in an effective detuning and concentrate on the collective coupling between the cavity at ω_c and the near resonant ensemble centered around ω_-^{I}. For simplicity we assume equal coupling g for all spins to get

$$\tilde{\mathrm{H}}_{\mathrm{TC}} = \omega_c a_c^\dagger a_c + \frac{1}{2}\omega_-^{\mathrm{I}} \sum_j^N \sigma_j^z + g \sum_j^N \left(\sigma_j^+ a_c + \mathrm{H.c.}\right) \ . \tag{5.7.1}$$

To include thermal excitations of the mode and the ensemble we have to add standard Liouvillian terms to the dynamics and study the corresponding master equation of the reduced cavity-ensemble system [5.15], where the inhomogeneous width of the ensemble is still simply approximated by an effective dephasing term γ_p for the polarization. In this model decay γ_{hom} and dephasing γ_p are described by separate quantities, which already should improve the model. The master equation reads

$$\frac{\mathrm{d}}{\mathrm{d}t}\rho = \frac{1}{\mathrm{i}}\left[\tilde{\mathrm{H}}_{\mathrm{TC}} + \mathrm{H}_p, \rho\right] + \mathcal{L}\left[\rho\right] \ , \tag{5.7.2}$$

where

$$\begin{aligned}\mathcal{L}\left[\rho\right] &= \kappa\left(\bar{n}\left(T,\omega_c\right)+1\right)\left(2a_c\rho a_c^\dagger - a_c^\dagger a_c\rho - \rho a_c^\dagger a_c\right)\\ &+ \kappa\bar{n}\left(T,\omega_c\right)\left(2a_c^\dagger\rho a_c - a_c a_c^\dagger\rho - \rho a_c a_c^\dagger\right)\\ &+ \frac{\gamma_{\mathrm{hom}}}{2}\left(\bar{n}\left(T,\omega_-^{\mathrm{I}}\right)+1\right)\sum_{j=1}^N\left(2\sigma_j^-\rho\sigma_j^+ - \sigma_j^+\sigma_j^-\rho - \rho\sigma_j^+\sigma_j^-\right)\\ &+ \frac{\gamma_{\mathrm{hom}}}{2}\bar{n}\left(T,\omega_-^{\mathrm{I}}\right)\sum_{j=1}^N\left(2\sigma_j^+\rho\sigma_j^- - \sigma_j^-\sigma_j^+\rho - \rho\sigma_j^-\sigma_j^+\right)\\ &+ \frac{\gamma_p}{2}\sum_{j=1}^N\left(\sigma_j^z\rho\sigma_j^z - \rho\right) \ .\end{aligned} \tag{5.7.3}$$

The first two lines of Eq. (5.7.3) describe the coupling of the cavity to the bath, while the next two lines include the coupling of the ensemble to the bath. The number of thermal excitations at temperature T and frequency ω is denoted by $\bar{n}\left(T,\omega\right)$. The term in the last line introduces nonradiative dephasing at a rate γ_p of the spins and thereby models the inhomogeneity.

Based on the master equation we can derive a hierarchic set of equations for various system expectation values starting with

$$\begin{aligned}\frac{\mathrm{d}}{\mathrm{d}t}\left\langle a_c\right\rangle &= \mathrm{Tr}\{a_c\frac{\mathrm{d}}{\mathrm{d}t}\rho\}\\ &= -\left(\kappa + \mathrm{i}\Delta_c\right)\left\langle a_c\right\rangle - \mathrm{i}gN\left\langle\sigma_i^-\right\rangle + \eta \ ,\end{aligned} \tag{5.7.4}$$

$$\begin{aligned}\frac{\mathrm{d}}{\mathrm{d}t}\left\langle\sigma_i^-\right\rangle &= -\left(\frac{\gamma_{\mathrm{hom}}}{2}+\gamma_{\mathrm{hom}}\bar{n}\left(T,\omega_-^{\mathrm{I}}\right)+\gamma_p+\mathrm{i}\Delta_-^{\mathrm{I}}\right)\left\langle\sigma_i^-\right\rangle\\&\quad+\mathrm{i}g\left\langle\sigma_i^z a_c\right\rangle\ , &(5.7.5)\\\frac{\mathrm{d}}{\mathrm{d}t}\left\langle\sigma_i^z\right\rangle &= -\mathrm{i}2g\left(\left\langle\sigma_i^+a_c\right\rangle-\left\langle\sigma_i^-a_c^\dagger\right\rangle\right)-\gamma_{\mathrm{hom}}\left(\left\langle\sigma_i^z\right\rangle+1\right)\\&\quad-2\gamma_{\mathrm{hom}}\bar{n}\left(T,\omega_-^{\mathrm{I}}\right)\left\langle\sigma_i^z\right\rangle\ , &(5.7.6)\end{aligned}$$

which also includes equations for $\left\langle a_c\sigma_i^+\right\rangle$, $\left\langle a_c\sigma_i^z\right\rangle$, $\left\langle\sigma_i^+\sigma_j^-\right\rangle$, $\left\langle a_c^\dagger a_c\right\rangle$, $\left\langle a_c\sigma_i^-\right\rangle$, $\left\langle a_c^\dagger a_c^\dagger\right\rangle$, $\left\langle\sigma_i^-\sigma_j^-\right\rangle$, $\left\langle\sigma_i^z\sigma_j^+\right\rangle$, $\left\langle\sigma_i^z\sigma_j^z\right\rangle$, and $\left\langle a_c^\dagger a_c\sigma_i^z\right\rangle$. In order to truncate the system higher-order terms in the equations are expanded in a well defined way [5.16], then higher-order cumulants are neglected [5.17, 5.18]. The equations again are written in a frame rotating with the cavity probe frequency ω_p. Despite the inhomogeneous broadening, which is included by the nonradiative dephasing of the spins, we assume that all spins are equal so that we only have to include the equations for one spin i and pairs i, j [5.17]. This set of equations can be integrated numerically to study the dynamics of the coupled system. We note that when we fix $\left\langle\sigma_i^z\right\rangle = -1$ we immediately arrive at the model discussed in Sec. 5.6 with $\gamma = \gamma_{\mathrm{hom}} + 2\gamma_p$.

In our experiment we measure the avoided crossing for different temperatures of the environment and compare it to the results of our model. First we note that the steady state of the inversion as a function of the temperature $\left\langle\sigma_i^z(T)\right\rangle_{\mathrm{st}}$ can be written as [5.5]

$$\begin{aligned}\left\langle\sigma_i^z(T)\right\rangle_{\mathrm{st}} &= \frac{1}{1+2\bar{n}\left(T,\omega_-^{\mathrm{I}}\right)}\left\langle\sigma_i^z(T=0)\right\rangle_{\mathrm{st}}\\&= \tanh\left(\frac{\hbar\omega_i}{2k_BT}\right)\left\langle\sigma_i^z(T=0)\right\rangle_{\mathrm{st}}\ . &(5.7.7)\end{aligned}$$

For higher temperatures $\left\langle\sigma_i^z(T)\right\rangle_{\mathrm{st}}$ is reduced and therefore so are the effective number of NVs that take part in the dynamics. In the model equations this is represented by the last term in Eq.(5.7.5) for the polarization involving $\left\langle a_c\sigma_i^z\right\rangle$, which leads to a cutoff for the coupling at higher T. As a zero-field approximation we thus write

$$\Omega(T) = g\sqrt{N\tanh\left(\frac{\hbar\omega_-^{\mathrm{I}}}{2k_BT}\right)}\ , \tag{5.7.8}$$

where we replaced ω_i by the center frequency ω_-^{I}. Equation (5.7.8) should give an approximate description of the reduction of the Rabi splitting with increasing temperature.

This treatment however neglects the presence of the $m_S = +1$ state which will also be populated with increasing T. Including this level and assuming $\bar{n}\left(T, \omega_+^{\mathrm{I}}\right) \approx \bar{n}\left(T, \omega_-^{\mathrm{I}}\right)$ we find the population difference between the $m_S = 0$ and -1 state to be

$$\frac{N_{-1}(T)}{N} - \frac{N_0(T)}{N} = -\frac{1}{1 + 3\bar{n}\left(T, \omega_-^{\mathrm{I}}\right)} \ . \tag{5.7.9}$$

This suggests

$$\tilde{\Omega}(T) = g\sqrt{\frac{N}{1 + 3\bar{n}\left(T, \omega_-^{\mathrm{I}}\right)}} \tag{5.7.10}$$

to be a better description for the temperature dependence of the coupling.

In a second step we integrate the whole hierarchic set of equations numerically for $\omega_c = \omega_-^{\mathrm{I}}$ and varying pump frequency ω_p. From $|\langle a_c \rangle_{\mathrm{st}}|^2(\omega)$ we determine the Rabi splitting for different temperatures, from which we obtain the collective coupling. This can be compared to our measurements and the approximations in Eqs. (5.7.8) and (5.7.10).

In Fig. 5.3(a) we show that the measured coupling strength is in disagreement with the Eq. (5.7.8), which is most significant for very low temperatures. Both functions Eqs. (5.7.8) (5.7.10) fail to capture the behavior for low temperatures. The disagreement is even more pronounced as we include the effect of the $m_S = +1$ state. So far we have found no definite explanation for the disagreement. However, one possible explanation would be that for low temperatures not all defects are “active“. As temperature increases, more NVs become available but at the same time the number of NVs taking part in the dynamics is proportional to $\tanh\left(\hbar\omega_-^{\mathrm{I}}/(2k_B T)\right)$.

The collective coupling strength determined from the numerical integration of the coupled equations, shown in Fig. 5.3(b), exactly follows Eq. (5.7.8). This shows that the assumption $\Omega(T) \propto \langle \sigma_i^z(T) \rangle_{\mathrm{st}}$ is reasonable. However, the almost constant value of the coupling strength $\Omega(T)$ found in the experimental data for very low T cannot be explained in the above theoretical model. Interestingly the same behavior is also found in measurements of the dispersive shift of the cavity mode as a function of temperature by the offresonant spin ensemble at zero magnetic field. As possible explanations one might think of a reduced thermal excitation probability due to spin-spin coupling or an effective reduction of active NV centers close to zero temperature.

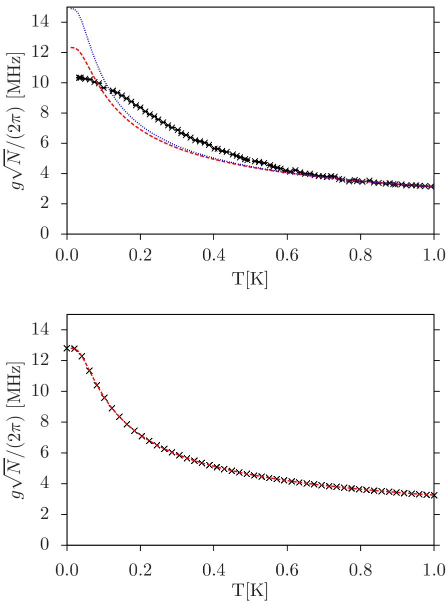

Figure 5.3.: (Color online) (a) Collective coupling strength obtained from our measurements for different temperatures (black markers) and $\Omega(T) = a_0 \left[\tanh\left(\hbar\omega_-^{\mathrm{I}}/(2k_BT)\right)\right]^{1/2}$ (red dashed line), where a_0 was chosen to match the high temperature behavior. Including the $m_S = +1$ state via Eq. (5.7.10) gives the result denoted by the blue dotted line. (b) Collective coupling strength determined from the results of the numerical integration of the coupled equations with $g\sqrt{N} = a_0$ (a_0 determined from (a), black markers) and $\Omega(T)$ (red dashed line).

5.8. Detailed modeling and reconstruction of inhomogeneous distributions

The simplified model descriptions discussed above in Secs. 5.6 and 5.7 provided for an analytically tractable and qualitatively correct description of the effect of an inhomogeneous broadening of the ensemble. This also allows us to get a fairly good estimate for the total width of the frequency distribution of the ensemble. However, such an effective width model inherently is connected to the assumption of a Lorentzian shape of the ensemble frequency distribution. In actual crystals such an assumption is not obvious and other distributions of local-field variations and strain distributions are possible as well.

To obtain more accurate information about the distribution we will now use an improved model based on the resolvent formalism to treat the coupling between a central oscillator (the mode) and the spin degrees of freedom [5.13, 5.19]. Here each frequency class of spins is treated individually. For low temperatures virtually all spins are in the $m_S = 0$ state, i.e., the lower state of our effective two-level system, and their excitation properties can be approximated by a frequency distributed set of oscillators (the Holstein-Primakoff approximation).

We define creation and annihilation operators for the corresponding ensemble oscillators representing a subclass of two-level systems with equal frequency via

$$\sigma_j^z = -1 + 2a_j^\dagger a_j \quad \text{and} \quad \sigma_j^+ = a_j^\dagger \sqrt{1 - a_j^\dagger a_j} \approx a_j^\dagger \ . \tag{5.8.1}$$

The approximation in Eq. (5.8.1) is justified as long as the number of excitations in each ensemble is much smaller than the number of spins in this energy region. In our experimental setup this is very well justified and we thus obtain the unperturbed part of the Hamiltonian as

$$\mathrm{H}_0' = \omega_c a_c^\dagger a_c + \sum_j^N \omega_j a_j^\dagger a_j \ , \tag{5.8.2}$$

and the interaction term

$$\mathrm{V}' = \sum_j^N \left(g_j a_j^\dagger a_c + g_j^* a_j a_c^\dagger \right) \ , \tag{5.8.3}$$

which constitute $\mathrm{H}' = \mathrm{H}_0' + \mathrm{V}'$. In this section we account for the decay of cavity excitations and the spontaneous decay of the spins by introducing nonzero imaginary parts of the corresponding transition frequencies $\operatorname{Im}\omega_c = -\kappa$ and $\operatorname{Im}\omega_j = -\frac{1}{2}\gamma_{\mathrm{hom}}$ and the resolvent of the Hamiltonian H' is defined as $\mathrm{G}(z) = 1/\left(z - \mathrm{H}'\right)$.

Let us consider the state $|\varphi_c\rangle = |1_c, 0, \ldots, 0\rangle$ where we have one photon in the cavity and no excitation in the ensemble.

The matrix element of the resolvent $\mathrm{G}_{cc}(z) = \langle\varphi_c| \, \mathrm{G}(z) \, |\varphi_c\rangle$ can be written as

$$G_{cc}(z) = \frac{1}{z - E_c - R_{cc}(z)} \ , \tag{5.8.4}$$

where we define the matrix element of the level shift operator

$$
\begin{aligned}
R_{cc}\left(z\right) = V'_{cc} &+ \sum_{i\neq c} V'_{ci}\frac{1}{z-E_i}V'_{ic} \\
&+ \sum_{i\neq c}\sum_{j\neq c} V'_{ci}\frac{1}{z-E_i}V'_{ij}\frac{1}{z-E_j}V'_{jc} + \dots \ ,
\end{aligned}
\tag{5.8.5}
$$

where $V'_{kl} = \langle\varphi_k|\,\mathrm{V}'\,|\varphi_l\rangle$ and $E_c = \langle\varphi_c|\,\mathrm{H}'_0\,|\varphi_c\rangle$. States $|\varphi_i\rangle$ with $i \neq c$ are states where the excitation is absorbed in the ensemble spin i. We note that $V'_{cc} = 0$ and that $V'_{ij} = 0$ for $i, j \neq c$ since our Hamiltonian does not include spin-spin interaction. Only the second term in Eq. (5.8.5) remains and we can write

$$
R_{cc}\left(z\right) = \sum_{i\neq c}\frac{|g_i|^2}{z-E_i} \ . \tag{5.8.6}
$$

Introducing the coupling density profile $\rho\left(\omega\right) \equiv \sum_j |g_j|^2\,\delta\left(\omega - \mathrm{Re}\,\omega_j\right)$ as it is done in [5.13] leads to

$$
R_{cc}\left(z\right) = \int \frac{\rho\left(\omega\right)}{z-\omega+\frac{\mathrm{i}}{2}\gamma_{\mathrm{hom}}}\mathrm{d}\omega \ . \tag{5.8.7}
$$

Approaching the branch cut at $\omega - \frac{\mathrm{i}}{2}\gamma_{\mathrm{hom}}$ we write

$$
\lim_{\eta\to 0^+} R_{cc}\left(\omega - \frac{\mathrm{i}}{2}\gamma_{\mathrm{hom}} \pm \mathrm{i}\eta\right) = R^{\pm}_{cc}\left(\omega - \frac{\mathrm{i}}{2}\gamma_{\mathrm{hom}}\right) \ . \tag{5.8.8}
$$

Using $\lim_{\eta\to 0^+}\frac{1}{x\pm\mathrm{i}\eta} = \mathcal{P}\frac{1}{x} \mp \mathrm{i}\pi\delta\left(x\right)$, where $\mathcal{P}$ denotes the Cauchy principal value, we find

$$
R^{\pm}_{cc}\left(\omega - \frac{\mathrm{i}}{2}\gamma_{\mathrm{hom}}\right) = \mathcal{P}\int\frac{\rho\left(\omega'\right)}{\omega-\omega'}\mathrm{d}\omega' \mp \mathrm{i}\pi\rho\left(\omega\right) \ . \tag{5.8.9}
$$

Experimentally we probe the transmission of a weak probe signal amplitude through the cavity as a function of frequency. The position and shape of the weak-field transmission resonances can be determined from the complex poles of $G^{+}_{cc}\left(\omega\right) = 1/\left(\omega - \omega_c - R^{+}_{cc}\left(\omega\right)\right)$, which contains the spin energy distribution on the right-hand side. We can therefore extract information about the coupling density $\rho\left(\omega\right) = -\frac{1}{\pi}\,\mathrm{Im}\,R^{+}_{cc}\left(\omega - \frac{\mathrm{i}}{2}\gamma_{\mathrm{hom}}\right)$ by carefully analyzing the measured transmission spectrum.

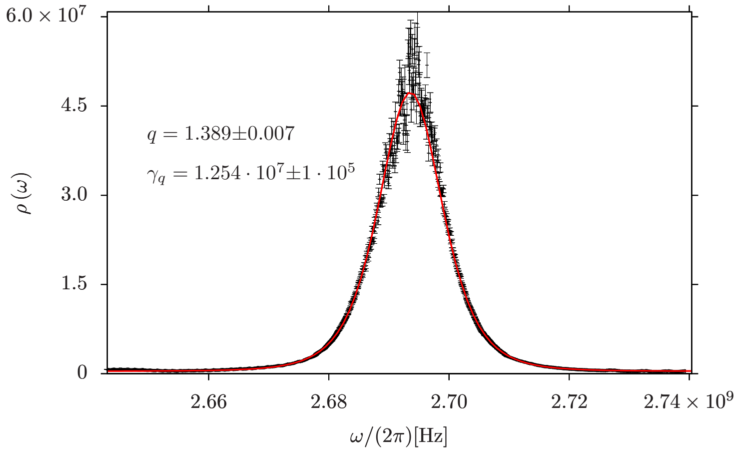

Figure 5.4.: (Color online) Coupling density of the ensemble determined from an exemplary transmission measurement at $T = 20\,\mathrm{mK}$. The errorbars are calculated from the uncertainties in $R_{cc}^{+}(\omega)$ which we obtain from fitting Eq. (5.8.11) to the data. We fit the q-Gaussian (red) in Eq. (5.8.12) to the coupling density to determine the width and the behavior of the tails of the distribution.

For small γ_{hom} the reconstruction simplifies to:

$$\rho(\omega) \approx -\frac{1}{\pi} \operatorname{Im} R_{cc}^{+}(\omega) + \frac{1}{2\pi} \frac{\partial \operatorname{Re} R_{cc}^{+}(\omega)}{\partial \omega} \gamma_{\mathrm{hom}} \,, \tag{5.8.10}$$

where $\operatorname{Im} R_{cc}^{+}\left(\omega - \frac{\mathrm{i}}{2}\gamma_{\mathrm{hom}}\right)$ is expanded in a Taylor series around $\gamma_{\mathrm{hom}} = 0$. We can therefore directly use the frequency distribution of the transmitted signal $|\langle a_c \rangle_{\mathrm{st}}|^2$ via

$$\begin{aligned} |\langle a_c \rangle_{\mathrm{st}}|^2 &\propto \left| G_{cc}^{+}(\omega, \omega_c) \right|^2 \\ &= \frac{1}{\left(\omega - \omega_c - \operatorname{Re} R_{cc}^{+}(\omega)\right)^2 + \left(\kappa + \operatorname{Im} R_{cc}^{+}(\omega)\right)^2} \end{aligned} \tag{5.8.11}$$

to determine $R_{cc}^{+}(\omega)$. Let us point out here that Eq. (5.8.11) exhibits a Lorentzian shape as a function of ω_c with peak position $\omega - \operatorname{Re} R_{cc}^{+}(\omega)$ and peak width of $2\left(\kappa + \operatorname{Im} R_{cc}^{+}(\omega)\right)$. After extraction of the relevant parameters which determine $R_{cc}^{+}(\omega)$ from the measured spectra, we can simply use Eq. (5.8.10) to find the coupling density $\rho(\omega)$. Assuming that all spins are coupled with equal strength, one finds that $\rho(\omega) = g^2 N \mathcal{M}(\omega)$ where $\mathcal{M}(\omega)$ is the frequency distribution of the spins.

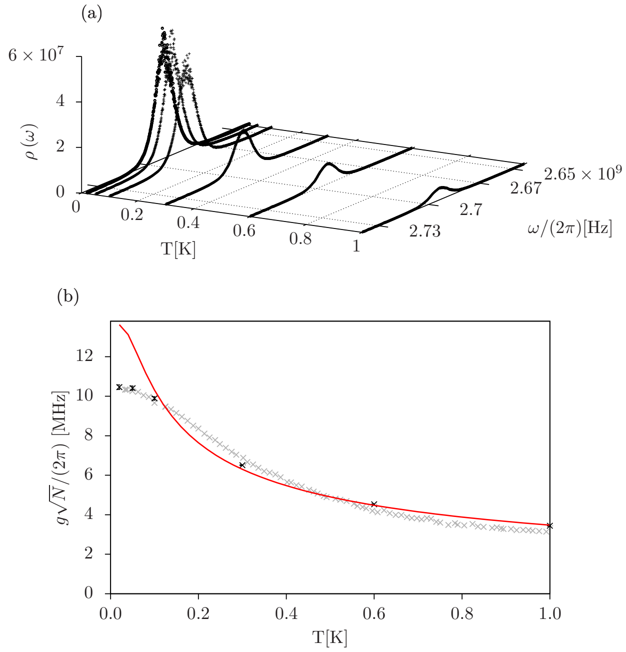

Figure 5.5.: (Color online) In (a) we show the coupling density for different temperatures. The q-parameter and width γ_q of the coupling density do not change significantly with increasing temperature. The coupling $g\sqrt{N} = \left(\int \rho(\omega)\,\mathrm{d}\omega\right)^{1/2}$ is reduced, as can be seen in (b). The red line shows $\Omega(T) = a_0\left[\tanh\left(\hbar\omega_-^{\mathrm{I}}/(2k_BT)\right)\right]^{1/2}$ with a_0 chosen to match the high temperature limit of the data (black markers). To compare $\Omega(T)$ with our previous results determined directly from the splitting we plot the data already shown in Fig. 5.3 using grey markers.

The shape of the coupling density, i.e., the frequency distribution of the spins, plays an important role in the cavity-ensemble interaction [5.12, 5.13]. If the coupling density falls off sufficiently fast with distance from the center, the width of the Rabi peaks will decrease with increasing collective coupling strength $g\sqrt{N}$. For the spin frequency distribution, the limiting case is the Lorentzian coupling density profile, for which the width of the Rabi peaks is independent of $g\sqrt{N}$ [5.12]. Any distribution falling faster than $1/\omega^2$ will provide a decrease of the width of the Rabi peaks. Moreover, knowing the coupling density gives us the opportunity to study the transmission through the cavity for different parameter ranges via Eq. (5.8.4).

To determine $\rho(\omega)$ the raw data have to be rearranged, since in the experiment we cannot simply vary ω_c but we shift the center frequency of the spins by a magnetic field. We therefore shift each scan by $\omega_c - \omega_-^{\mathrm{I}}(B)$ to obtain fixed ensemble frequencies and tuning of the cavity frequency. As the only significant quantity is the detuning between the cavity and the ensemble this does not change the dynamics. For fixed ω we fit a Lorentzian to $\left|G_{cc}^{+}(\omega, \omega_c)\right|^2$ to determine $R_{cc}^{+}(\omega)$ in order to calculate $\rho(\omega)$. We plot an exemplary result for $\rho(\omega)$ in Fig. 5.4. To determine the behavior of the tails of the distribution we fit the function

$$L(\omega) = b + I\left[1 - (1-q)\frac{(\omega - \omega_0)^2}{a}\right]^{\frac{1}{1-q}}, \tag{5.8.12}$$

to the data. $L(\omega)$ is related to the q-Gaussian, a Tsallis distribution. The dimensionless parameter $1 < q < 3$ determines how fast the tails of the distribution fall off, while a is related to the width. The actual width (FWHM) is given by $\gamma_q = 2\sqrt{\frac{a(2^q-2)}{2q-2}}$. For $q \to 1$ we recover a Gaussian distribution, while for $q = 2$ we find a Lorentzian distribution. The wings fall off as $1/\omega^{2/(q-1)}$.

From the fit in Fig. 5.4 we find values for $q = 1.389 \pm 0.007$ and $\gamma_q/(2\pi) = (12.54 \pm 0.10)$ MHz. The temperature during the measurement was 20 mK.

The same analysis is performed for data measured for $T = 20 - 1000$ mK, see Fig. 5.5(a). The fitted curves are not shown. For the resulting coupling densities we find almost no change in the width or the q-parameter. However, with increasing temperature $\int \rho(\omega)\,\mathrm{d}\omega = g^2 N$ is reduced, as can be seen in Fig. 5.5(b). The resulting coupling strength is in agreement with the results obtained from the analysis in Sec. 5.7. It also reproduces the unexpected behavior for small values of T.

To study the behavior of an ensemble following a q-Gaussian distribution with the q-parameter we determined, we show $\left|G_{cc}(\omega)\right|^2$ for $\omega_c = \omega_0$ as a function of the collective coupling strength $g\sqrt{N}$ in Fig. 5.6 b). The transmission for an ensemble with Gaussian distribution ($q \to 1$) is shown in Fig. 5.6 a) and for a Lorentzian distribution ($q \to 2$) is shown in Fig. 5.6 c). The width parameter a is chosen accordingly to ensure that γ_q is the same for all three cases. In Figs. 5.6 d)-f) the transmission for the three ensemble types is shown for $g\sqrt{N} = 4, 8$ and 16 MHz, respectively. For the ensemble with Lorentzian distribution (solid black line) we see that the width of the Rabi resonances remains constant with increasing collective coupling. For the Gaussian distribution (dotted black line) and the intermediate distribution with $q = 1.39$ (dashed red line) we find a decrease in the peak width for increasing collective coupling. In Fig. 5.7 we plot the real and imaginary part of one of the complex poles of $G_{cc}^{+}(\omega)$, determining the position and width of one of

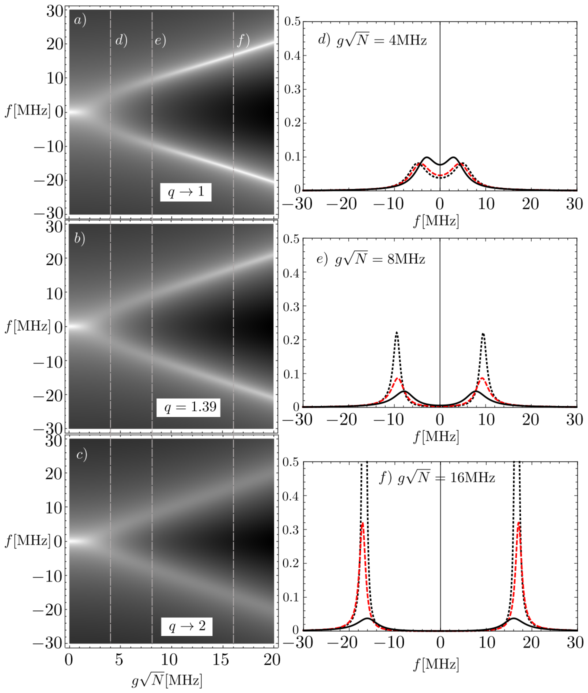

Figure 5.6.: (Color online) We plot $|G_{cc}(\omega)|^2$ as a function of the collective coupling strength $g\sqrt{N}$ and for three different values of the q-Gaussian parameter q (grayscale figures on the left are plotted on a logarithmic scale). For $g\sqrt{N} = 4, 8$ and 16 MHz, marked by d), e) and f) we show the transmission for all three values of q together. The transmission for the Gaussian coupling density with $q \to 1$ (dotted black line), for the coupling density of our ensemble with $q = 1.39$ (dashed red line) and for the Lorentzian coupling density with $q \to 2$ (solid black line) are shown on the right. The parameters were chosen to $\gamma_q/(2\pi) = 10$ MHz, $\kappa/(2\pi) = 0.4$ MHz and $\gamma_{\text{hom}}/(2\pi) = 1$ Hz.

the Rabi peaks. As we focus on the resonant case the spectrum is symmetric. We chose $\gamma_{\text{hom}} = 0$, $\kappa/(2\pi) = 0.4$ MHz, $\gamma_q/(2\pi) = 10$ MHz, and $q = 1.39$. This again shows the decreasing width of the Rabi Peaks as $g\sqrt{N}$ increases.

We therefore assume that for our ensemble it is possible to increase the lifetime of the collective states by increasing the collective coupling. This could be achieved by a further decrease of the mode volume or an increase of the NV density in the sample.

In Fig. 5.8 we show the behavior of the transmission with increasing γ_q. For the Lorentzian coupling density the splitting of the resonance peaks is always reduced if $\gamma_q > 0$. For coupling densities falling off faster than $1/\omega^2$, as is the case in Figs. 5.8(a) and (b), the splitting of the resonance peaks is even slightly increased for $\gamma_q > 0$,

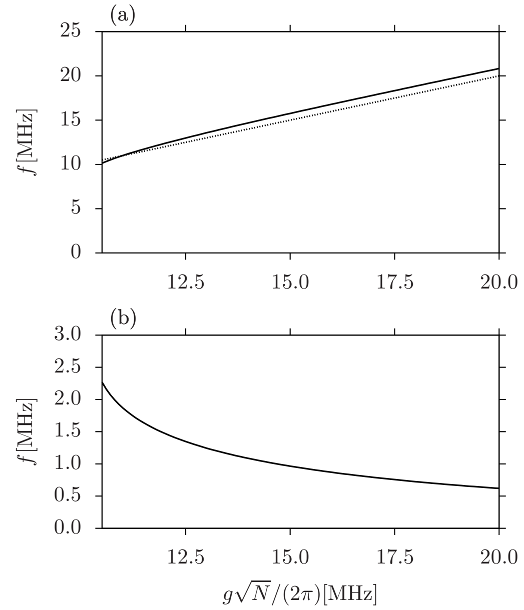

Figure 5.7.: (a) Real part and (b) modulus of the imaginary part of one of the complex poles of $G^+_{cc}(\omega)$ in the regime where $g\sqrt{N}/(2\pi) > \gamma_q/(2\pi) = 10$ MHz. The collective coupling strength $g\sqrt{N}$ is shown as dotted line in (a). With increasing $g\sqrt{N}$ the modulus of the imaginary part, proportional to the width of the Rabi peaks, is reduced.

until the peaks finally merge. Hence a finite but small enough inhomogeneous width might even mimic somewhat higher active spin numbers.

As a bottom line we see that common coupling to a cavity mode can suppress dephasing of the polarization, if the effective Rabi frequency is larger than the inhomogeneous width. This could be interpreted as the effect that the exchange of the excitation between the ensemble and the cavity is so fast, that there is no time for decoherence in the ensemble.

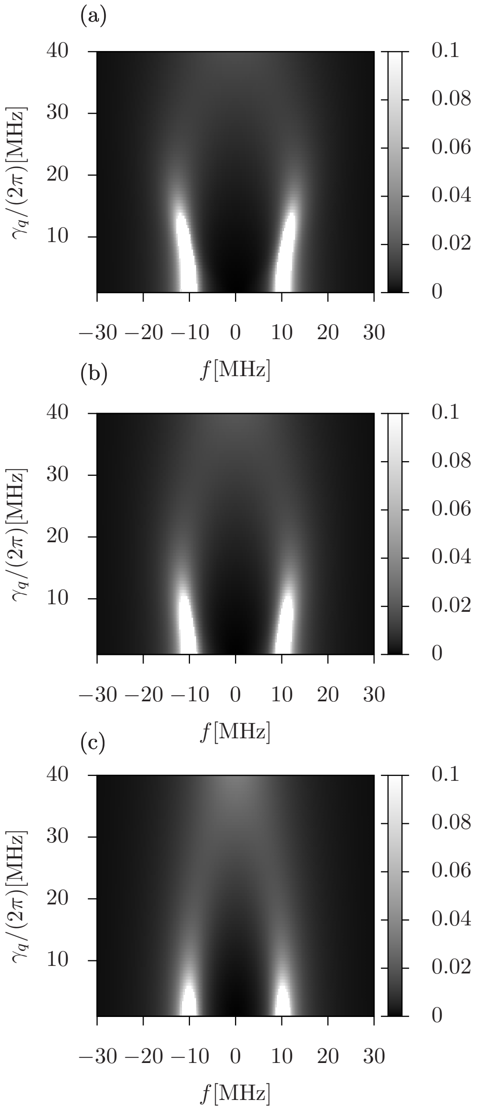

Figure 5.8.: $|G_{cc}(\omega)|^2$ on resonance as a function of the inhomogeneous width γ_q for an ensemble with (a) Gaussian coupling density, (b) q-Gaussian ($q = 1.39$) coupling density and (c) Lorentzian coupling density. To keep the transmission visible for large values of γ_q the range of the color coding is limited to $[0, 0.1]$. The parameters were chosen to $g\sqrt{N}/(2\pi) = 10$ MHz, $\kappa/(2\pi) = 0.4$ MHz and $\gamma_{\mathrm{hom}}/(2\pi) = 1$ Hz.

5.9. A transmission line micro-maser with an inhomogeneous NV ensemble

A recent proposal to construct a laser operating on an ultra-narrow atomic clock transition predicted very narrow optical emission above threshold [5.17]. Similar ideas, employing the collective coupling between a cold atomic ensemble and a microwave cavity, have been proposed to construct stable stripline oscillators in the microwave regime [5.18].

Here we study the prospects of implementing such an oscillator by coupling a diamond to the CPW resonator. At first sight in view of the MHz scale inhomogeneous broadening, one would expect fast dephasing. However, as we have seen above, for strong enough coupling one observes a continuous rephasing of the polarization inducing a long lived polarization and coherent Rabi oscillations. Thus one could expect narrow microwave emission nevertheless.

Let us consider the case of the cavity mode tuned to resonance with the spin transition $|0\rangle_{\mathrm{I}} \rightarrow |-\rangle_{\mathrm{I}}$, which is partially inverted by an external incoherent pump. Such a pump could in principle be facilitated by optical pumping and it can be consistently modeled by a reversed spontaneous decay. Alternatively one could think of pulsed inversion by tailored microwave pulses or a time switching of the magnetic bias field.

Mathematically such incoherent pumping can be modelled by adding the terms $-\frac{w}{2}\sum_{j=1}^{N}\left(\sigma_j^-\sigma_j^+\rho + \rho\sigma_j^-\sigma_j^+ - 2\sigma_j^+\rho\sigma_j^-\right)$, where w denotes the pump rate, to the Liouvillian in Eq. (5.7.3).

For the explicit calculations, here we use the effective linewidth model, as outlined in Sec. 5.7 without any coherent pump. Hence the total phase symmetry of the system is not broken and we assume $\langle a_c\rangle = \left\langle a_c^\dagger\right\rangle = \left\langle \sigma_j^\pm\right\rangle = 0$. Starting from the master equation in Eq. (5.7.2) we derive four coupled equations for $\left\langle\sigma_j^z\right\rangle$, $\left\langle a_c^\dagger a_c\right\rangle$, $\left\langle a_c\sigma_i^+\right\rangle$, and $\left\langle\sigma_i^+\sigma_j^-\right\rangle$. We used the cumulant expansion $\left\langle a_c^\dagger a_c\sigma_i^z\right\rangle = \left\langle a_c^\dagger a_c\sigma_i^z\right\rangle_{\mathrm{cum}} + \left\langle a_c^\dagger a_c\right\rangle\left\langle\sigma_i^z\right\rangle$ which takes this simple form because of the total phase invariance. Assuming that the higher-order cumulant $\left\langle a_c^\dagger a_c\sigma_i^z\right\rangle_{\mathrm{cum}}$ can be neglected, we arrive at a closed set of four equations that can be solved analytically.

To study the spectrum of the emitted light we calculate the two-time correlation function $\left\langle a_c^\dagger(\tau)\, a_c(0)\right\rangle$ via the quantum regression theorem. We switch to a frame

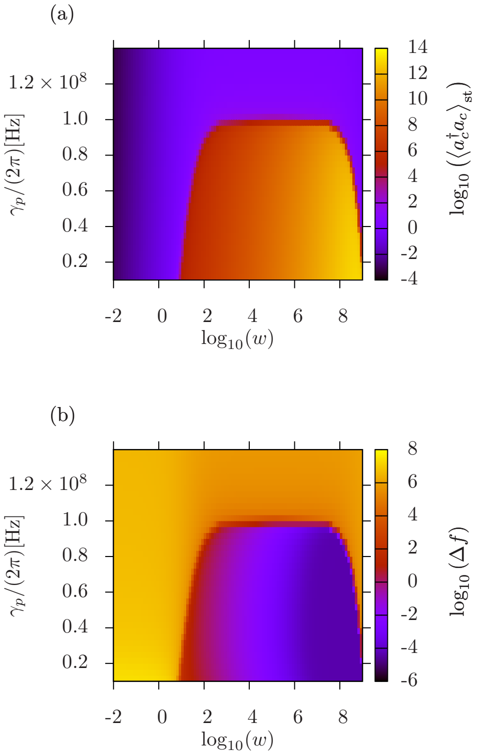

Figure 5.9.: (Color online) In (a) we show the steady state number of photons in the cavity $\left\langle a_c^\dagger a_c\right\rangle_{\mathrm{st}}$ as a function of the incoherent pump rate w and the inhomogeneous width γ_p. The resulting linewidth Δf is shown in (b). For small γ_p both, Δf and $\left\langle a_c^\dagger a_c\right\rangle_{\mathrm{st}}$ show rapid changes as w becomes larger than γ_{hom}. The critical width of the inhomogeneity is given by $\gamma_{p,\mathrm{crit}} = g^2 N/\kappa$. The parameters were chosen to $N = 10^{12}$, $g/(2\pi) = 10$ Hz, $\kappa/(2\pi) = 1$ MHz and $\gamma_{\mathrm{hom}}/(2\pi) = 1$ Hz.

rotating with ω_c and define $\Delta = \omega_-^{\mathrm{I}} - \omega_c$. We obtain

$$\frac{\mathrm{d}}{\mathrm{d}\tau}\begin{pmatrix}\left\langle a_c^\dagger(\tau)\, a_c(0)\right\rangle \\ \left\langle \sigma_i^+(\tau)\, a_c(0)\right\rangle\end{pmatrix} = \begin{pmatrix} -\kappa & \mathrm{i}gN \\ -\mathrm{i}g\left\langle\sigma_i^z\right\rangle_{\mathrm{st}} & -\left(\frac{w+\gamma_{\mathrm{hom}}}{2} + \gamma_{\mathrm{hom}}\bar{n}\left(T,\omega_-^{\mathrm{I}}\right) + \gamma_p - \mathrm{i}\Delta\right)\end{pmatrix}\begin{pmatrix}\left\langle a_c^\dagger(\tau)\, a_c(0)\right\rangle \\ \left\langle \sigma_i^+(\tau)\, a_c(0)\right\rangle\end{pmatrix} \tag{5.9.1}$$

From Eq. (5.9.1) we can calculate the spectrum via Laplace transformation [5.20]. We show the linewidth of the obtained spectrum in the resonant case ($\Delta = 0$) for different values of the pump w and the inhomogeneous width γ_p (see Fig. 5.9). The minimum linewidth is $\Delta f \approx g^2/\kappa$. For small γ_p the region where we find narrow linewidth emission is characterized by $\gamma_{\text{hom}} < w < 2g^2N/\kappa$. The critical width of the inhomogeneity is given by $\gamma_{p,\text{crit}} = g^2N/\kappa$. Hence once we achieve enough pumping and coupling strength the system could provide for an extremely stable microwave oscillator.

5.10. Conclusions

We showed theoretically and experimentally that an ensemble of spins with an inhomogeneous frequency distribution coupled to a cavity mode can exhibit strong coupling, where the coherent energy exchange between mode and ensemble dominates cavity decay and polarization dephasing. A detailed theoretical modeling connecting probe transmission and frequency distribution allows us to extract not only the effective coupling strength and particle number but also the detailed frequency distribution. The microscopic mechanisms that cause the inhomogeneous broadening are not treated as a central theme in this work, but we hope that the knowledge of the frequency distribution can be of use in further investigations on this subject. Interestingly for our dense NV ensemble, the frequency distribution of the spins can be well described as a q-Gaussian with $q = 1.39$, showing that the wings of the distribution fall off faster than $1/\omega^2$. The temperature dependence of the effective available spin number fits quite well with expectations, except for an unexpected decrease for very low temperature. In summary such an NV-ensemble cavity QED system exhibits a prolonged lifetime of the eigenstates of the coupled cavity-ensemble system [5.13] and has great potential as a quantum interface between superconducting and optical qubits. The long effective T_1 time could also be the basis of building a compact ultrastable microwave oscillator if the strong coupling overcomes the dephasing from the inhomogeneous broadening.

5.11. Acknowledgment

We thank Klaus Mølmer for his helpful remarks and open discussions. K.S. was supported by the DOC-fFORTE doctoral program. R.A. and T.N. were supported by CoQuS, C.K. by FunMat. We acknowledge support by the Austrian Science Fund FWF through the project SFB F40.

References for Chapter 5

[5.1] DF Phillips et al. “Storage of light in atomic vapor.” In: *Physical Review Letters* 86.5 (2001), pp. 783–786.

[5.2] JM Taylor et al. “High-sensitivity diamond magnetometer with nanoscale resolution.” In: *Nature Physics* 4.10 (2008), pp. 810–816.

[5.3] J. Verdú et al. “Strong magnetic coupling of an ultracold gas to a superconducting waveguide cavity.” In: *Physical Review Letters* 103.4 (2009), p. 43603.

[5.4] P. Rabl et al. “Hybrid quantum processors: molecular ensembles as quantum memory for solid state circuits.” In: *Physical review letters* 97.3 (2006), p. 33003.

[5.5] P. Bushev et al. “Ultralow-power spectroscopy of a rare-earth spin ensemble using a superconducting resonator.” In: *Physical Review B* 84.6 (2011), p. 060501.

[5.6] Y. Kubo et al. “Strong coupling of a spin ensemble to a superconducting resonator.” In: *Physical Review Letters* 105.14 (2010), p. 140502.

[5.7] R. Amsüss et al. “Cavity QED with Magnetically Coupled Collective Spin States.” In: *Physical Review Letters* 107.6 (2011), pp. 1–5. DOI: `10.1103/PhysRevLett.107.060502`. URL: `http://link.aps.org/doi/10.1103/PhysRevLett.107.060502`.

[5.8] F. Jelezko and J. Wrachtrup. “Single defect centres in diamond: A review.” In: *physica status solidi (a)* 203.13 (2006), pp. 3207–3225.

[5.9] L. Childress et al. “Coherent dynamics of coupled electron and nuclear spin qubits in diamond.” In: *Science* 314.5797 (2006), p. 281.

[5.10] VM Acosta et al. “Diamonds with a high density of nitrogen-vacancy centers for magnetometry applications.” In: *Physical Review B* 80.11 (2009), p. 115202.

[5.11] R. Houdré, RP Stanley, and M. Ilegems. “Vacuum-field Rabi splitting in the presence of inhomogeneous broadening: Resolution of a homogeneous linewidth in an inhomogeneously broadened system.” In: *Physical Review A* 53.4 (1996), p. 2711.

[5.12] I. Diniz et al. “Strongly coupling a cavity to inhomogeneous ensembles of emitters: potential for long lived solid-state quantum memories.” In: *Arxiv preprint arXiv:1101.1842* (2011).

[5.13] Z. Kurucz, J.H. Wesenberg, and K. Mølmer. “Spectroscopic properties of inhomogeneously broadened spin ensembles in a cavity.” In: *Physical Review A* 83.5 (2011), p. 053852.

[5.14] D. Braun, J. Hoffman, and E. Tiesinga. “Superradiance of cold atoms coupled to a superconducting circuit.” In: *Physical Review A* 83.6 (2011), p. 062305.

[5.15] H.J. Carmichael. *An open systems approach to quantum optics: lectures presented at the Université libre de Bruxelles, October 28 to November 4, 1991.* Vol. 18. Springer, 1993.

[5.16] R. Kubo. “Generalized cumulant expansion method.” In: *J. Phys. Soc. Japan* 17.7 (1962), pp. 1100–1120.

[5.17] D. Meiser et al. “Prospects for a millihertz-linewidth laser.” In: *Physical Review Letters* 102.16 (2009), p. 163601.

[5.18] K. Henschel et al. “Cavity QED with an ultracold ensemble on a chip: Prospects for strong magnetic coupling at finite temperatures.” In: *Physical Review A* 82.3 (2010), p. 033810.

[5.19] C. Cohen-Tannoudji, J. Dupont-Roc, and G. Grynberg. *Atom-photon interactions: basic processes and applications.* Wiley Online Library, 1992.

[5.20] P. Meystre and M. Sargent. *Elements of quantum optics.* Springer Verlag, 2007.

Part II.

Quantum cascade lasers

6. Introduction to quantum cascade lasers

Quantum cascade (QC) lasers are built from thin layers of semiconductor material that form a repetitive pattern of quantum wells. The thickness of the barriers between the wells can be designed to form a requested structure of the energy levels, tunneling rates between the wells and dipole matrix elements for transitions within a well [6.1, 6.2]. An electron that passes through the structure undergoes several intraband transitions. This constitutes the main difference between QC lasers and conventional semiconductor lasers which are based on interband transitions between the conduction and valence band.

To operate the device, an external electric field is applied so that electrons tunnel into the active region of the QC laser, as indicated in Fig. 6.1. The ratio of the scattering times between the upper laser level $|u\rangle$ and lower laser level $|l\rangle$, τ_{ul} and between $|l\rangle$ and $|i\rangle$, τ_{li} can be designed to allow for laser action. This can be done by deliberately choosing the energy separation between $|l\rangle$ and $|i\rangle$ to be close to the energy of non-radiative phonon modes, ensuring very short τ_{li}. In general there are several other scattering paths for the electrons that allow electrons to bypass the ideal carrier transport path indicated in Fig. 6.1 and it is a major goal of QC laser design to suppress these paths [6.2].

Here we develop a simplified theoretical description of QC lasers that allows to study the temperature dependence of the laser activity and the dynamics of coupled QC lasers. Details concerning the design and growth of the structures are beyond the scope of this thesis and are therefore omitted.

6.1. Devices

There are many different designs of QC lasers available [6.2]. Here we intend to study QC lasers implemented as microdisc cavities. The cavities are formed by etching

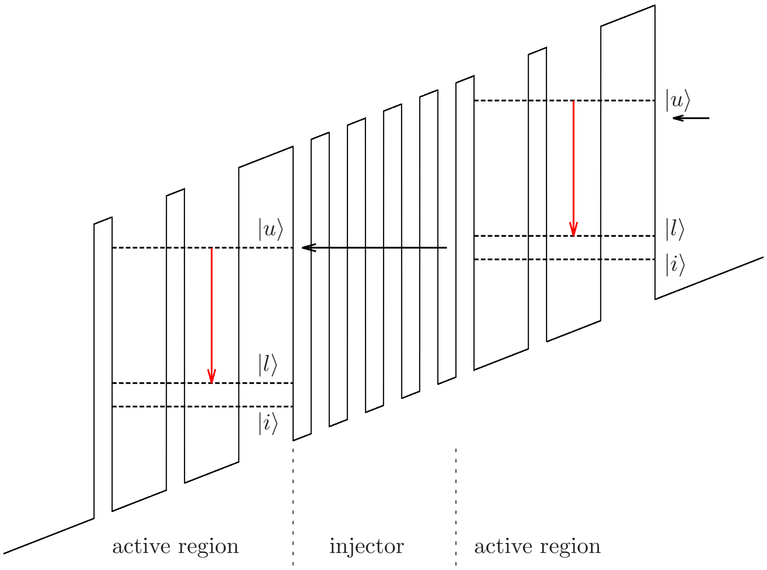

Figure 6.1.: Schematic representation of the repetitive quantum well structure emerging as a result of the arrangement of the semiconductor layers. The overall slope visualizes the applied electric field. The horizontal arrows indicate the flow of electrons while the laser transitions are depicted as red arrows. The injector region contains several energy levels that are not specified in this sketch. A common value for the thickness of each period of the structure is ≈ 50 nm [6.3].

of the previously grown heterostructure so that cylindrical structures with a radius of $r \approx 50$ µm and with perpendicular and smooth boundaries remain [6.4, 6.5]. Sub-wavelength sized cavities can be designed to support only a single whispering-gallery mode. The light is confined by the boundary of the disk as it impinges on the outer edge with an angle larger than the critical angle of refraction according to the refractive index of the laser material. Contact layers on the top and bottom allow for electrical pumping of the structure. The number of repetitions of the periodic heterostructure differs strongly depending on the wavelength of the QC laser. For infrared QC lasers 30 repetitions are required while for THz QC lasers about 200 repetitions are necessary.

Microdisc QC lasers can be coupled by placing them in close proximity [6.5]. The strength of the coupling is proportional to the distance as the coupling is accomplished via the evanescent fields of the whispering-gallery modes, see Fig. 6.4.

In Sec. 6.2 we develop a simplified theoretical description of a single cascade laser

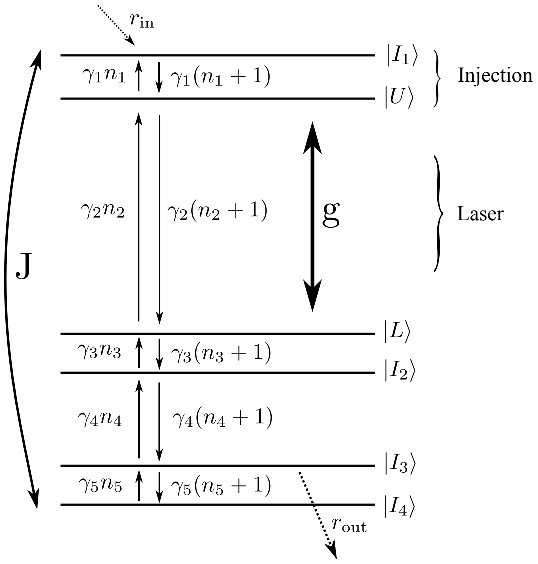

Figure 6.2.: Energy levels of a single cascade pattern with coherent repumping of the upper injection level $|I_1\rangle$ at rate J. The states $|U\rangle$ and $|L\rangle$ are the upper and lower laser levels.

and study the lasing activity as a function of the temperature of the laser material. In Sec. 6.3 the description is extended to include the coupling between two lasers.

6.2. Theoretical description of a single QC laser

To describe a single cascade laser we introduce a model for a single element of the repetitive cascade structure into which electrons enter at the rate r_{in} and leave it at the rate r_{out}, see Fig. 6.2. In real devices an electron passes trough many elements of the cascade, which is described in the model by a coherent pump of rate J that recycles population from the state $|I_4\rangle$ to the state $|I_1\rangle$. The cavity is resonant with the transition between the laser levels $|U\rangle$ and $|L\rangle$. A corresponding Hamiltonian reads

$$\begin{aligned}
\mathrm{H} &= \mathrm{H}_0 + \mathrm{H}_\mathrm{I} + \mathrm{V} \\
&= \hbar\omega_m a^\dagger a + \hbar\omega_u |U\rangle\langle U| + \hbar\omega_l |L\rangle\langle L| + \sum_{j=1}^{4} \hbar\omega_j |I_j\rangle\langle I_j| \\
&+ \mathrm{i}\hbar g\left(a\sigma_{UL} - a^\dagger\sigma_{LU}\right) + \mathrm{i}\hbar\left(J\sigma_{14} - J^*\sigma_{41}\right) \;, \qquad (6.2.1)
\end{aligned}$$

where we introduced the cavity photon annihilation operator a, the coupling constant g, and the abbreviation $\sigma_{ij} = |i\rangle\langle j|$. The transition frequencies are set to $\omega_1 - \omega_u = 2\pi \times 1$ GHz, $\omega_u - \omega_l = 2\pi \times 3$ THz, $\omega_l - \omega_2 = 2\pi \times 1$ GHz, $\omega_2 - \omega_3 = 2\pi \times 1$ THz, and $\omega_3 - \omega_4 = 2\pi \times 1$ GHz. We define all frequencies with respect to ω_l and transform to a frame rotating with ω_m, introducing the detunings $\Delta_u = \omega_u - \omega_m$, $\Delta_j = \omega_j - \omega_m$ with $j = 1, \ldots, 4$. We furthermore introduce the phenomenological gain shift factor α and define $\Delta'_u = \Delta_u + \alpha V_{\text{ext}}$, where V_{ext} is the applied voltage, and the carrier induced shift of the mode $\Delta'_m = \beta\left(\langle L\rangle - \langle U\rangle\right)$. Note that number of repetitions of the periodic heterostructure is implicitly contained in the ratio between the pump rate J and the rate of carrier extraction r_{out}.

Dissipative processes include the spontaneous transition rates between the states and losses due to imperfections of the cavity. We furthermore assume that the device is at $T \neq 0$, resulting in a thermal occupation of the mode and incoherent transitions within the heterostructure, induced by thermal photons or phonons.

To include the dissipative processes in our description we follow the master equation approach

$$\frac{\mathrm{d}}{\mathrm{d}t}\rho = \frac{\mathrm{i}}{\hbar}\left[\rho, \tilde{\mathrm{H}}\right] + \mathcal{L}\left[\rho\right] \ , \tag{6.2.2}$$

where $\tilde{\mathrm{H}}$ is the Hamiltonian in the rotating frame and the Liouvillian is given by

$$\begin{aligned}
\mathcal{L}\left[\rho\right] = {} & \kappa\left(n_2 + 1\right)\left(2a\rho a^\dagger - a^\dagger a\rho - \rho a^\dagger a\right) \\
& + \kappa n_2\left(2a^\dagger\rho a - aa^\dagger\rho - \rho aa^\dagger\right) \\
& + \frac{\gamma_1\left(n_1 + 1\right)}{2}\left(2\sigma_{U1}\rho\sigma_{1U} - \sigma_{1U}\sigma_{U1}\rho - \rho\sigma_{1U}\sigma_{U1}\right) \\
& + \frac{\gamma_1 n_1}{2}\left(2\sigma_{1U}\rho\sigma_{U1} - \sigma_{U1}\sigma_{1U}\rho - \rho\sigma_{U1}\sigma_{1U}\right) \\
& + \frac{\gamma_2\left(n_2 + 1\right)}{2}\left(2\sigma_{LU}\rho\sigma_{UL} - \sigma_{UL}\sigma_{LU}\rho - \rho\sigma_{UL}\sigma_{LU}\right) \\
& + \frac{\gamma_2 n_2}{2}\left(2\sigma_{UL}\rho\sigma_{LU} - \sigma_{LU}\sigma_{UL}\rho - \rho\sigma_{LU}\sigma_{UL}\right) \\
& + \frac{\gamma_3\left(n_3 + 1\right)}{2}\left(2\sigma_{L2}\rho\sigma_{2L} - \sigma_{2L}\sigma_{L2}\rho - \rho\sigma_{2L}\sigma_{L2}\right) \\
& + \frac{\gamma_3 n_3}{2}\left(2\sigma_{2L}\rho\sigma_{L2} - \sigma_{L2}\sigma_{2L}\rho - \rho\sigma_{L2}\sigma_{2L}\right)
\end{aligned}$$

$$
\begin{aligned}
&+ \frac{\gamma_4 (n_4 + 1)}{2} (2\sigma_{32}\rho\sigma_{23} - \sigma_{23}\sigma_{32}\rho - \rho\sigma_{23}\sigma_{32}) \\
&+ \frac{\gamma_4 n_4}{2} (2\sigma_{23}\rho\sigma_{32} - \sigma_{32}\sigma_{23}\rho - \rho\sigma_{32}\sigma_{23}) \\
&+ \frac{\gamma_5 (n_5 + 1)}{2} (2\sigma_{43}\rho\sigma_{34} - \sigma_{34}\sigma_{43}\rho - \rho\sigma_{34}\sigma_{43}) \\
&+ \frac{\gamma_5 n_5}{2} (2\sigma_{34}\rho\sigma_{43} - \sigma_{43}\sigma_{34}\rho - \rho\sigma_{43}\sigma_{34}) \ . \qquad (6.2.3)
\end{aligned}
$$

We calculate expectation value equations up to second order. Third order expectation values are decomposed and third order cumulants are neglected. We also assume total phase invariance which results in $\langle a \rangle = \langle \sigma_{UL} \rangle = 0$. The populations of each energy level are determined by the equations

$$
\begin{aligned}
\frac{\mathrm{d}}{\mathrm{d}t} \langle U \rangle &= g \left(\left\langle a^\dagger \sigma_{LU} \right\rangle + \langle a \sigma_{UL} \rangle \right) + \gamma_1 (n_1 + 1) \langle I_1 \rangle \\
&\quad - (\gamma_1 n_1 + \gamma_2 (n_2 + 1)) \langle U \rangle + \gamma_2 n_2 \langle L \rangle \qquad (6.2.4) \\
\frac{\mathrm{d}}{\mathrm{d}t} \langle L \rangle &= -g \left(\left\langle a^\dagger \sigma_{LU} \right\rangle + \langle a \sigma_{UL} \rangle \right) + \gamma_2 (n_2 + 1) \langle U \rangle \\
&\quad - (\gamma_2 n_2 + \gamma_3 (n_3 + 1)) \langle L \rangle + \gamma_3 n_3 \langle I_2 \rangle \qquad (6.2.5)
\end{aligned}
$$

$$
\begin{aligned}
\frac{\mathrm{d}}{\mathrm{d}t} \langle I_1 \rangle &= J^* \langle \sigma_{41} \rangle + J \langle \sigma_{14} \rangle - \gamma_1 (n_1 + 1) \langle I_1 \rangle + \gamma_1 n_1 \langle U \rangle + r_{\text{in}} \qquad (6.2.6) \\
\frac{\mathrm{d}}{\mathrm{d}t} \langle I_2 \rangle &= -(\gamma_3 n_3 + \gamma_4 (n_4 + 1)) \langle I_2 \rangle + \gamma_4 n_4 \langle I_3 \rangle + \gamma_3 (n_3 + 1) \langle L \rangle \qquad (6.2.7) \\
\frac{\mathrm{d}}{\mathrm{d}t} \langle I_3 \rangle &= -(\gamma_4 n_4 + \gamma_5 (n_5 + 1)) \langle I_3 \rangle + \gamma_5 n_5 \langle I_4 \rangle + \gamma_4 (n_4 + 1) \langle I_2 \rangle \\
&\quad - r_{\text{out}} \langle I_3 \rangle \qquad (6.2.8) \\
\frac{\mathrm{d}}{\mathrm{d}t} \langle I_4 \rangle &= -J \langle \sigma_{14} \rangle - J^* \langle \sigma_{41} \rangle + \gamma_5 (n_5 + 1) \langle I_3 \rangle - \gamma_5 n_5 \langle I_4 \rangle \ . \qquad (6.2.9)
\end{aligned}
$$

The carrier input rate r_{in} determines the external pumping of the structure. To determine the input rate as a function of the applied voltage V_{ext} we introduce the phenomenological function [6.3]

$$
r_{\text{in}} (V_{\text{ext}}) = r_{\text{max}} \frac{w_{\text{res}}^4}{w_{\text{res}}^4 - (V_{\text{ext}} - V_{\text{res}})^4} \ , \qquad (6.2.10)
$$

where r_{max} is the maximum current injection rate, V_{res} is the voltage for which the maximum current is obtained and w_{res} is the width of the current curve.

For the transition dipole operator σ_{14} we obtain the equation

$$\frac{\mathrm{d}}{\mathrm{d}t}\left\langle\sigma_{14}\right\rangle = J^{*}\left(\left\langle I_4\right\rangle - \left\langle I_1\right\rangle\right) - \left(\frac{\gamma_1\left(n_1+1\right)}{2} + \frac{\gamma_5 n_5}{2}\right)\left\langle\sigma_{14}\right\rangle \ , \tag{6.2.11}$$

where we omitted the contribution $\mathrm{i}\left(\Delta_1 - \Delta_4\right)\left\langle\sigma_{14}\right\rangle$ which arises during the calculation. This is a reasonable assumption as we intend to describe the situation where the electron enters the next element of the cascade after leaving state $|I_4\rangle$. The assumption that the detuning between $|I_4\rangle$ and $|I_1\rangle$ of two adjacent elements is small justifies the omission of the contribution mentioned above. The emerging second order expectation value for the exchange of energy between the mode and the structure follows

$$\begin{aligned}\frac{\mathrm{d}}{\mathrm{d}t}\left\langle a\sigma_{UL}\right\rangle = &-g\left(\left(1+\left\langle a^{\dagger}a\right\rangle\right)\left\langle U\right\rangle - \left\langle a^{\dagger}a\right\rangle\left\langle L\right\rangle\right)\\ &-\left(\kappa + \frac{\gamma_1 n_1}{2} + \frac{\gamma_2\left(2n_2+1\right)}{2} + \frac{\gamma_3\left(n_3+1\right)}{2} + \mathrm{i}\Delta_m' - \mathrm{i}\Delta_u'\right)\left\langle a\sigma_{UL}\right\rangle \ ,\end{aligned} \tag{6.2.12}$$

while the equation for the photon number in the cavity is given by

$$\frac{\mathrm{d}}{\mathrm{d}t}\left\langle a^{\dagger}a\right\rangle = -g\left(\left\langle a\sigma_{UL}\right\rangle + \left\langle a^{\dagger}\sigma_{LU}\right\rangle\right) - 2\kappa\left\langle a^{\dagger}a\right\rangle + 2\kappa n_2 \ . \tag{6.2.13}$$

The equations are integrated numerically to determine the steady state. In Fig. 6.3 the steady state photon number in the cavity, which is proportional to the emitted intensity, is depicted as a function of the external voltage and the temperature. The sudden drop in $\left\langle a^{\dagger}a\right\rangle_{\mathrm{st}}$ for low temperatures is a result of the carrier injection. Only for an appropriate voltage we find resonant injection, described in our model by the function $r_{\mathrm{in}}\left(V_{\mathrm{ext}}\right)$. In Fig. 6.1 the external electric field is indicated by the overall slope of the quantum wells. For $V_{\mathrm{ext}} = V_{\mathrm{res}}$ the slope is such that resonant tunneling of carriers is possible, which is realized in the model by a peak in $r_{\mathrm{in}}\left(V_{\mathrm{ext}}\right)$. For $\Delta_u' = \Delta_m'$ the photon number in the cavity reaches a maximum. Further increase of V_{ext} causes the lasing activity to cease because cavity and medium are shifted out of resonance. This is certainly a very crude approximation for the carrier dynamics, which in principle requires self-consistent solutions. Nevertheless the solutions mimic the observed behavior surprisingly well [6.6].

This simplified model allows to simulate the lasing activity of a single QC laser operated at different temperatures. With increasing temperature the output power is reduced dramatically which is in accordance with experimental results [6.6]. In the next section we intend to study coupled QC lasers, where each laser is modeled

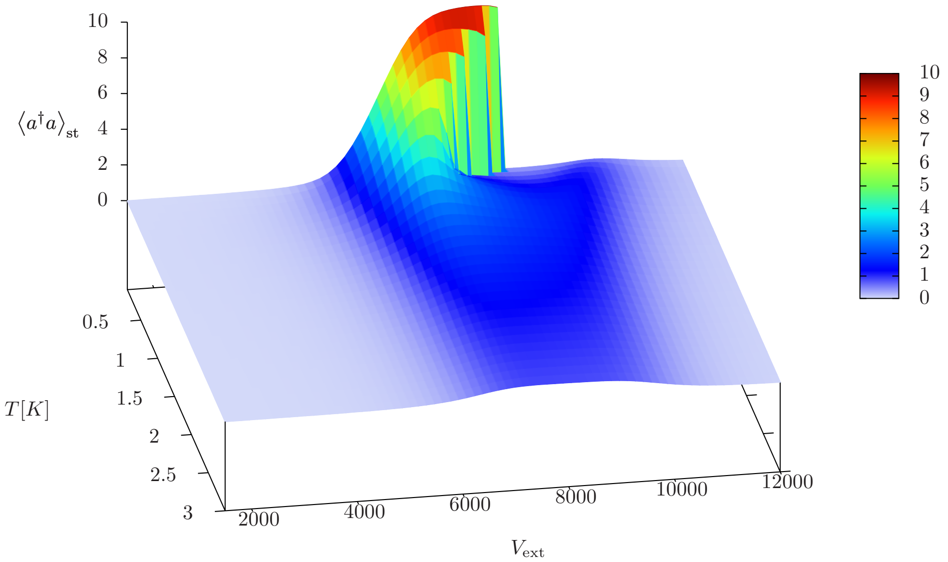

Figure 6.3.: Steady state number of photons in the cavity for different temperatures and applied voltages. The parameters were chosen to $\kappa = 2\pi \times 10\,\mathrm{Hz}$, $g = \kappa/3$, $\gamma_1 = 0.4\kappa$, $\gamma_2 = 0.1\kappa$, $\gamma_3 = \gamma_4 = \gamma_5 = 0.8\kappa$, $J = \kappa/(2\pi)$, $\Delta_u = -14\kappa$, $V_{\mathrm{res}} = 8000$, $w_{\mathrm{res}} = 2000$, $r_{\mathrm{max}} = 25\kappa$, $\alpha = 12\kappa/V_{\mathrm{res}}$, $\beta = 0.1\kappa$.

as described in this section plus an appropriate coupling term.

6.3. Coupled QC lasers

QC lasers can be coupled by placing them in close proximity of each other, so that the evanescent field of one laser overlaps with the microdisc of the second laser and vice versa. Photons in one mode can therefore switch over to the mode of the second laser. In experiments the emission from each lasers depends on whether the second laser is in the active voltage region or not, thereby exhibiting mutual blocking behavior [6.5]. Here we intend to check whether an extended version of the simplified model introduced for the description of a single laser is capable of reproducing the mutual blocking found in experiments. The Hamiltonian describing

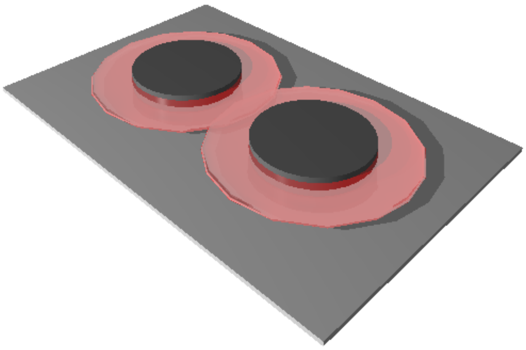

Figure 6.4.: Sketch of the two microdiscs on the ground plane. Each of the discs is etched from the repetitive heterostructure. The strength of the coupling between the QC lasers scales with the distance between the microdiscs. Photons can leave one laser mode and enter the mode of the other laser.

the coupled system reads

$$\mathrm{H} = \mathrm{H}_1 + \mathrm{H}_2 + \mathrm{H}_{\text{coupling}} \tag{6.3.1}$$

where H_1 and H_2 are defined analogously to Eq. (6.2.1),

$$\begin{aligned} \mathrm{H}_1 = {} & \hbar\omega_{m,1} a_1^\dagger a_1 + \hbar\omega_{u,1} \left|U_1\right\rangle \left\langle U_1\right| + \hbar\omega_{l,1} \left|L_1\right\rangle \left\langle L_1\right| + \sum_{j=1}^{4} \hbar\omega_{j,1} \left|I_{j,1}\right\rangle \left\langle I_{j,1}\right| \\ & + \mathrm{i}\hbar g_1 \left(a\sigma_{UL} - a^\dagger \sigma_{LU}\right) + \mathrm{i}\hbar \left(J_1 \sigma_{14} - J_1^* \sigma_{41}\right) \end{aligned} \tag{6.3.2}$$

and

$$\begin{aligned} \mathrm{H}_2 = {} & \hbar\omega_{m,2} a_2^\dagger a_2 + \hbar\omega_{u,2} \left|U_2\right\rangle \left\langle U_2\right| + \hbar\omega_{l,2} \left|L_2\right\rangle \left\langle L_2\right| + \sum_{j=1}^{4} \hbar\omega_{j,2} \left|I_{j,2}\right\rangle \left\langle I_{j,2}\right| \\ & + \mathrm{i}\hbar g_2 \left(a\pi_{UL} - a^\dagger \pi_{LU}\right) + \mathrm{i}\hbar \left(J_2 \pi_{14} - J_2^* \pi_{41}\right) \ , \end{aligned} \tag{6.3.3}$$

and moreover contains the coupling

$$\mathrm{H}_{\text{coupling}} = \hbar\varepsilon \left(a_1^\dagger a_2 + a_2^\dagger a_1\right) \ . \tag{6.3.4}$$

The mutual coupling rate between the modes ε depends on the distance between the micro-resonators. The term $\propto a_1^\dagger a_2$ describes a photon leaving the mode of the second laser and entering the mode of the first laser. In Eq. (6.3.3) we introduced the abbreviation $\pi_{ij} = |i_2\rangle \langle j_2|$. We assume here both QC lasers to be identical, i.e. $\omega_{m,1} = \omega_{m,2} = \omega_m$ etc. for all involved frequencies, $g_1 = g_2 = g$, and $J_1 = J_2 = J$. We again define all frequencies with respect to ω_l and transform to a frame rotating with ω_m, introducing the detunings $\Delta_u = \omega_u - \omega_m$, $\Delta_j = \omega_j - \omega_m$ with $j = 1, \ldots, 4$. The voltage applied to each QC laser can be adjusted individually, leading to the detunings $\Delta'_{u,1} = \Delta_u + \alpha V_{\text{ext},1}$ and $\Delta'_{u,2} = \Delta_u + \alpha V_{\text{ext},2}$. The carrier induced mode shift gives $\Delta'_{m,1} = \beta \left(\langle L_1 \rangle - \langle U_1 \rangle \right)$ and $\Delta'_{m,2} = \beta \left(\langle L_2 \rangle - \langle U_2 \rangle \right)$.

The Liouvillian describing dissipative processes in the second QC laser is defined analogously to Eq. (6.2.3). Thermal photons in the mode of the second micro cavity are denoted by m_j, the decay rates are denoted by μ_j, $j = 1, \ldots, 5$. The equations describing the first QC laser are

$$\begin{aligned}\frac{\mathrm{d}}{\mathrm{d}t} \langle U_1 \rangle =& g_1 \left(\left\langle a_1^\dagger \sigma_{LU} \right\rangle + \langle a_1 \sigma_{UL} \rangle \right) + \gamma_1 (n_1 + 1) \langle I_{1,1} \rangle \\ & - (\gamma_1 n_1 + \gamma_2 (n_2 + 1)) \langle U_1 \rangle + \gamma_2 n_2 \langle L_1 \rangle \ ,\end{aligned} \tag{6.3.5}$$

$$\begin{aligned}\frac{\mathrm{d}}{\mathrm{d}t} \langle L_1 \rangle =& - g_1 \left(\left\langle a_1^\dagger \sigma_{LU} \right\rangle + \langle a_1 \sigma_{UL} \rangle \right) + \gamma_2 (n_2 + 1) \langle U_1 \rangle \\ & - (\gamma_2 n_2 + \gamma_3 (n_3 + 1)) \langle L_1 \rangle + \gamma_3 n_3 \langle I_{2,1} \rangle \ ,\end{aligned} \tag{6.3.6}$$

$$\frac{\mathrm{d}}{\mathrm{d}t} \langle I_{1,1} \rangle = J_1^* \langle \sigma_{41} \rangle + J_1 \langle \sigma_{14} \rangle - \gamma_1 (n_1 + 1) \langle I_{1,1} \rangle + \gamma_1 n_1 \langle U_1 \rangle + r_{\text{in},1} \ , \tag{6.3.7}$$

$$\frac{\mathrm{d}}{\mathrm{d}t} \langle I_{2,1} \rangle = - (\gamma_3 n_3 + \gamma_4 (n_4 + 1)) \langle I_{2,1} \rangle + \gamma_4 n_4 \langle I_{3,1} \rangle + \gamma_3 (n_3 + 1) \langle L_1 \rangle \ , \tag{6.3.8}$$

$$\begin{aligned}\frac{\mathrm{d}}{\mathrm{d}t} \langle I_{3,1} \rangle =& - (\gamma_4 n_4 + \gamma_5 (n_5 + 1)) \langle I_{3,1} \rangle + \gamma_5 n_5 \langle I_{4,1} \rangle + \gamma_4 (n_4 + 1) \langle I_{2,1} \rangle \\ & - r_{\text{out},1} \langle I_{3,1} \rangle \ ,\end{aligned} \tag{6.3.9}$$

$$\frac{\mathrm{d}}{\mathrm{d}t} \langle I_{4,1} \rangle = - J_1 \langle \sigma_{14} \rangle - J_1^* \langle \sigma_{41} \rangle + \gamma_5 (n_5 + 1) \langle I_{3,1} \rangle - \gamma_5 n_5 \langle I_{4,1} \rangle \ , \tag{6.3.10}$$

$$\frac{\mathrm{d}}{\mathrm{d}t} \langle \sigma_{14} \rangle = J_1^* \left(\langle I_{4,1} \rangle - \langle I_{1,1} \rangle \right) - \frac{\gamma_1 (n_1 + 1)}{2} \langle \sigma_{14} \rangle \ , \tag{6.3.11}$$

and the second order terms

$$\begin{aligned}\frac{\mathrm{d}}{\mathrm{d}t} \langle a_1 \sigma_{UL} \rangle =& - g_1 \left(\left\langle a_1 a_1^\dagger \right\rangle \langle U_1 \rangle - \left\langle a_1^\dagger a_1 \right\rangle \langle L_1 \rangle \right) + \mathrm{i} \Delta'_{u,1} \langle a_1 \sigma_{UL} \rangle \\ & - \left(\kappa_1 + \frac{\gamma_1 n_1}{2} + \frac{\gamma_2 (2 n_2 + 1)}{2} + \frac{\gamma_3 (n_3 + 1)}{2} + \mathrm{i} \Delta'_{m,1} \right) \langle a_1 \sigma_{UL} \rangle \\ & - \mathrm{i} \varepsilon \langle a_2 \sigma_{UL} \rangle \ ,\end{aligned} \tag{6.3.12}$$

and

$$\begin{aligned}\frac{\mathrm{d}}{\mathrm{d}t}\left\langle a_1^\dagger a_1\right\rangle =& -g_1\left(\left\langle a_1\sigma_{UL}\right\rangle + \left\langle a_1^\dagger\sigma_{LU}\right\rangle\right) - 2\kappa_1\left\langle a_1^\dagger a_1\right\rangle + 2\kappa_1 n_2\\ &+ \mathrm{i}\varepsilon\left(\left\langle a_1 a_2^\dagger\right\rangle - \left\langle a_1^\dagger a_2\right\rangle\right)\ . \end{aligned} \tag{6.3.13}$$

The emission from each laser is proportional to the number of photons in the each mode.

The coupling to the second QC laser becomes apparent in Eq. (6.3.12) and Eq. (6.3.13). Equations for the quantities that emerge from the coupling are calculated below. The equations for the second QC laser are

$$\begin{aligned}\frac{\mathrm{d}}{\mathrm{d}t}\left\langle U_2\right\rangle =& g_2\left(\left\langle a_2^\dagger\pi_{LU}\right\rangle + \left\langle a_2\pi_{UL}\right\rangle\right) + \mu_1\left(m_1+1\right)\left\langle I_{1,2}\right\rangle\\ &-\left(\mu_1 m_1 + \mu_2\left(m_2+1\right)\right)\left\langle U_2\right\rangle + \mu_2 m_2\left\langle L_2\right\rangle\ ,\end{aligned} \tag{6.3.14}$$

$$\begin{aligned}\frac{\mathrm{d}}{\mathrm{d}t}\left\langle L_2\right\rangle =& -g_2\left(\left\langle a_2^\dagger\pi_{LU}\right\rangle + \left\langle a_2\pi_{UL}\right\rangle\right) + \mu_2\left(m_2+1\right)\left\langle U_2\right\rangle\\ &-\left(\mu_2 m_2 + \mu_3\left(m_3+1\right)\right)\left\langle L_2\right\rangle + \mu_3 m_3\left\langle I_{2,2}\right\rangle\ ,\end{aligned} \tag{6.3.15}$$

$$\frac{\mathrm{d}}{\mathrm{d}t}\left\langle I_{1,2}\right\rangle = J_2^*\left\langle\pi_{41}\right\rangle + J_2\left\langle\pi_{14}\right\rangle - \mu_1\left(m_1+1\right)\left\langle I_{1,2}\right\rangle + \mu_1 m_1\left\langle U_2\right\rangle + r_{\mathrm{in},2}\ , \tag{6.3.16}$$

$$\frac{\mathrm{d}}{\mathrm{d}t}\left\langle I_{2,2}\right\rangle = -\left(\mu_3 m_3 + \mu_4\left(m_4+1\right)\right)\left\langle I_{2,2}\right\rangle + \mu_4 m_4\left\langle I_{3,2}\right\rangle + \mu_3\left(m_3+1\right)\left\langle L_2\right\rangle\ , \tag{6.3.17}$$

$$\begin{aligned}\frac{\mathrm{d}}{\mathrm{d}t}\left\langle I_{3,2}\right\rangle =& -\left(\mu_4 m_4 + \mu_5\left(m_5+1\right)\right)\left\langle I_{3,2}\right\rangle + \mu_5 m_5\left\langle I_{4,2}\right\rangle + \mu_4\left(m_4+1\right)\left\langle I_{2,2}\right\rangle\\ &- r_{\mathrm{out},2}\left\langle I_{3,2}\right\rangle\ ,\end{aligned} \tag{6.3.18}$$

$$\frac{\mathrm{d}}{\mathrm{d}t}\left\langle I_{4,2}\right\rangle = -J_2\left\langle\pi_{14}\right\rangle - J_2^*\left\langle\pi_{41}\right\rangle + \mu_5\left(m_5+1\right)\left\langle I_{3,2}\right\rangle - \mu_5 m_5\left\langle I_{4,2}\right\rangle\ , \tag{6.3.19}$$

$$\frac{\mathrm{d}}{\mathrm{d}t}\left\langle\pi_{14}\right\rangle = J_2^*\left(\left\langle I_{4,2}\right\rangle - \left\langle I_{1,2}\right\rangle\right) - \frac{\mu_1\left(m_1+1\right)}{2}\left\langle\pi_{14}\right\rangle\ , \tag{6.3.20}$$

with the second order terms

$$\begin{aligned}\frac{\mathrm{d}}{\mathrm{d}t}\left\langle a_2\pi_{UL}\right\rangle =& -g_2\left(\left\langle a_2 a_2^\dagger\right\rangle\left\langle U_2\right\rangle - \left\langle a_2^\dagger a_2\right\rangle\left\langle L_2\right\rangle\right) + \mathrm{i}\Delta'_{u,2}\left\langle a_2\pi_{UL}\right\rangle\\ &-\left(\kappa_2 + \frac{\mu_1 m_1}{2} + \frac{\mu_2\left(2m_2+1\right)}{2} + \frac{\mu_3\left(m_3+1\right)}{2} + \mathrm{i}\Delta'_{m,2}\right)\left\langle a_2\pi_{UL}\right\rangle\\ &-\mathrm{i}\varepsilon\left\langle a_1\pi_{UL}\right\rangle\ ,\end{aligned} \tag{6.3.21}$$

and

$$\begin{aligned}\frac{\mathrm{d}}{\mathrm{d}t}\left\langle a_2^\dagger a_2\right\rangle = &-g_2\left(\langle a_2\pi_{UL}\rangle + \left\langle a_2^\dagger \pi_{LU}\right\rangle\right) - 2\kappa_2\left\langle a_2^\dagger a_2\right\rangle + 2\kappa_2 m_2 \\ &- \mathrm{i}\varepsilon\left(\left\langle a_1 a_2^\dagger\right\rangle - \left\langle a_1^\dagger a_2\right\rangle\right) \ .\end{aligned} \tag{6.3.22}$$

The coupling requires the introduction of the equation for $\left\langle a_1^\dagger a_2\right\rangle$ which reads

$$\begin{aligned}\frac{\mathrm{d}}{\mathrm{d}t}\left\langle a_1^\dagger a_2\right\rangle = &-g_1\langle a_2\sigma_{UL}\rangle - g_2\left\langle a_1^\dagger \pi_{LU}\right\rangle \\ &- \left(\mathrm{i}\Delta'_{m,2} - \mathrm{i}\Delta'_{m,1} + \kappa_1 + \kappa_2\right)\left\langle a_1^\dagger a_2\right\rangle \\ &+ \mathrm{i}\varepsilon\underbrace{\left(\left\langle a_1 a_1^\dagger a_2^\dagger a_2\right\rangle - \left\langle a_1^\dagger a_1 a_2 a_2^\dagger\right\rangle\right)}_{\left(\left\langle a_2^\dagger a_2\right\rangle - \left\langle a_1^\dagger a_1\right\rangle\right)} \ ,\end{aligned} \tag{6.3.23}$$

which quantifies the exchange of photons between the modes. Photons can also be emitted by one structure and directly enter the cavity of the second structure. This processes are described by

$$\begin{aligned}\frac{\mathrm{d}}{\mathrm{d}t}\langle a_2\sigma_{UL}\rangle = &-\left(\mathrm{i}\Delta'_{m,2} - \mathrm{i}\Delta'_{u,1}\right)\langle a_2\sigma_{UL}\rangle \\ &- \left(\kappa_2 + \frac{\gamma_1 n_1}{2} + \frac{\gamma_2\left(2n_2+1\right)}{2} + \frac{\gamma_3\left(n_3+1\right)}{2}\right)\langle a_2\sigma_{UL}\rangle \\ &- g_2\langle\sigma_{UL}\pi_{LU}\rangle - g_1\left(\langle U_1\rangle - \langle L_1\rangle\right)\left\langle a_1^\dagger a_2\right\rangle \\ &- \mathrm{i}\varepsilon\langle a_1\sigma_{UL}\rangle\end{aligned} \tag{6.3.24}$$

and

$$\begin{aligned}\frac{\mathrm{d}}{\mathrm{d}t}\langle a_1\pi_{UL}\rangle = &-\left(\mathrm{i}\Delta'_{m,1} - \mathrm{i}\Delta'_{u,2}\right)\langle a_1\pi_{UL}\rangle \\ &- \left(\kappa_1 + \frac{\mu_1 m_1}{2} + \frac{\mu_2\left(2m_2+1\right)}{2} + \frac{\mu_3\left(m_3+1\right)}{2}\right)\langle a_1\pi_{UL}\rangle \\ &- g_1\langle\pi_{UL}\sigma_{LU}\rangle - g_2\left(\langle U_2\rangle - \langle L_2\rangle\right)\left\langle a_2^\dagger a_1\right\rangle \\ &- \mathrm{i}\varepsilon\langle a_2\pi_{UL}\rangle \ .\end{aligned} \tag{6.3.25}$$

Correlations between the structures $\langle\sigma_{UL}\pi_{LU}\rangle$ emerge as a result of the interaction.

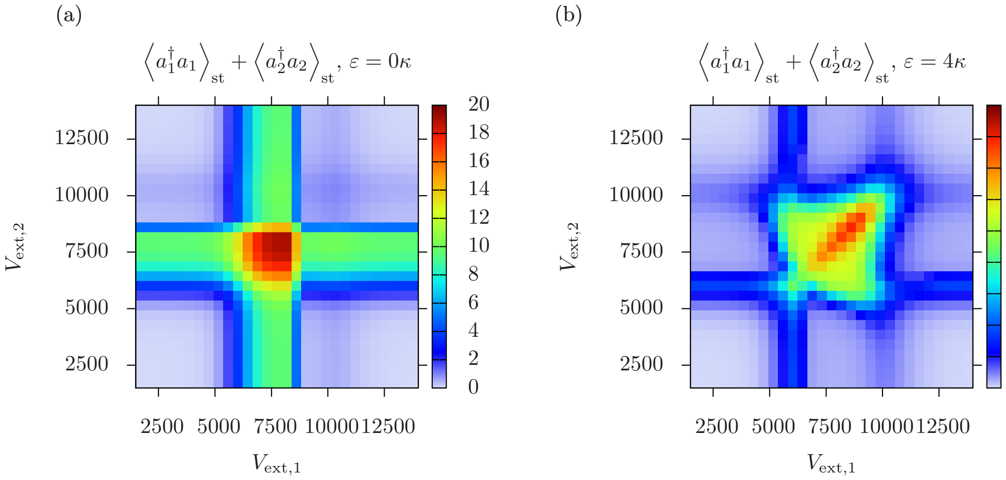

Figure 6.5.: Sum of the steady state photon number in both modes $\left\langle a_1^\dagger a_1 \right\rangle_{\mathrm{st}} + \left\langle a_2^\dagger a_2 \right\rangle_{\mathrm{st}}$ as a function of the individual pumping rates $V_{\mathrm{ext},1}$, and $V_{\mathrm{ext},2}$ at $T = 0.1$ K. In (a) the two lasers are uncoupled as $\varepsilon = 0$, resulting in the mere addition of both emission patterns. In (b) the coupling is set to $\varepsilon = 4\kappa$. The coupled lasers show mutual blockade: To obtain a significant number of photons both lasers must be in their working voltage range, which corresponds to a logical AND operation. The parameters for each laser are chosen as in Fig. 6.3.

This equation

$$\begin{aligned}\frac{\mathrm{d}}{\mathrm{d}t}\left\langle \sigma_{UL}\pi_{LU}\right\rangle &= -g_1\left(\langle U_1\rangle - \langle L_1\rangle\right)\left\langle a_1^\dagger \pi_{LU}\right\rangle - g_2\left(\langle U_2\rangle - \langle L_2\rangle\right)\left\langle a_2\sigma_{UL}\right\rangle \\ &\quad + \mathrm{i}\left(\Delta'_{u,1} - \Delta'_{u,2}\right)\left\langle \sigma_{UL}\pi_{LU}\right\rangle - \left(\frac{\gamma_1 n_1}{2} + \frac{\gamma_2\left(2n_2+1\right)}{2} + \frac{\gamma_3\left(n_3+1\right)}{2}\right. \\ &\quad \left. + \frac{\mu_1 m_1}{2} + \frac{\mu_2\left(2m_2+1\right)}{2} + \frac{\mu_3\left(m_3+1\right)}{2}\right)\left\langle \sigma_{UL}\pi_{LU}\right\rangle , \qquad (6.3.26)\end{aligned}$$

is the last necessary to obtain a closed set because all expectation values in Eq. (6.3.26) are already collected. Numerical integration yields the steady state behavior of the coupled QC lasers. To be consistent with the experiment we assume that the detected emission cannot be assigned to a single laser but is proportional to the sum $\left\langle a_1^\dagger a_1 \right\rangle_{\mathrm{st}} + \left\langle a_2^\dagger a_2 \right\rangle_{\mathrm{st}}$.

With increasing strength ε of the mutual coupling the emission pattern of the QC lasers changes. In Fig. 6.5 the number of photons in both modes is depicted for the case of uncoupled lasers (a) and for the coupling rate $\varepsilon = 4\kappa$ (b). For the uncoupled lasers the photon number is simply added. The lasing regions of both lasers are visible as vertical and horizontal features that cross for $V_{\mathrm{ext},1} = V_{\mathrm{ext},2} = 8000$. The

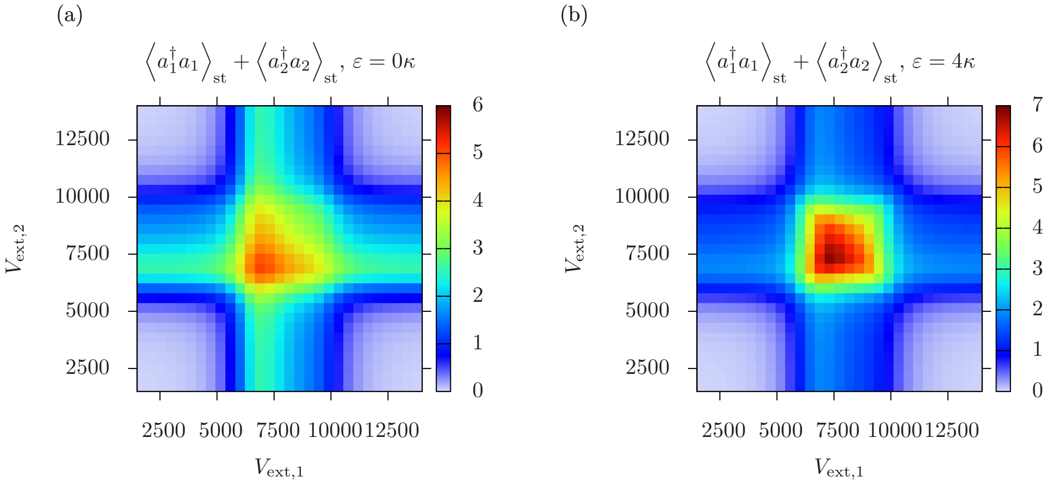

Figure 6.6.: Sum of the steady state photon number in both modes $\langle a_1^\dagger a_1 \rangle_{st} + \langle a_2^\dagger a_2 \rangle_{st}$ as a function of the individual pumping rates $V_{ext,1}$, and $V_{ext,2}$ at a significantly higher temperature $T = 1$ K. The overall emission is reduced but the blocking mechanism is still present.

emission profile of each laser corresponds to a section across Fig. 6.3 at $T = 0.1$ K. For the coupled lasers the common lasing region is restricted to the area where both lasers are active. This corresponds to a logical AND operation, and has also been demonstrated experimentally [6.5].

For $T = 1$ K the emission profile of each laser is deformed and the output power is reduced, as already visible in Fig. 6.3. However, the behavior of mutual blockade is preserved. In conclusion we find that the simplified model we developed for the description of single and coupled cascade lasers is able to simulate some aspects of the behavior found in experiments.

In the following section we study how the temperature of the environment can be employed as part of the structure design.

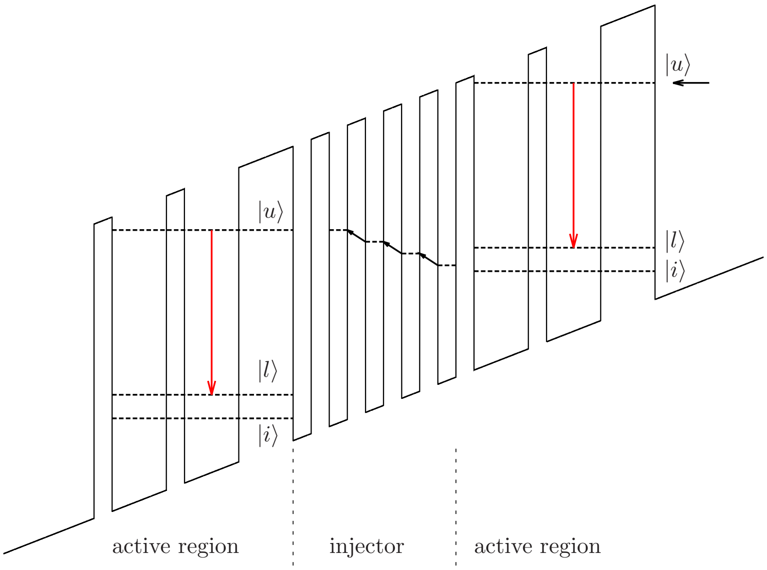

Figure 6.7.: Schematic representation a quantum well structure with absorptive steps in the injector region. The injector region contains several energy levels which are arranged such that several phonons must be absorbed in order to pass the structure. The absorption processes are indicated by black arrows.

6.4. Suppression of heating and alternative pumping schemes

So far the inversion necessary for laser action has been accomplished by electrical pumping of the semiconductor structure. The emission of photons is proportional to the current that runs through the material. Reverting this process naturally gives rise to a so-called intersubband photo detector. A photon excites an electron that can tunnel into the next well from where it relaxes predominantly into the next active region of the structure, leading to a measurable photo current. The interesting point of such detectors is that they could allow for fast photo detection in frequency ranges where no suitable intraband semiconductor photo detectors are available [6.7].

Following this idea, a modified design for QC lasers can be envisaged which to some extend reduces the problem of heating in conventional QC lasers. Phonon emission during the passage of carriers through the injector region causes heating of the device. Finally the QC laser ceases to work due to the heating. In a modified scheme, depicted in Fig. 6.7, the injector region could be designed to contain absorptive steps, leading to a situation where the absorption of a phonon (or several phonons) is required in each quantum well structure. The resulting design is therefore a combination between cascade lasers studied in Sec. 6.2 and the above described intersubband photo detector. Due to the absorptive steps a minimal temperature is required to allow for the transfer through the injector. There is still an upper temperature limit above which lasing is impossible. However, if heating is suppressed during operation, higher currents and therefore higher output powers should be possible before the heating becomes detrimental.

Elaborating on this basic idea of absorptive steps we propose a model in which thermal intersubband excitations are employed as a pump mechanism. A sustained spatial temperature gradient across a quantum well structure takes the role that spectral shaping plays in conventional lasers. The efficiency of such systems, where lasing and pumping transition are kept at different temperatures, has been widely studied [6.8, 6.9]. In Sec. 7 the basic principles of the temperature gradient pumping scheme are introduced. The model is then extended to include an extra absorptive step in the cold region of the device to demonstrate the above discussed suppression of heating.

References for Chapter 6

[6.1] J. Faist et al. “Quantum cascade laser.” In: *Science* 264.5158 (1994), pp. 553–556.

[6.2] C. Gmachl et al. “Recent progress in quantum cascade lasers and applications.” In: *Reports on progress in physics* 64 (2001), p. 1533.

[6.3] H.G. Schuster and K. Lüdge. *Nonlinear Laser Dynamics-From Quantum Dots to Cryptography*. Vol. 8. Wiley-VCH, 2012.

[6.4] G. Fasching et al. “Terahertz microcavity quantum-cascade lasers.” In: *Applied Physics Letters* 87 (2005), p. 211112.

[6.5] G. Fasching et al. “Electrically Switchable Photonic Molecule Laser.” In: *Arxiv preprint arXiv:0907.1932* (2009).

[6.6] K. Unterrainer et al. “Quantum cascade lasers with double metal-semiconductor waveguide resonators.” In: *Applied physics letters* 80 (2002), p. 3060.

[6.7] F.R. Giorgetta et al. “Quantum Cascade Detectors.” In: *Quantum Electronics, IEEE Journal of* 45.8 (2009), pp. 1039–1052.

[6.8] H.E.D. Scovil and E.O. Schulz-DuBois. "Three-level masers as heat engines." In: *Physical Review Letters* 2.6 (1959), pp. 262–263.

[6.9] E. Boukobza and D.J. Tannor. "Three-level systems as amplifiers and attenuators: A thermodynamic analysis." In: *Physical review letters* 98.24 (2007), p. 240601.

7. Preprint

PREPRINT

Temperature gradient driven lasing and stimulated cooling[†]

Kathrin Sandner[1], Helmut Ritsch[1]

[1] *Institute for Theoretical Physics, University of Innsbruck*
Technikerstr. 25, 6020 Innsbruck, Austria

A laser can be understood as thermodynamic engine converting heat to a coherent single mode field close to Carnot efficiency. To achieve lasing, spectral shaping of the excitation light is used to generate a higher effective temperature on the pump than on the gain transition. Here, using a toy model of a quantum well structure with two suitably designed tunnel-coupled wells kept at different temperature, we predict that lasing can also occur on an actual spatial temperature gradient between pump and gain region. Gain and narrow band laser emission require a sufficiently large temperature gradient and resonator quality. Lasing appears concurrent with amplified heat flow between the reservoirs and points to a new form of stimulated solid state cooling. In addition, such a mechanism could reduce intrinsic heating and thus extend the operating regime of quantum cascade lasers by substituting phonon emission driven injection by a phonon absorption step.

PACS numbers: 42.50.Pq,42.55.Sa,42.55.Ah

Lasing occurs for sufficient gain within an optical resonator, which for stimulated emission based amplification requires an inverted populations between the amplifier levels [7.1]. In theoretical models pumping to generate inversion is described by coupling reservoirs of different temperature to pump, injection and lasing transitions [7.2–7.5]. Practical implementation requires precise spectral design of the pump radiation to overlap well with the pump transition with strong suppression of thermal radiation on lasing and injection transitions. At optical frequencies with

---

[†] The author of the present thesis performed all of the calculations in this preprint.

almost no thermal photons present, filtering of the pump light is sufficient to achieve this. However, spectral shaping in the far infrared or even THz regime is practically hampered by ubiquitous thermal quanta, which create strong restrictions on the laser operating temperature [7.6].

In this paper we exhibit possible routes to directly use spatial temperature gradients instead of spectral pump design to generate inversion and facilitate gain and lasing. While we mostly concentrate on basic principles and mechanisms, we also discuss a possible real world implementation based on designed quantum well structures. Here the optical properties and level structures in the far infrared or even THz regime can be precisely engineered. While such a temperature gradient laser at first seems more of conceptual than of practical importance, the underlying principle can exploited by adding an extra pump step to a conventional semiconductor laser setup. Adding thermal or phonon absorption based injection steps before the gain transition leads to a useful modification of the thermal operation conditions. Lasing then can be tied to heat absorption or directional energy flow to reduce excess heating and steer heat flow [7.7]. As prove of principle we study a simple structure of two tunnel coupled quantum wells at different temperature as sketched in Fig. 7.1. A single high Q cavity mode is coupled to a gain transition in the right well kept at low temperature. A model Hamiltonian $\mathrm{H} = \mathrm{H}_0 + \mathrm{H}_\mathrm{I}$ for a system of N parallel two-well structures and a single mode reads

$$\mathrm{H}_0 = \hbar\omega_m a^\dagger a + \hbar \sum_{j=1}^{N} \Big[\omega_u \left|u_j\right\rangle \left\langle u_j\right| + \omega_l \left|l_j\right\rangle \left\langle l_j\right| + \sum_{k=1}^{4} \omega_{I_k} \left|I_{k,j}\right\rangle \left\langle I_{k,j}\right| \Big] \tag{7.0.1}$$

and

$$\mathrm{H}_\mathrm{I} = \hbar g \sum_{j=1}^{N} \Big(a\sigma_j^+ + a^\dagger \sigma_j^- \Big) + \hbar \sum_{j=1}^{N} \left(J_1 \left|I_{4,j}\right\rangle \left\langle I_{3,j}\right| + J_2 \left|I_{2,j}\right\rangle \left\langle I_{1,j}\right| + h.c. \right) \ , \tag{7.0.2}$$

where $\sigma_j^+ = \left|u_j\right\rangle \left\langle l_j\right|$. The energy eigenstates are denoted by $\left|I_{1,j}\right\rangle, \ldots, \left|I_{4,j}\right\rangle$, $\left|u_j\right\rangle$ and $\left|l_j\right\rangle$ with the energies $\hbar\omega_{I_1}, \ldots, \hbar\omega_{I_4}$, $\hbar\omega_u$ and $\hbar\omega_l$. $a^\dagger$ is the creation operator for a cavity photon at frequency ω_m. Note that the structures do not form a cascade and interact only via the common cavity mode. The coupling between the $u \to l$ transition and the mode is described by the coupling rate g. Tunneling between the states $\left|I_{1,j}\right\rangle$ and $\left|I_{2,j}\right\rangle$ and the states $\left|I_{3,j}\right\rangle$ and $\left|I_{4,j}\right\rangle$ is described by the matrix elements J_1 and J_2. For the forthcoming analysis we define all frequencies relative to ω_l and switch to a frame rotating with ω_m with detuning $\Delta_u = \omega_u - \omega_m$. The dynamics of the reduced density matrix is described by the master equation $\frac{\mathrm{d}}{\mathrm{d}t}\rho = (\mathrm{i}/\hbar)\left[\rho, \mathrm{H}\right] + \mathcal{L}\left[\rho\right]$, including the coupling to the environment at finite temperature

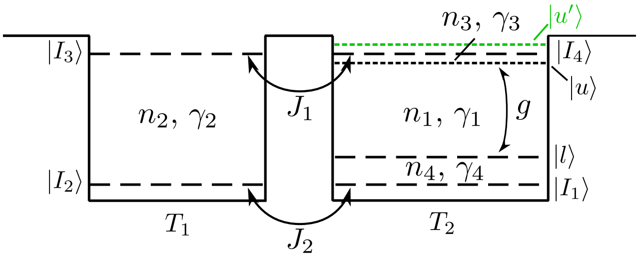

Figure 7.1.: (Color online) Sketch of the two-well structure and the energy levels. The wave functions are assumed to be well localized in each well while the coupling is described by the tunneling constants J_1 and J_2. An alternative design including an absorptive step between $|I_4\rangle$ and $|u'\rangle$ is indicated in green.

(see supplementary material). The decay rate of the cavity is denoted by κ and the spontaneous emission rates are denoted by $\gamma_1, \ldots, \gamma_4$. The thermal photon number at the transition frequencies $\omega_1 = \omega_u - \omega_l$, $\omega_2 = \omega_{I_3} - \omega_{I_2}$, $\omega_3 = \omega_{I_4} - \omega_u$ and $\omega_4 = \omega_l - \omega_{I_1}$ at temperature T is denoted by $n_i(T)$ $(i = 1, \ldots, 4)$.

We assume to have a sustained temperature difference between the two wells with $T_1 > T_2$. As $T_1 \neq 0$ electrons will be thermally excited to state $|I_3\rangle$ and tunnel to state $|I_4\rangle$, which couples radiatively or via phonons to the upper laser level $|u\rangle$. Eventually a photon is created in the cavity by a transition to the lower laser level $|g\rangle$ and the cycle then ends with the tunneling from state $|I_1\rangle$ to $|I_2\rangle$. For appropriate parameters this cycle creates gain and lasing.

Mathematically we use the master equation to get equations for the population expectation values in each state and the quantities they couple to [7.8], which we truncate to include only second order correlation functions. For the central quantity of the number of photons this gives

$$\frac{\mathrm{d}}{\mathrm{d}t}\left\langle a^\dagger a\right\rangle = -2\kappa\left\langle a^\dagger a\right\rangle + 2\kappa n_1 - \mathrm{i}gN\left(\left\langle a^\dagger\sigma_j^-\right\rangle - \left\langle a\sigma_j^+\right\rangle\right) ,$$

which contains the intuitive expected loss term, a heating term from thermal photons and the stimulated emission term to provide gain. The latter has to be determined from:

$$\begin{aligned}\frac{\mathrm{d}}{\mathrm{d}t}\left\langle a\sigma_j^+\right\rangle = \mathrm{i}\Delta_u\left\langle a\sigma_j^+\right\rangle - \mathrm{i}g\left(N-1\right)\left\langle\sigma_j^-\sigma_k^+\right\rangle \\ - \mathrm{i}g\left(\left[1+\left\langle a^\dagger a\right\rangle\right]\left\langle\left|u_j\right\rangle\left\langle u_j\right|\right\rangle - \left\langle a^\dagger a\right\rangle\left\langle\left|l_j\right\rangle\left\langle l_j\right|\right\rangle\right) \\ - \left(\kappa + \gamma_1\left(2n_1+1\right) + \gamma_3 n_3 + \gamma_4\left(n_4+1\right)\right)\left\langle a\sigma_j^+\right\rangle, \quad (7.0.3)\end{aligned}$$

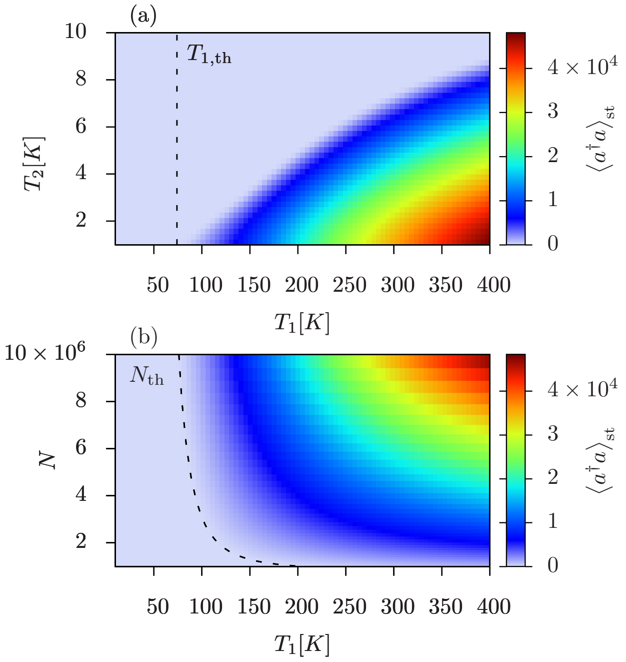

Figure 7.2.: (Color online) (a) Numerical solution for the steady state number of photons $\left\langle a^\dagger a\right\rangle_{\mathrm{st}}$ in the cavity as a function of T_1 and T_2 for $N = 10^7$. The dashed line indicates a minimum $T_{1,\mathrm{th}}$ for cooperative behavior (valid for T_2 small enough to set $n_1 = n_3 = n_4 = 0$). (b) $\left\langle a^\dagger a\right\rangle_{\mathrm{st}}$ as a function of T_1 and N ($T_2 = 0.1$ K). The analytical solution gives $N_{\mathrm{th}}\,(T_1)$ (dashed line) and reliably predicts the onset of cooperative behavior and a significant increase in $\left\langle a^\dagger a\right\rangle_{\mathrm{st}}$.

which describes the rate at which excitations are transferred between the cavity and the structure. Fortunately, global phase invariance ($\langle a\rangle = \left\langle \sigma_j^+\right\rangle = 0$) can be used to simplify third order expectation values [7.9, 7.10]. In the second term of Eq. (7.0.3) we see, that cooperative effects emerge as a result of common interaction with the cavity mode. Explicitly we find

$$\begin{aligned}\frac{\mathrm{d}}{\mathrm{d}t}\left\langle \sigma_j^-\sigma_k^+\right\rangle = &-\left(2\gamma_1\left(2n_1+1\right)+2\gamma_3 n_3+2\gamma_4\left(n_4+1\right)\right)\left\langle \sigma_j^-\sigma_k^+\right\rangle \\ &-\mathrm{i}g\left[\left(\left\langle a^\dagger\sigma_j^-\right\rangle-\left\langle a\sigma_j^+\right\rangle\right)\left(\langle |u_j\rangle\langle u_j|\rangle-\langle |l_j\rangle\langle l_j|\rangle\right)\right]\ . \qquad (7.0.4)\end{aligned}$$

To complete a selfcontained set we still need equations for the populations and polarizations: $\langle |u_j\rangle\langle u_j|\rangle$, $\langle |l_j\rangle\langle l_j|\rangle$, $\langle |I_{i,j}\rangle\langle I_{i,j}|\rangle$ $(i = 1,2,3,4)$, $\langle |I_{1,j}\rangle\langle I_{2,j}|\rangle$ and $\langle |I_{3,j}\rangle\langle I_{4,j}|\rangle$. This nonlinear set of equations can be solved numerically for the steady state properties of our laser as shown in the following figures. In addition, under the assumption of very small T_2, so that $n_1 = n_3 = n_4 \approx 0$ and resonance

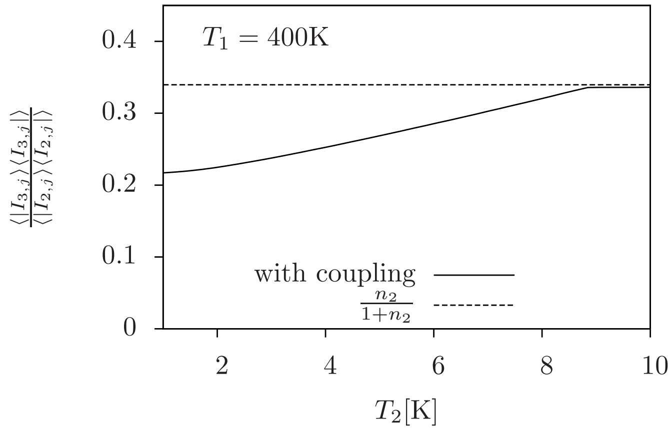

Figure 7.3.: Occupation ratio in the first quantum well for the coupled and uncoupled case versus T_2. The temperature of the hot part T_1 is fixed to 400 K. For $T_2 < 9$ K we see a reduction of $\langle |I_{3,j}\rangle \langle I_{3,j}|\rangle \,/\, \langle |I_{2,j}\rangle \langle I_{2,j}|\rangle$ (solid line) compared to the uncoupled case (dashed line).

$\Delta_u = 0$, an approximate analytical solution can be found to give extra insight into the central mechanisms present [7.10]. In the bad cavity regime, keeping only the decay term proportional to κ and the second term of Eq. (7.0.3), where we approximate $N-1 \approx N$, we obtain the steady-state $\left\langle a\sigma_j^+ \right\rangle_{\text{st}} = -\frac{igN}{\kappa} \left\langle \sigma_j^- \sigma_k^+ \right\rangle_{\text{st}}$. Actually for large longitudinal mode spacing of tiny cavities as often used in cascade lasers even a high finesse still gives a larger decay rate κ as compared to optical transition rates in the wells. Using the approximate solution for $\left\langle a\sigma_j^+ \right\rangle_{\text{st}}$, an approximate steady state for the whole set can be found. Here the steady state correlation between the structures $\left\langle \sigma_j^- \sigma_k^+ \right\rangle_{\text{st}}$ is of particular interest. It shows for which parameters the formation of cooperative interaction with the mode is possible [7.10]. For a given number of structures N we can calculate the critical temperature $T_{1,\text{th}}$ that is necessary to meet this condition: $(\left\langle \sigma_j^- \sigma_k^+ \right\rangle_{\text{st}} > 0)$. Analogously, T_1 determines the threshold number N_{th} of structures necessary for lasing as shown in the supplementary material.

The equations can also solved numerically for the steady state and compared to our approximate solutions. The parameters $\kappa = 2\pi \times 5 \times 10^5$ Hz (i.e. FWHM linewidth of 1 MHz), $g = (\kappa/3) \times 10^{-3}$, $\Delta_u = 0$,$\gamma_1 = 2\pi \times 4 \times 10^2$ Hz, $\gamma_2 = \gamma_3 = \gamma_4 = \gamma_1 \times 10^2$, $\omega_1 = 2\pi \times 7.9$ THz, $\omega_2 = 2\pi \times 9$ THz, $\omega_3 = 2\pi \times 0.1$ THz, $\omega_4 = 2\pi \times 1$ THz remain fixed for the forthcoming calculations, while N, T_1 and T_2 are varied. The number of photons as a function of T_1 and T_2 for $N = 10^7$ is shown in Fig. 7.2(a). The occupation of the cavity mode strongly depends on the temperature gradient between the wells. The approximative analytical treatment for small T_2 gives the threshold temperature $T_{1,\mathrm{th}}$ that signals the onset of cooperative behavior. For $T_2 > 1$ K the approximative solutions break down. In Fig. 7.2(b) we show $\left\langle a^\dagger a \right\rangle_{\mathrm{st}}$ as a function of T_1 and N for fixed $T_2 = 0.1$ K. Here, the approximative analytical solutions give a reliable result for which parameters to expect a high number of photons in the cavity. The numerical solutions show that the number of photons in the cavity increases rapidly as soon as we exceed N_{th} for a given value of T_1.

We have seen that a sufficient temperature difference between the layers results in a high population of the cavity mode and eventually lasing. Thus photons are emitted from the cavity at rate $2\kappa \left\langle a^\dagger a \right\rangle$ and energy is extracted from the system. From a different viewpoint this suggests that the cavity can serve as a channel for cooling. To show this we compare the level excitation ratio in the hot well with and without the cavity/laser present. Without lasing and tunneling $J_1 = J_2 = 0$ we find that the ratio between the upper level I_3 and the lower energy level I_2 in the first well to be $n_2/(1 + n_2)$. In the presence of the second well and in the lasing regime this ratio will be significantly reduced, indicating a lower effective temperature and enhanced heat flow. Figure 7.3 shows how the ratio $\langle |I_{3,j}\rangle \langle I_{3,j}|\rangle \,/\, \langle |I_{2,j}\rangle \langle I_{2,j}|\rangle$ changes with T_2 while $T_1 = 400$ K, and hence n_2, remains fixed. While T_2 remains low enough to ensure a significant number of photons in the cavity, and hence a considerable dissipation via the cavity mirrors, the occupation ratio in the first well is reduced. This corresponds to an effectively lower temperature of the first well. Note that we have neglected other forms of heat flow in the system which could be significant but here would only change the reference point of the curves.

As we have seen, we obtain a large number of photons in the cavity for $N > N_{\mathrm{th}}(T_1)$ and an appropriate temperature gradient $T_1 < T_2$, which can therefore be seen as an effective pump. To show that we indeed have lasing we still need to characterize the emission spectrum of the cavity output field and in particular its linewidth. Using the quantum regression theorem we obtain the differential equation for the first order correlation function $\left\langle a^\dagger (t+\tau)\, a(t) \right\rangle$ and $\left\langle \sigma_j^+ (t+\tau)\, a(t) \right\rangle$, see supplementary material. To find the spectrum we calculate the Laplace transform of the coupled equations [7.11]. The steady state values of the involved quantities are obtained numerically. In Fig. 7.4 the linewidth (FWHM) of the cavity output spectrum is depicted. With the onset of cooperative behavior the linewidth is reduced dramatically, which is a clear signature of sustained coherent oscillation. Similar behavior is found for fixed T_2 and varying T_1 and N. Using some algebra the laser linewidth above threshold can be analytically approximated by

$$\Delta f = \frac{\kappa\Gamma}{\kappa + \Gamma}\left[1 - \frac{g^2 N}{\kappa\Gamma} D\right] , \tag{7.0.5}$$

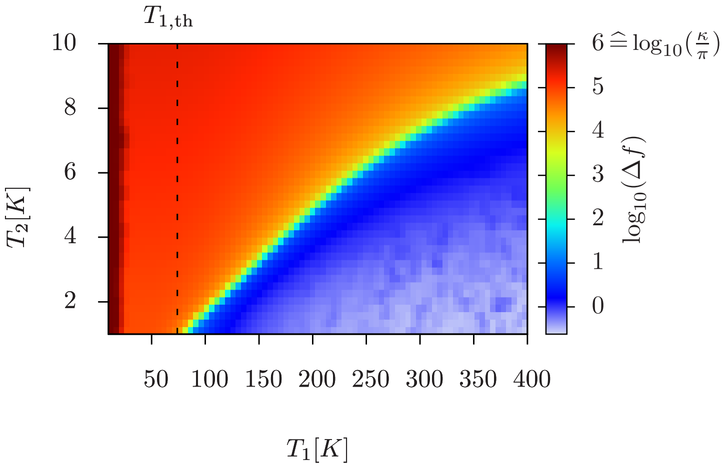

Figure 7.4.: (Color online) Linewidth of the cavity output spectrum for varying T_1 and T_2 with $N = 10^7$ (plotted on a logarithmic scale). The linewidth (FWHM) of the empty cavity $2\frac{\kappa}{2\pi} = 1$ MHz corresponds to the dark red color (upper boundary of the scale). The linewidth Δf falls slightly below that limit with increasing T_1 until it finally drops off dramatically as the cooperative effects emerge. For small T_2 the onset of cooperative behavior is marked by $T_{1,\mathrm{th}}$.

with the abbreviations

$$D = \left(\langle |u_j\rangle \langle u_j|\rangle_{\mathrm{st}} - \langle |l_j\rangle \langle l_j|\rangle_{\mathrm{st}}\right) \ ,$$

and

$$\Gamma = \gamma_3 n_3 \left(T_2\right) + \gamma_1 \left(2n_1 \left(T_2\right) + 1\right) + \gamma_4 \left(n_4 \left(T_2\right) + 1\right) \ .$$

The prefactor nicely exhibits the two limits of a good cavity or bad cavity configuration, where the linewidth is fixed by the less damped oscillator, while the second term shows lasing and gain induced linewidth narrowing.

The two-well system discussed above clearly exhibits the essential physical mechanism of heat to coherent light conversion. In the following we show that the very same principle can be extended to a multi step excitation processes, where a heat absorbing step leads to operation at higher emission frequencies and counteracts the heating processes. Replacing one of the absorbing steps by conventional pumping should reduce the temperature gradient requirements, but we refrain from a discussion of this mixed model here.

Formally a reduction of heating can be easily facilitated by incorporating an absorptive step in the second well and choosing $\omega_u' > \omega_{l_4}$. We indicated this possibility

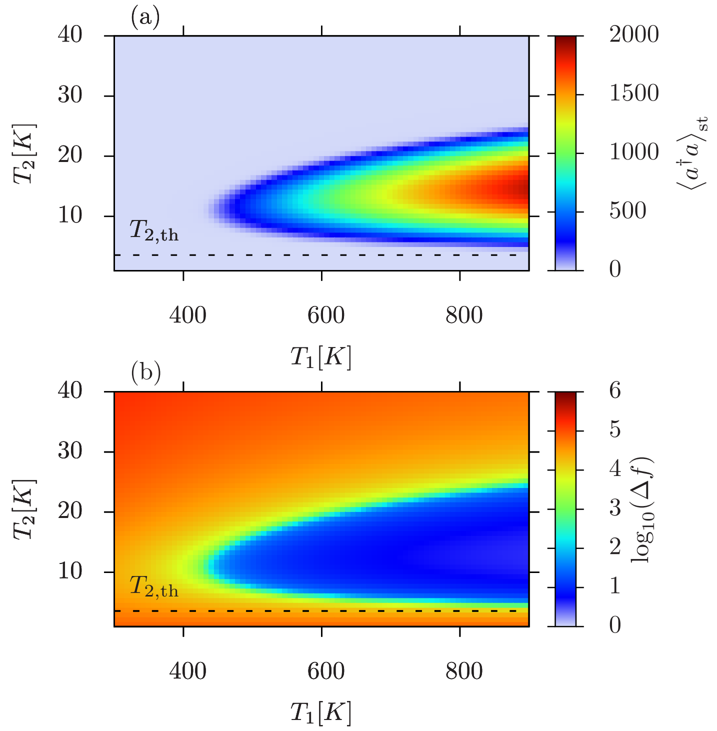

Figure 7.5.: (Color online) (a) Number of photons in the mode versus T_1 and T_2. For $T_2 > T_{2,\mathrm{th}}$ we find a sudden increase in $\left\langle a^\dagger a \right\rangle_{\mathrm{st}}$, and in (b) a corresponding drop in the linewidth of the cavity emission. This is due to the absorptive step in the revised model where $\omega_u' = \omega_u + 2\pi \times 0.05$ THz. The remaining parameters are unchanged except for $\gamma_3 = \gamma_1 = 2\pi \times 4 \times 10^2$ Hz.

(extra level $|u'\rangle$ in green) in Fig. 7.1. In the dissipative model dynamics we then simply have to exchange the rates $\gamma_3 n_3 (T_2) \leftrightarrow \gamma_3 (n_3 (T_2) + 1)$. Physically, this means that in each pump and stimulated emission cycle the absorption of an extra thermal photon or phonon with frequency $\omega_u' - \omega_{I_4}$ is necessary. On the one hand this implies that we find a minimal temperature below which not enough phonons are present to close the pump cycle and generate gain. On the other hand lasing is tied to heat absorption. In general one could of course consider a balanced combination of thermally assisted and externally driven excitation steps to optimize the operation regime. We will refrain from this here to keep the complexity of the model limited. Let us look at the results now. The temperature range for which $\left\langle a^\dagger a \right\rangle_{\mathrm{st}}$ becomes significant is depicted in Fig. 7.5(a). The dashed line marks the critical temperature necessary for cooperative behavior for similar approximations as described above. The linewidth of the emission in Fig. 7.5(b) shows distinctive narrowing in the lasing region. Extra phonon absorbing steps could be also added to conventional quantum well lasers, which generate intrinsic heating during operation to counteract the heating process.

Our theoretical calculations exhibit the possibility to use a spatial temperature gradient in a suitable active medium to induce optical gain and lasing. While not very practicable in the visible regime, a semiconductor heterostructure can be envisaged to generate narrow bandwidth emission through a resonant cavity mode in the THz regime, where the coherent emission of photons is sustained by a spatial temperature gradient. The effective extraction of thermal energy from the system in parallel provides for stimulated cooling of the first, hot quantum well. To use a similar idea at higher frequencies without too high temperatures, a multi step excitation process can be envisaged, where some steps could also invoke optical pumping or current injection. In general, introducing an absorptive step well before carrier injection to the upper laser level relies on absorption of thermal quanta and therefore counteracts heating during operation. While we here only worked with an oversimplified generic model, the physical principles behind should stay valid for more realistic and thus more complex descriptions. In addition, transverse spatial temperature gradients or even spatially separated structures connected by conducting wires might provide for alternative configurations at greater length scales.

K.S. was supported by the DOC-fFORTE doctoral program of the ÖAW. H.R. acknowledges support from the Austrian Science Fund FWF grant S4013.

Supplementary material

Liouvillian

The Liouvillian that describes dissipative processes, including the coupling of the cavity and the structures to the environment at finite temperature, reads

$$\begin{aligned}\mathcal{L}\left[\rho\right] = \kappa\left(n_1\left(T_2\right)+1\right)\left(2a\rho a^\dagger - a^\dagger a\rho - \rho a^\dagger a\right) + \kappa n_1\left(T_2\right)\left(2a^\dagger\rho a - aa^\dagger\rho - \rho aa^\dagger\right)\\ + \gamma_1\left(n_1\left(T_2\right)+1\right)\sum_j\left(2\sigma_j^-\rho\sigma_j^+ - \left|u_j\right\rangle\left\langle u_j\right|\rho - \rho\left|u_j\right\rangle\left\langle u_j\right|\right)\end{aligned}$$

$$
\begin{aligned}
&+ \gamma_1 n_1 (T_2) \sum_j \Big(2\sigma_j^+ \rho \sigma_j^- - |l_j\rangle \langle l_j| \rho - \rho |l_j\rangle \langle l_j|) \\
&+ \gamma_2 (n_2 (T_1) + 1) \sum_j (2 |I_{2,j}\rangle \langle I_{3,j}| \rho |I_{3,j}\rangle \langle I_{2,j}| - |I_{3,j}\rangle \langle I_{3,j}| \rho - \rho |I_{3,j}\rangle \langle I_{3,j}|) \\
&+ \gamma_2 n_2 (T_1) \sum_j (2 |I_{3,j}\rangle \langle I_{2,j}| \rho |I_{2,j}\rangle \langle I_{3,j}| - |I_{2,j}\rangle \langle I_{2,j}| \rho - \rho |I_{2,j}\rangle \langle I_{2,j}|) \\
&+ \gamma_3 (n_3 (T_2) + 1) \sum_j (2 |u_j\rangle \langle I_{4,j}| \rho |I_{4,j}\rangle \langle u_j| - |I_{4,j}\rangle \langle I_{4,j}| \rho - \rho |I_{4,j}\rangle \langle I_{4,j}|) \\
&+ \gamma_3 n_3 (T_2) \sum_j (2 |I_{4,j}\rangle \langle u_j| \rho |u_j\rangle \langle I_{4,j}| - |u_j\rangle \langle u_j| \rho - \rho |u_j\rangle \langle u_j|) \\
&+ \gamma_4 (n_4 (T_2) + 1) \sum_j (2 |I_{1,j}\rangle \langle l_j| \rho |l_j\rangle \langle I_{1,j}| - |l_j\rangle \langle l_j| \rho - \rho |l_j\rangle \langle l_j|) \\
&+ \gamma_4 n_4 (T_2) \sum_j (2 |l_j\rangle \langle I_{1,j}| \rho |I_{1,j}\rangle \langle l_j| - |I_{1,j}\rangle \langle I_{1,j}| \rho - \rho |I_{1,j}\rangle \langle I_{1,j}|) \quad . \qquad (7.0.6)
\end{aligned}
$$

Approximate Analytical Solutions

For T_2 small enough we can neglect n_1, n_3 and n_4. Inserting the steady state solutions for $\left\langle a\sigma_j^+ \right\rangle_{\mathrm{st}}$, $\langle |u_j\rangle \langle u_j| \rangle_{\mathrm{st}}$ and $\langle |l_j\rangle \langle l_j| \rangle_{\mathrm{st}}$ into the equation for $\left\langle \sigma_j^- \sigma_k^+ \right\rangle$ we obtain

$$
\begin{aligned}
&2 \left\langle \sigma_j^- \sigma_k^+ \right\rangle_{\mathrm{st}} \Bigg[\gamma_1 + \gamma_4 + \Bigg(g^4 N^2 |J_2|^2 \left\langle \sigma_j^- \sigma_k^+ \right\rangle_{\mathrm{st}} (2+3n_2)\gamma_2\gamma_3(\gamma_2 + n_2\gamma_2 + \gamma_3)\gamma_4 \\
&\quad + |J_1|^2 \Big(g^4 N^2 \left\langle \sigma_j^- \sigma_k^+ \right\rangle_{\mathrm{st}} n_2^2 \gamma_2^2 \gamma_3 \gamma_4 + |J_2|^2 \big(2 g^4 N^2 \left\langle \sigma_j^- \sigma_k^+ \right\rangle_{\mathrm{st}} \\
&((\gamma_2+\gamma_3)\gamma_4 + n_2\gamma_2(\gamma_3 + 2\gamma_4)) + g^2 N n_2 \gamma_2 \gamma_3 (\gamma_1 - \gamma_4)\kappa + n_2\gamma_2\gamma_3(\gamma_4^2 - \gamma_1^2)\kappa^2)\Big)\Bigg) \\
&\quad / \Bigg(\gamma_1 \kappa^2 \Big(|J_2|^2 (2+3n_2)\gamma_2\gamma_3(\gamma_2 + n_2\gamma_2 + \gamma_3)\gamma_4 \\
&\quad + |J_1|^2 (n_2^2 \gamma_2^2 \gamma 3 \gamma_4 + 2 |J_2|^2 ((\gamma_2+\gamma_3)\gamma_4 + n_2\gamma_2(\gamma_3 + 2\gamma_4)))\Big)\Bigg)\Bigg] = 0 \qquad (7.0.7)
\end{aligned}
$$

for the quantity $\left\langle \sigma_j^- \sigma_k^+ \right\rangle_{\mathrm{st}}$ describing cooperative behavior between the structures. The stable solution is obtained from the part of Eq. (7.0.7) which is enclosed by the rectangular brackets. To find the number of structures necessary for reaching the onset of cooperative behavior $N_{\mathrm{th}}\left(T_1\right)$ for a given temperature T_1 we solve $\left\langle \sigma_j^- \sigma_k^+ \right\rangle_{\mathrm{st}} = 0$ to find

$$N_{\mathrm{th}}\left(T_1\right) = \frac{\gamma_4 \kappa}{g^2} + \alpha\left(T_1\right)\gamma_1 + \mathcal{O}\left(\gamma_1^2\right) \tag{7.0.8}$$

for small γ_1, where

$$\alpha\left(T_1\right) = \frac{A}{n_2} + B + C n_2 \ . \tag{7.0.9}$$

The first term causes the divergence of N_{th} for small T_1 in Fig. 2(b) (dashed line). The coefficients are $A = (2\gamma_4\kappa(\gamma_2+\gamma_3)(\gamma_2\gamma_3+\left|J_1\right|^2))/(g^2\gamma_2\gamma_2\left|J_2\right|^2)$, $B = (\kappa[\gamma_3\gamma_4(5\gamma_2+3\gamma_3)+\left|J_1\right|^2(3\gamma_3+4\gamma_4)])/(g^2\gamma_3\left|J_1\right|^2)$, and $C = (\gamma_2\gamma_4\kappa[3/\left|J_1\right|^2 + 1/\left|J_2\right|^2])/g^2$.

For the thermal photon number

$$n_2 = \frac{\sqrt{2}\left|J_2\right|\sqrt{\gamma_2+\gamma_3}\sqrt{\gamma_2\gamma_3+\left|J_1\right|^2}}{\sqrt{\gamma_2^2\gamma_3\left(\left|J_1\right|^2+3\left|J_2\right|^2\right)}} \tag{7.0.10}$$

we find a minimum of $N_{\mathrm{th}}\left(T_1\right)$. Similar calculations give the critical temperature $T_{1,\mathrm{th}}$ for given N, see Fig. 2(a).

Calculation of the spectrum

Using the quantum regression theorem we obtain $\left\langle a^\dagger\left(t+\tau\right)a\left(t\right)\right\rangle$ which couples to $\left\langle \sigma_j^+\left(t+\tau\right)a\left(t\right)\right\rangle$. For $t \to \infty$ using stationarity we can write

$$\frac{\mathrm{d}}{\mathrm{d}\tau}\begin{pmatrix}\left\langle a^\dagger\left(\tau\right)a\left(0\right)\right\rangle \\ \left\langle \sigma_j^+\left(\tau\right)a\left(0\right)\right\rangle\end{pmatrix} = \begin{pmatrix}-\kappa & \mathrm{i}gN \\ -\mathrm{i}gD & \mathrm{i}\Delta_u - \Gamma\end{pmatrix} \times \begin{pmatrix}\left\langle a^\dagger\left(\tau\right)a\left(0\right)\right\rangle \\ \left\langle \sigma_j^+\left(\tau\right)a\left(0\right)\right\rangle\end{pmatrix} \tag{7.0.11}$$

with

$$D = \left(\left\langle \left|u_j\right\rangle\left\langle u_j\right|\right\rangle_{\mathrm{st}} - \left\langle \left|l_j\right\rangle\left\langle l_j\right|\right\rangle_{\mathrm{st}}\right) \ ,$$

and

$$\Gamma = \gamma_3 n_3 \left(T_2\right) + \gamma_1 \left(2n_1 \left(T_2\right) + 1\right) + \gamma_4 \left(n_4 \left(T_2\right) + 1\right) \ .$$

The Laplace transformation yields

$$\left\langle a^\dagger a \right\rangle (s) = \frac{\left\langle a^\dagger a \right\rangle_{\mathrm{st}} \left(s - \mathrm{i}\Delta_u + \Gamma\right) + \mathrm{i}gN \left\langle \sigma_j^+ a \right\rangle_{\mathrm{st}}}{\left(s + \kappa\right)\left(s - \mathrm{i}\Delta_u + \Gamma\right) - g^2 ND} \tag{7.0.12}$$

which allows to calculate the spectrum [7.11]. An approximation for the linewidth is found by expanding the denominator for small s.

References for Chapter 7

[7.1] W.E. Lamb Jr. “Theory of an optical maser.” In: *Phys. Rev* 134.6A (1964), A1429–A1450.

[7.2] H.E.D. Scovil and E.O. Schulz-DuBois. “Three-level masers as heat engines.” In: *Physical Review Letters* 2.6 (1959), pp. 262–263.

[7.3] E. Boukobza and D.J. Tannor. “Thermodynamic analysis of quantum light amplification.” In: *Physical Review A* 74.6 (2006), p. 063822.

[7.4] E. Boukobza and D.J. Tannor. “Three-level systems as amplifiers and attenuators: A thermodynamic analysis.” In: *Physical review letters* 98.24 (2007), p. 240601.

[7.5] M. Youssef, G. Mahler, and A.S.F. Obada. “Quantum heat engine: A fully quantized model.” In: *Physica E: Low-dimensional Systems and Nanostructures* 42.3 (2010), pp. 454–460.

[7.6] S. Kumar et al. “A 1.8-THz quantum cascade laser operating significantly above the temperature of $\hbar\omega/k_B$.” In: *Nature Physics* 7.2 (2010), pp. 166–171.

[7.7] R.I. Epstein et al. “Observation of laser-induced fluorescent cooling of a solid.” In: *Nature* 377.6549 (1995), pp. 500–503.

[7.8] H.J. Carmichael. *An open systems approach to quantum optics: lectures presented at the Université libre de Bruxelles, October 28 to November 4, 1991.* Vol. 18. Springer, 1993.

[7.9] R. Kubo. “Generalized cumulant expansion method.” In: *J. Phys. Soc. Japan* 17.7 (1962), pp. 1100–1120.

[7.10] D. Meiser et al. “Prospects for a millihertz-linewidth laser.” In: *Physical Review Letters* 102.16 (2009), p. 163601.

[7.11] P. Meystre and M. Sargent. *Elements of quantum optics.* Springer Verlag, 2007.

8. List of Publications

Preprints

- K. Sandner, H. Ritsch, *Temperature gradient driven lasing and stimulated cooling*, (submitted)

Publications

- K. Sandner, H. Ritsch, R. Amsüss, C. Koller, T. Nöbauer, S. Putz, J. Schmiedmayer, J. Majer, *Strong magnetic coupling of an inhomogeneous NV ensemble to a cavity* Physical Review A (Atomic, Molecular, and Optical Physics) 85, 053806 (2012)

- R. Amsüss, C. Koller, T. Nöbauer, S. Putz, S. Rotter, K. Sandner, S. Schneider, M. Schramböck, G. Steinhauser, H. Ritsch, J. Schmiedmayer, J. Majer, *Cavity QED with Magnetically Coupled Collective Spin States*, Physical Review Letters 107, 060502 (2011)

- K. Henschel, J. Majer, J. Schmiedmayer, H. Ritsch, *Cavity QED with an ultracold ensemble on a chip: Prospects for strong magnetic coupling at finite temperatures*, Physical Review A (Atomic, Molecular, and Optical Physics) 82, 033810 (2010)

Danksagung

Ich möchte Prof. Helmut Ritsch für seinen Einsatz und seine Unterstützung danken. In Momenten großer Verwirrung bekam ich Ansätze aufgezeigt die mir halfen Klarheit zu schaffen, in Momenten weniger großer Verwirrung bekam ich Zeit und Ermutigung meine Ideen und Ziele zu verfolgen.

Der österreichischen Akademie der Wissenschaften möchte ich dafür danken, dass sie meine Arbeit durch ein DOC-fFORTE Stipendium maßgeblich unterstützt hat. Im weiteren wurde ich von der Universität Innsbruck mit einem Stipendium zur Nachwuchsförderung unterstützt.

Einer der anfänglich schwierigsten aber in der Rückschau lohnenswertesten Schritte war das Finden einer gemeinsamen Sprache mit den Physikern am Experiment. Die Möglichkeit direkt mit interessierten, geduldigen und freundlichen Menschen sprechen zu können war mir ein besonderes Vergnügen. Mein Dank gilt dabei Johannes Majer, Robert Amsüss, Tobias Nöbauer und Christian Koller. Herrn Prof. Jörg Schmiedmayer danke ich für die Unterstützung meiner Forschung und die aufmerksame Lektüre meiner Arbeiten.

Meiner Familie möchte ich für die Unterstützung danken die ich über die Jahre hinweg während meiner Ausbildung erhalten habe.